Identification of the novel role of sterol regulatory element binding proteins (SREBPs) in mechanotransduction and intraocular pressure regulation

Ting Wang[1,2], Avinash Soundararajan[1], Jeffery Rabinowitz[3], Anant Jaiswal[4], Timothy Osborne[4], Padmanabhan Paranji Pattabiraman[1,2]

[1]Glick Eye Institute, Department of Ophthalmology, Indiana University School of Medicine, 1160 West Michigan Street, Indianapolis, Indiana, 46202, United States of America

[2]Stark Neuroscience Research Institute, Medical Neuroscience Graduate Program, Indiana University School of Medicine, 320 W. 15th Street, Indiana, 46202, United States of America

[3]Department of Ophthalmology, Case Western Reserve University, Cleveland, Ohio, United States of America

[4]Institute for Fundamental Biomedical Research, Department of Medicine and Biological Chemistry, Johns Hopkins University School of Medicine, St. Petersburg, Florida, 33701, United States of America

Key Words: Intraocular pressure, trabecular meshwork, sterol regulatory element binding protein, mechanotransduction, lipid biogenesis, actin cytoskeleton, extracellular matrix

Synopsis

In this study, we show the role of lipogenic transcription factors sterol regulatory element binding proteins (SREBPs) in the regulation of intraocular pressure (IOP). (**Synopsis Figure - *Created using Biorender.com***)

- SREBPs are involved in the sensing of changes in mechanical stress on the trabecular meshwork (TM). SREBPs aid in transducing the mechanical signals to induce actin polymerization and filopodia/lamellipodia formation.
- SREBPs inactivation lowered genes and enzymes involved in lipogenesis and modified lipid levels in TM.
- SREBPs activity is a critical regulator of ECM engagement to the matrix sites.
- Inactivation of SCAP-SREBP pathway lowered IOP via actin relaxation and decreasing ECM production and deposition in TM outflow pathway signifying a novel relationship between SREBP activation status and achieving IOP homeostasis.

Abstract

Trabecular meshwork (TM) cells are highly contractile and mechanosensitive to aid in maintaining intraocular pressure (IOP) homeostasis. Lipids are attributed to modulating TM contractility with poor mechanistic understanding. In this study using human TM cells, we identify the mechanosensing role of the transcription factors sterol regulatory element binding proteins (SREBPs) involved in lipogenesis. By constitutively activating SREBPs and pharmacologically inactivating SREBPs, we have mechanistically deciphered the attributes of SREBPs in regulating the contractile properties of TM. The pharmacological inhibition of SREBPs by fatostatin and molecular inactivation of SREBPs *ex vivo* and *in vivo* respectively results in significant IOP lowering. As a proof of concept, fatostatin significantly decreased the SREBPs responsive genes and enzymes involved in lipogenic pathways as well as the levels of the phospholipid, cholesterol, and triglyceride. Further, we show that fatostatin mitigated actin polymerization machinery and stabilization, and decreased ECM synthesis and secretion. We thus postulate that lowering lipogenesis in the TM outflow pathway can hold the key to lowering IOP by modifying the TM biomechanics.

1. Introduction:

Chronic and sustained elevation in intraocular pressure (IOP) is a significant risk factor for primary open angle glaucoma (POAG) (1-3). A rise in IOP above normal causes mechanical stress and reduced blood flow to the optic nerve (4). This increases the risk of glaucoma with significant consequences on vision and quality of life (5-7). Glaucoma is a major public health concern and the second leading cause of irreversible blindness worldwide afflicting mainly the aging population (8, 9). The estimated number of glaucoma patients in the world is around 80 million with over 2 million in the United States alone (10, 11). Interestingly lowering IOP is neuroprotective and the most effective way to delay the onset of POAG and to halt the progression towards vision loss (12-14). A 20% decrease in IOP significantly alleviates the risk of developing glaucoma (15). The IOP is maintained by the balance between the generation of AH via the ciliary body and drainage mainly via the conventional outflow pathway, which includes trabecular meshwork (TM), juxtacanalicular TM tissue (JCT), and Schlemm's canal (SC) (16). The TM contains an extracellular matrix (ECM) organized into a network of beams lined by highly contractile and mechanosensitive TM cells sensing pressure changes (17-19). Increased actin

contractility in TM and ECM hyperdeposition in TM outflow pathway augment AH outflow resistance and IOP elevation (20-22). In POAG, the increased IOP is directly correlated with the increased outflow resistance, and the most characteristic structural change in TM is increased tissue stiffness including ECM accumulation, increased cell contractility, and cell-ECM connections (18, 23-25). Thereby mitigating TM contractility and the ECM based stiffness has provided novel therapeutic options to lower IOP (26).

Cellular lipids play important roles in tissue biomechanics by modulating the plasma membrane remodeling, signal transduction cascades, and actin cytoskeleton-cell adhesions linked to the ECM (27). Moreover, various lipids found in TM and AH are known to impact IOP homeostasis (28-30). This is attributed via modulating the signaling events including altering the TM contractility and tissue stiffness. Hyperlipidemia is associated with an increased risk of elevated IOP and glaucoma with poor mechanistic understanding (31-33). Interestingly, cholesterol-lowering statins lower IOP and reduce the incidence of glaucoma (34-36). Mechanistic studies in TM point at statin-mediated disruption of membrane association of Rho GTPase due to inhibition of the isoprenylation of Rho (36, 37). We recently found that cyclic mechanical stretch, which mimics mechanical stress on TM, significantly altered lipid contents and increased the expression of cholestogenic enzymes like squalene synthase, 3-hydroxy-3-methylglutaryl coenzyme A (HMG-CoA) synthase (HMGCS) and the transcriptional regulator of lipid biogenesis sterol regulatory element binding protein 2 (SREBP2) in human TM (HTM) cells (38). The SREBPs are master regulator of cellular lipogenesis and occur as three isoforms – SREBP1a, SREBP1c, and SREBP2 (39-41). SREBP1a is involved in overall lipid biosynthesis, SREBP1c regulates fatty acid synthesis, whereas SREBP2 modulates sterol biosynthesis specifically (39-42). SREBPs are basic-helix-loop-helix leucine zipper (bHLH-LZ) transcription factors. Each SREBP precursor has three domains: (1) an NH2-terminal domain including transactivation domain, which is rich in serine and proline and the bHLH-LZ region for DNA binding and dimerization; (2) two hydrophobic transmembrane spanning segments; (3) a COOH-terminal domain (43, 44). Within the cell, following SREBPs mRNA translation, the proform SREBPs (Pro-SREBPs) are bound to SREBP cleavage activating protein (SCAP) forming a SCAP-SREBP complex located on the ER membrane. Stimuli including low lipids levels promote SCAP to guide the whole complex to leave the ER membrane to the Golgi membrane. In the Golgi, the SCAP-SREBP complex is cleaved by site 1 protease (S1P) and site 2 protease (S2P), releasing SCAP from the complex and releasing the active or nuclear SREBPs (N-SREBPs) from Golgi to translocate into the nucleus. Inside the nucleus, N-SREBPs bind to the sterol response element (SRE) on the promoter region of the responsive genes and promote their transcription. These target genes are involved in the fatty acid, triglycerides, and cholesterol biosynthetic pathways by modulating the expression of rate limiting enzymes like acetyl-CoA carboxylase (ACC), fatty acid synthase (FAS), and 3-hydroxy-3-methylglutaryl coenzyme A (HMG-CoA) reductase (HMGCR) (42, 44-47). Interestingly, it was earlier reported that there is an isoprenylation of RhoA-dependent and cholesterol-independent actin cytoskeleton contraction, which prevents SREBP1 dependent lipogenesis in human immortalized cancer lines and *Drosophila* (48). Such regulatory mechanistic evaluation of lipogenic pathways in AH outflow tract and the role of SREBPs in TM biology lacks understanding. By regulating lipid biogenesis in TM, we believe that SREBPs activities play a significant role in defining actin polymerization and ECM remodeling (49-52). Investigating the mechanosensing function via SREBPs activation paradigm in TM can elucidate how TM cells actively sense and transduce mechanical signals via SREBPs. Thus, we report the biological relevance of SREBPs activation in TM for active pressure sensing to convert mechanical stimuli into TM contractility and mechanistically decipher how the inactivation of SREBPs in the TM outflow pathway lowers IOP.

2. Material and Methods:

2.1 Materials:

104 The reagents and antibodies used in this study are documented in Table 1.

105

106 **2.2 Primary TM cell culture:**

107 Primary human TM (HTM) cells were cultured from TM tissue isolated from the leftover donor corneal
108 rings after they had been used for corneal transplantation at the Indiana University Clinical Service,
109 Indianapolis, and characterized as described previously (20, 53). HIPPA compliance guidelines were
110 adhered for the use of human tissues. The usage of donor tissues was exempt from the DHHS regulation
111 and the IRB protocol (1911117637), approved by the Indiana University School of Medicine IRB review
112 board.

113 Primary porcine TM (PTM) cells were cultured from fresh porcine TM globes obtained from Indiana
114 Packers, Delphi, In, USA, as described previously (20).

115 All experiments were conducted using confluent HTM or PTM cultures as mentioned, using cells in
116 between passage four to six, and were performed after overnight serum starvation unless mentioned,
117 otherwise. All experiments in this manuscript were performed using biological replicates.

118 **2.3 Construction of replication-deficient recombinant adenovirus expressing N-SREBPs**

119 Generation of replication-defective recombinant adenovirus expressing N-SREBPs under CMV promoter
120 was performed using ViraPower Adenoviral Expression System (#K4930-00, Invitrogen) as described
121 earlier (54). N-SREBP1a (1470 bps) , N-SREBP1c (1398 bps), and N-SREBP2 (1440 bps) were amplified
122 using high-fidelity PCR (Advantage-HF 2 PCR kit, #639123; Clontech) from human pcDNA3.1-2xFLAG-
123 SREBP1a (#26801, Addgene), pcDNA3.1-2xFLAG-SREBP1c (#26802, Addgene) and pcDNA3.1-2xFLAG-
124 SREBP-2 (#26807, Addgene). Amplified N-SREBP1a (Ad5-N-SREBP1a), N-SREBP1c (Ad5-N-SREBP1c), and
125 N-SREBP2 (Ad5-N-SREBP2) were purified, and titers determined.

126 **2.4 Adenovirus-mediated gene transduction in HTM cells**

127 Primary HTM cells were grown on gelatin-coated glass coverslips or in plastic Petri dishes and were
128 infected with Ad5-N-SREBP1a, Ad5-N-SREBP1c, and Ad5-N-SREBP2 or a control empty virus (AdMT) at 50
129 multiplicities of infection for 24 h followed by 48 h serum starvation. Cells were then washed with 1X
130 PBS and were fixed for immunofluorescence (IF) analysis and collected using either TRIZOL for RNA
131 extraction or 1X RIPA for protein extraction.

132 **2.5 Optimization fatostatin for *in vitro* dosing**

133 Fatostatin directly binds to SCAP and inhibits the SREBP-escorting function of SCAP, thereby restricting
134 the translocation of SREBPs from ER to the Golgi and subsequently causing SREBPs inactivation and
135 reducing lipogenesis and fat accumulation (55-57). Overnight serum starvation (~16 h) was carried out
136 on PTM and HTM cultures before treatments. To identify the optimal concentration of fatostatin for
137 lowering SREBPs activation, PTM cells were subjected to 0.2, 2, and 20 µM fatostatin reconstituted in
138 serum-free DMEM for 24 h respectively, and the solvent dimethyl sulfoxide (DMSO) treated PTM cells
139 were used as a control. Post-treatment, PTM cells were either used for cell viability assay or protein
140 collected for total and nuclear fraction. HTM cells were subjected to the optimal concentration of
141 fatostatin and post-treatment, cells were collected in TRIZOL for RNA isolation or in 1X

142 radioimmunoprecipitation assay (RIPA) buffer for protein isolation along with the cell culture media and
143 stored in -80 °C until used.

144 **2.6 Cell viability assay**

145 The cell viability assay was performed using fluorescein diacetate (FDA) and propidium iodide (PI)
146 staining. PTM cells were grown in 6-well plates until they attained 90% confluency. The cells were
147 treated with a final concentration of 20 µM fatostatin for 24 h after overnight serum starvation. FDA-PI
148 double staining was performed based on a previously published protocol with minor modifications (58).

149 **2.7 Cyclic mechanical Stretch:**

150 HTM cells were plated on BioFlex® Culture Plates (Flexcell International Corp) and subjected to cyclic
151 mechanical stretch as published earlier (38). 2 h and 6 h post stretch, cells were fixed and processed for
152 IF analysis.

153 **2.8 Porcine *ex vivo* elevated IOP model**

154 Elevated IOP was modeled using porcine *ex vivo* perfusion system as described earlier (20, 54). Post
155 perfusion the TM tissue was carefully isolated and frozen at -80°C until further processing.

156 **2.9 *Ex vivo* porcine anterior segment perfusion culture to assess the effect of SREBPs inactivation on**
157 **IOP**

158 The effect of pharmacological SREBPs inactivation on IOP regulation was studied using *ex vivo* porcine
159 anterior segment perfusion culture as described earlier (20). After achieving a stable baseline IOP, the
160 IOP was continuously recorded in the control eyes that received a sham DMSO treatment, and the
161 experimental eyes received 20 µM fatostatin for up to 24h. The relative changes in IOP were calculated
162 as the change in pressure relative to the baseline of drug/sham perfusion. At the end of the perfusion
163 studies, TM tissues were either sectioned for histology studies and fixed with 4% paraformaldehyde, or
164 the TM was collected for protein analysis.

165 **2.10 SCAP-Floxed (*SCAP*$^{f/f}$) mice**

166 All experiments were performed in compliance with the Association for Research in Vision and
167 Ophthalmology (ARVO) Statement for the Use of Animals in Ophthalmic and Vision Research. Mice
168 carrying the floxed Scap allele (B6;129-*Scap*^{tm1Mbjg}/*J*) (59) were obtained from Dr. Tim Osborne, bred,
169 and housed under a standard 12 h light and dark cycle with food and water provided *ad libitum* in the
170 laboratory animal resource center (LARC). Exon 1 of the SCAP gene is flanked with LoxP sites, which are
171 targets for bacteriophage P1 Cre recombinase originally made by Dr. Horton, UTSW Med Center, Dallas
172 (59, 60). They are viable, fertile, normal in size, and do not display any physical or behavioral
173 abnormalities. The genotype was identified by PCR analysis of tail biopsies. All animal procedures were
174 approved by the Institutional Animal Care and Use Committee at the Indiana University School of
175 Medicine and conducted following the Declaration of Helsinki.

176 **2.11 Molecular inactivation of SREBPs *in vivo* in *SCAP*$^{f/f}$ mice**

177 Molecular inactivation of SREBPs was achieved by knocking down SCAP in *SCAP*$^{f/f}$ mice via intravitreal
178 injection of adenovirus expressing Cre [Ad5.CMV.iCre-eGFP] (1.6×10^{11} pfu/ml). The Ad5.CMV.eGFP
179 (2.6×10^{11} pfu/ml) was used as an adenovirus control and saline injection was used for injection control.

180 These adenoviruses were purchased from the Vector Development Lab, Baylor College of Medicine. Four
181 groups were included in the study: untouched, saline injection, Ad5.CMV.eGFP injection, and
182 Ad5.CMV.Cre-eGFP injection. A 33-gauge needle with a glass microsyringe (10 µL volume; Hamilton
183 Company) was used for the intravitreal injection. Intravitreal injections were performed only in the left
184 eye under a surgical microscope (Trinocular Stereo Zoom Microscope, AmScope). The needle was
185 inserted through the equatorial sclera into the vitreous chamber at an angle of ~ 45°, carefully avoiding
186 contact with the posterior lens capsule or the retina. The right eyes in all groups were left untouched.
187 Viral vectors or saline in a volume of 2 µL were slowly injected into the vitreous over the course of 30
188 seconds. The needle was then left in place for an additional 45 s to avoid leakage before being
189 withdrawn. Before and during intravitreal injection, mice were anesthetized with isoflurane (2.5%)
190 (#NDC 46066-755-04, Patterson Veterinary, Loveland, CO, USA) and 100% oxygen using SomnoSuite
191 (Kent Scientific Corporation, Torrington, CT, USA). Initially, a total of 15 animals/group were used, but
192 post-injection due to infection, cataract formation, and death the final numbers were reduced to 9-10
193 mice/group for the data acquisition with a roughly equal number of adult (10-14 months) and old (18-24
194 months) mice.

195 **2.12 Measurement of IOP**

196 The mice were anesthetized with 2.5% isoflurane and 100% oxygen using SomnoSuite. A previously
197 validated commercial rebound tonometer (TonoLab, Colonial Medical Supply) was used to take three
198 sets of six measurements of IOP in each eye. The IOP measurement and recording were carried out in a
199 blinded manner by the experimenter to minimize outcome bias. Right and left eye measurement sets
200 were alternated with the initial eye selected randomly. All measurements were taken between 3 and 5
201 min after isoflurane inhalation. As indicated by the manufacturer, the tonometer was fixed horizontally
202 for all measurements, and the tip of the probe was 2–3 mm from the eye. The probe contacted the eye
203 perpendicularly over the central cornea. The average of a set of measurements was accepted only if the
204 device indicated that there was "no significant variability" (as per the protocol manual; Colonial Medical
205 Supply). Daytime measurements were taken between 10:00 and 15:00 h. Baseline IOP was measured
206 before saline and viral vector injection. After injection, IOP was measured every 10 days until 50 days
207 post-injection.

208 **2.13 Gene expression analysis**

209 Total RNA was extracted from HTM cells using the Trizol method following the manufacturer's protocol.
210 The RNA amount used, cDNA conversion, and using reverse-transcription polymerase chain reaction (RT-
211 PCR) or qPCR reaction was conducted as published before (54). Sequence-specific forward and reverse
212 oligonucleotide primers for the indicated genes are provided in **Table 2**. The qPCR reaction was
213 performed and calculated by the delta-delta Ct method as described earlier (54, 61). The normalization
214 was performed using 18S ribosomal RNA (18S rRNA) for HTM.

215 **2.14 Protein Analysis by Immunoblotting**

216 For nuclear fraction, cells were collected from a 10 cm plate using fractionation buffer (20 mM HEPES,
217 10 mM KCl, 2 mM MgCl2, 1 mM EDTA, 1 mM EGTA, 1 mM DTT). After using a 1 mL syringe to pass cell
218 suspension through a 27 gauge needle several times, the sample was centrifuged and a pellet that
219 contains nuclei was collected. The pellet was washed, dispersed, and centrifuged again, then the nuclear
220 fraction was collected by TBS with 0.1% SDS.

221 The whole cell lysates containing total protein were prepared using 1X RIPA buffer composed of 50 mM
222 Tris-HCL (pH 7.2), 150 mM NaCl, 1% NP-40, 0.1% SDS, 1 mM EDTA, and 1 mM PMSF with protease and
223 phosphatase inhibitors (#A32961, ThermoFisher Scientific) and then sonicated. Nuclear extraction was
224 collected using 20mM HEPES (pH 7.4), 10mM KCl, 2mM MgCl2, 1mM EDTA, and 1mM EGTA. Media was
225 collected, concentrated using Nanosep® Centrifugal Devices with Omega™ Membrane 10K (#OD010C34,
226 Pall), and the media protein was collected in 1X RIPA.

227 After determining the protein concentration, immunoblotting was performed as published earlier (38,
228 54). Blots were stripped using mild stripping buffer if required to reprobe for the loading control and
229 multiple proteins within the same molecular weight range. The data were normalized to GAPDH, β-actin,
230 LaminB1, or Ponceau S. Semi-quantitative analyses and fold changes were calculated from the band
231 intensities measured using ImageJ software.

232 **2.15 Protein distribution analysis by immunohistochemistry (IHC) and IF**

233 Tissue sections from formalin-fixed, paraffin-embedded human donor whole globes eyes were prepared
234 at Case Western Reserve University, Cleveland, Ohio. Paraffin-embedded porcine TM tissue slides and
235 mice eyeball slides were prepared at the Histology Core, Indiana University, and immunolabeling was
236 performed. IF staining was done on HTM cells grown on 2% gelatin-coated glass coverslip or BioFlex®
237 Culture Plates. The methodologies used for IHC and IF has been published from the lab earlier (20, 54).

238 All the slides were observed under a Zeiss LSM 700 confocal microscope, and z-stack images were
239 obtained and processed using Zeiss ZEN image analysis software.

240 **2.16 Quantitative image analysis**

241 ImageJ (version 1.53a) software was used to analyze the SREBPs nuclear fluorescence intensity in IF
242 HTM cell images and ECM proteins in IHC tissue images. Specifically, the IF images obtained from HTM
243 cells and tissue sections were converted into an 8-bit image, then the threshold default setup under
244 Adjust was used to convert the image from grayscale into a binary image. Next, the region of interest
245 (ROI) tool was utilized for analysis. In this analysis, the nuclear area in the HTM cells or ROIs (equal area)
246 in the TM outflow pathway was chosen in an image, and the intensities were measured and compared
247 between the DMSO control and fatostatin.

248 **2.17 Quantitative filamentous actin/globular actin (F-actin/G-actin) ratio measurement**

249 The F-actin/G-actin ratio was measured using G-Actin/F-Actin In Vivo Assay Biochem Kit (#BK037,
250 Cytoskeleton, Inc.), following the manufacturer's instructions.

251 **2.18 Myosin light-chain (MLC) phosphorylation status measurement**

252 Myosin light-chain phosphorylation status in HTM cells was measured by following the procedure
253 described (62). Specifically, after treatments, HTM cells were incubated with 10% cold trichloroacetic
254 acid (TCA) for 5 minutes and then washed with ice-cold water 5 times to completely remove the TCA.
255 The cells were extracted with 8 M urea buffer containing 20 mM Tris, 23 mM glycine, 10 mM
256 dithiothreitol (DTT), saturated sucrose, and 0.004% bromophenol, using a sonicator. The urea-
257 solubilized samples were separated on urea/glycerol PAGE containing 30% acrylamide, 1.5%
258 bisacrylamide, 40% glycerol, 20 mM Tris, and 23 mM glycine. Then proteins from these glycerol gels

259 were transferred onto nitrocellulose filters in 10 mM sodium phosphate buffer, pH 7.6. Membranes
260 were probed using phospho-myosin light chain (p-MLC) or myosin light chain (MLC) primary antibodies.

261 **2.19 Lipid content measurement**

262 HTM cells were plated on 100 mm plates. Post-treatment, cells were counted, equal numbers were
263 collected, and frozen at -80°C until analysis. Then the phospholipid, cholesterol, and triglyceride from
264 HTM cells were extracted and measured with a phospholipid quantification assay kit (#CS0001, Sigma-
265 Aldrich), cholesterol quantitation kit (#MAK043, Sigma-Aldrich) and triglyceride quantification kit
266 (#MAK266, Sigma-Aldrich) respectively, following manufacturer's instructions.

267 **2.20 Cellular lipid extraction and multiple reaction monitoring (MRM) profiling-based MS for**
268 **lipidomics and pathway analysis**

269 HTM cell pellets were collected from DMSO and fatostatin treated HTM cells. The lipid extraction was
270 performed as per the Bligh and Dyer protocol (63). Lipidomics and data analysis was processed as
271 published earlier (38, 64). In addition, pathway enrichment analysis was also performed to identify the
272 most relevant pathways associated with the identified metabolites using a web-based analysis module
273 (http://metaboanalyst.ca), which is based on Globaltest. Through pathway analysis, 8 metabolic
274 pathways related to the identified metabolites (n = 274) were mapped.

275 **2.21 Transmission electron microscope (TEM) imaging**

276 HTM cells grown on coverslips were treated with Ad5-N-SREBP1a, Ad5-N-SREBP1c, Ad5-N-SREBP2 or
277 AdMT for 48-72 h. After removing the growth media from each well, the coverslips were washed using
278 0.1 M Cacodylate buffer and submerged in 3% glutaraldehyde solution and 2% OsO4 subsequently. Then
279 the cells were dehydrated by 30%, 50%, 70%, 95%, and 100% EtOH consequently, and 1:3
280 acetone:EMbed 812 was applied overnight. The next day, the coverslips were embedded using EMbed
281 812 resin in a BEEM capsule for 24 hours. After that, the samples were detached from coverslips using
282 liquid nitrogen and then sectioned using a razor blade to generate EM grids for imaging. The grids were
283 stained with 4% uranyl acetate and 0.2% aqueous lead citrate and washed, then imaged on a PEI Tecnai
284 12 with a LaB_6 crystal at 120kV at the Center for Electron Microscopy, IUSM.

285 **2.22 Statistical analysis**

286 All data presented were based on greater than three independent observations and inclusion of
287 biological replicates for *in vitro* analysis. The graphs represent the mean ± standard error. All statistical
288 analyses were performed using Prism 9.3.1 (GraphPad). The difference between the two groups was
289 assessed using paired Student's t-test when parametric statistical testing was applicable. When multiple
290 groups were compared, a two-way analysis of variance followed by the Tukey post hoc test was applied.
291 The p-value < 0.05 was considered a statistically significant difference between the test and control.

292 **3. Results:**

293 **3.1 SREBPs and SCAP are expressed in the human AH outflow pathway and TM cell cultures**

294 Initially we checked for the expression and distribution of SREBPs and SCAP in human TM outflow
295 pathway (**Supplementary Figure 1**) since it has never been investigated earlier. We found the expression
296 of SREBP isoforms and SCAP transcripts in HTM cells in primary HTM cell cultures (**Supplementary Figure**

297 **1A**). Additionally, the SREBP isoforms and SCAP protein were found in HTM and PTM cells. We observed
298 pro-SREBP1 and pro-SREBP2 at ~ 125 kDa, N-SREBP1 and N-SREBP2 at ~ 68 kDa, and SCAP at ~ 140 kDa
299 (**Supplementary Figure 1B and 1C**). IF analysis and confocal imaging of SREBP1, 2, and SCAP distribution
300 in HTM cells and the conventional human AH outflow pathway show their distinct localizations. In HTM
301 cells, both SREBP1 and 2 showed cytoplasmic and nuclear distribution (**Supplementary Figure 1D**).
302 Relatively, SREBP1 decorated the cytoplasmic and perinuclear region around the ER than in the nucleus.
303 On the other hand, SREBP2 showed a pronounced nuclear localization than cytoplasmic. The SCAP
304 showed cytoplasmic distribution (**Supplementary Figure 1D**). In the anterior chamber angle of a normal
305 human eye, the SREBP1, SREBP2, and SCAP immunopositive cells were seen in the TM-JCT region and
306 the endothelial lining of the SC (**Supplementary Figure 1E**). Interestingly, SREBP1 and 2, as well as SCAP
307 showed specific distribution in the TM-JCT region in the anterior chamber angle. Negative control in the
308 presence of secondary antibody alone did not show any staining (**Supplementary Figure 1F**).

309 **3.2 Mechanosensing via SREBPs activation in HTM cells aids in increasing the actin-based contractile**
310 **changes and lamellipodia formation**

311 In our recent work (38) on HTM cells subjected to mechanical stress, we showed a significant increase in
312 the N-SREBP2 that is involved in cholesterol biogenesis. To better understand the mechanosensing
313 functionality of SREBPs, here we provide empirical evidence by utilizing multiple systems to assess the
314 potential changes qualitatively and quantitatively in SREBPs localization under mechanical stress. Firstly,
315 we performed IF analysis post cyclic mechanical stretch to look at the changes in the localization of
316 SREBPs (in green) and F-actin (in red) changes in a time-dependent manner at 2 h and 6 h. After 2 h of
317 stretch (ST), HTM cells showed strong nuclear localization of SREBP1 (**Figure 1A**, second-row third
318 column) and SREBP2 (**Figure 1B**, second-row third column), compared to 2 h unstretched control (CTL)
319 (**Figure 1A and 1B**, first-row third column). HTM cells also showed increased F-actin fibers formation
320 (**Figure 1A and 1B**, second-row fourth column) after 2 h ST, compared to the 2 h CTL (**Figure 1A and 1B**,
321 first-row fourth column). Image analysis using ImageJ found significantly increased fluorescent intensity
322 for nuclear SREBP1 ($n = 30\text{-}40$, $p = 0.002$) and SREBP2 ($n = 30\text{-}40$, $p = 0.0001$) in HTM cells after 2 h ST,
323 compared to 2 h CTL (**Figure 1A and 1B**, right panel). Further we found that such increased nuclear
324 SREBPs paralleled with increased F-actin formation in stretched HTM cells. HTM cells were exposed to 2
325 h ST combined with the pharmacological inhibition of SREBPs activity using fatostatin treatment, a
326 specific SREBPs inhibitor. To test the inhibitory effect of fatostatin on SREBPs activity in TM, the dose-
327 dependency (0.2, 2, 20 µM) of fatostatin on PTM cells was performed. We found that 20 µM fatostatin
328 for 24 h treatment significantly decreased both N-SREBP1 ($n = 4$, $p = 0.02$) and N-SREBP2 ($n = 4$, $p = 0.02$)
329 from the total protein extract (**Supplementary Figure 2A and 2B**). The 20 µM fatostatin did not show
330 cytotoxic effects when tested using FDA and PI staining (**Supplementary Figure 2C**). Thus, 20 µM
331 fatostatin is the optimal concentration to be used in TM cells. IF shows that compared to 2 h ST alone, 2
332 h ST combined with 20 µM fatostatin treatment reduced both SREBP1 (**Figure 1A**, third-row third
333 column) and SREBP2 (**Figure 1B**, third-row third column) localization inside the nucleus, and a
334 concomitant decrease in F-actin distribution inside the HTM cells (**Figure 1A and 1B**, third-row fourth
335 column). Image analysis found that compared to 2 h ST alone, 2 h ST in combination with fatostatin
336 significantly decreased nuclear SREBP1 ($n = 30\text{-}40$, $p = 0.0001$) and SREBP2 ($n = 30\text{-}40$, $p = 0.0001$)
337 fluorescent intensity in HTM cells. Compared to 2 h CTL, 2 h ST combined with 20 µM fatostatin
338 treatment significantly decreased nuclear SREBP1 fluorescent intensity ($n = 30\text{-}40$, $p = 0.0001$), but
339 nuclear SREBP2 didn't show significant changes ($n = 30\text{-}40$, $p = 0.2$) (**Figure 1A and 1B**, right panel).

340 Similar results were found after 6 h ST in HTM cells with strong nuclear localization of SREBP1
341 (**Supplementary Figure 3A**, second-row third column) and SREBP2 (**Supplementary Figure 3B**, second-
342 row third column), and increased F-actin formation (**Supplementary Figure 3A and 3B**, second-row
343 fourth column) compared to 6 h CTL (**Supplementary Figure 3A and 3B**, first-row third and fourth
344 column, respectively). Image analysis comparing 6 h CTL versus 6 h ST showed significant increase in
345 nuclear SREBP1 (n = 30-40, p = 0.0001) and SREBP2 (n = 30-40, p = 0.0001) fluorescent intensity in HTM
346 cells (**Supplementary Figure 3A and 3B**, right panel). Additional evidence for the role of SREBPs in
347 mechanosensing was obtained using the acute anterior chamber pressure model (20, 54, 65). Porcine
348 anterior segments when subjected to two times (2x) elevated pressure (30 mmHg) compared to normal
349 pressure (15 mmHg), we found a significant increase in N-SREBP1 (n = 4, p = 0.04) and N-SREBP2 (n = 4,
350 p = 0.03) (**Figure 1C**). Thus, confirming that novel role of SREBPs activation as the hallmark of
351 mechanosensing in TM.

352 Since we found that augmented SREBPs activation paralleled with increased actin polymerization under
353 mechanical stress in HTM cells, we assessed if SREBPs activation aided in mechanotransduction. To
354 study this, we expressed Ad5-N-SREBPs in primary HTM cells *in vitro* and followed up with read outs
355 including cell shape changes, actin polymerization, and focal adhesion distribution changes. In serum-
356 starved HTM cells upon constitutively expression Ad5-N-SREBPs, Ad5-N-SREBP1a and Ad5-N-SREBP1c
357 significantly increased N-SREBP1 transcripts (n = 4, p = 0.01 and n = 4, p = 0.046, respectively), Ad5-N-
358 SREBP2 significantly increased N-SREBP2 mRNA expression (n = 4, p = 0.01) (**Supplementary Figure 4A**)
359 in comparison to AdMT control. Similarly, N-SREBP1 protein expression significantly increased under
360 Ad5-N-SREBP1a (n = 4, p = 0.0001) and Ad5-N-SREBP1c (n = 4, p = 0.03) and N-SREBP2 significantly
361 increased under Ad5-N-SREBP2 (n = 4, p = 0.0005) (**Supplementary Figure 4B**). Upon examination under
362 light microscopy, the HTM cells treated with Ad5-N-SREBPs showed altered cell shape with increased
363 lamellipodia and filopodial extensions (**Supplementary Figure 4C**, denoted by black arrows). The
364 increase in N-SREBPs distribution (red staining) inside the nucleus were confirmed by IF imaging studies.
365 A strong nuclear localization of SREBP1 was observed under Ad5-N-SREBP1a (**Figure 2A**) (second-row
366 third column) and Ad5-N-SREBP1c (third-row third column) compared to AdMT (first-row third column)
367 and SREBP2 distribution inside the nucleus (**Figure 2B**) due to Ad5-N-SREBP2 (second-row third column)
368 compared with AdMT (first-row third column). In comparison to AdMT (**Figure 2A and 2B,** first-row fifth
369 column), Ad5-N-SREBP1a (**Figure 2A,** second-row fifth column), Ad5-N-SREBP1c (**Figure 2A,** third-row
370 fifth column), and Ad5-N-SREBP2 (**Figure 2B**, second-row fifth column) expression increased filamentous
371 actin (F-actin) distribution inside HTM cells (purple staining in the merged/individually in grayscale)
372 indicating greater actin polymerization. This was accompanied by redistribution of the focal adhesions -
373 vinculin (in green) in the merged/individually in grayscale (denoted by white arrows) at the edges of F-
374 actin was observed in Ad5-N-SREBP1a (**Figure 2A,** second-row fourth column), Ad5-N-SREBP1c (**Figure**
375 **2A**, third-row fourth column), and Ad5-N-SREBP2 (**Figure 2B**, second-row fourth column). An interesting
376 observation we found was increased lamellipodia and filopodia formation with a strong lamellipodial
377 actin network (**Figure 2A and 2B,** denoted by yellow arrows). Similar observations were found for
378 paxillin distribution in TM cells under constitutive activation of SREBPs (**Supplementary Figure 4D and**
379 **4E**). Further investigations into the lamellipodial structures identified strong localization of actin binding
380 protein Arp2/3, which is involved in branching of fibrillar actin, and the regulator of lamellipodial
381 dynamics Ras-associated and pleckstrin homology domains-containing protein 1 (RAPH1) or lamellipodin
382 (in green) to membrane under constitutive activation of SREBP1a, 1c, and 2 (**Figure 2C,** denoted by
383 white arrows). The ultrastructural examination of constitutive SREBPs activation using TEM showed that

384 compared to AdMT treatment, Ad5-N-SREBP1a, Ad5-N-SREBP1c and Ad5-N-SREBP2 treatments induced
385 membrane bending and filopodia formation in HTM cells (**Figure 2D**) corroborating with results from IF.
386 Interestingly, all Ad5-N-SREBPs treatments also induced the formation of caveolar or caveolae rosette
387 structures compared to AdMT treatment (**Figure 2D**). Thus, demonstrating the significant role of
388 mechanosensing by SREBPs and excessive mechanotransduction upon activation in TM. This prompted
389 us to examine the role of SREBPs in the regulation of IOP.

390 **3.3 Pharmacological inactivation of SREBPs lowers IOP by altering the ECM architecture of the TM AH**
391 **outflow pathway in *ex vivo* porcine perfusion cultures**

392 After deriving a linear relationship between SREBPs activation, mechanosensing, and increased actin
393 polymerization, we hypothesized that loss of SREBPs activity can have a significant effect on IOP. The
394 pharmacological inhibition of SREBPs activity was accomplished using fatostatin (56). Fatostatin
395 treatment (20 µM) for 24 h in PTM cells showed a significant decrease in N-SREBP1 ($n = 4$, $p = 0.01$) and
396 N-SREBP2 ($n = 4$, $p = 0.02$) protein levels when assayed in the nuclear fraction (**Figure 3A**) and in HTM
397 cells significantly decreased N-SREBP1 ($n = 4$, $p = 0.03$) and N-SREBP2 ($n = 4$, $p = 0.0001$) in the total
398 protein (**Figure 3B**). The SCAP protein expression did not change ($n = 4$, $p = 0.3$) (**Figure 3B**). The IF
399 localization of SREBP1 and SREBP2 distribution after fatostatin treatment demonstrated a marked
400 decrease inside the nucleus compared to the controls (**Figure 3C and 3D**). Histograms on the right of
401 **Figure 3C and 3D** represent the ImageJ-based quantification of nuclear SREBPs fluorescent intensities
402 showing a significant decrease in N-SREBP1 ($n = 5$, $p = 0.02$) and N-SREBP2 ($n = 5$, $p = 0.001$) fluorescent
403 staining. Thus, providing the proof-of-concept for fatostatin inhibiting SREBPs activity in TM cells.

404 We then tested the effect of SREBPs inactivation via fatostatin on IOP *ex vivo* using the porcine organ
405 culture system. Perfusion of 20 µM fatostatin significantly decreased IOP by 12 h ($n = 5$, $p = 0.04$), and
406 sustained until 22 h ($n = 5$, $p < 0.05$) (**Figure 3E**) compared to the DMSO perfused control eyes. To
407 determine the effects of fatostatin on the TM outflow pathway structures, we analyzed the histological
408 changes. Based on the H and E staining in the AH outflow pathway, the most prominent was the
409 increased spacing between the TM (**Figure 3F**) in the fatostatin perfused eyes compared to a more
410 compact TM in the DMSO perfused eyes. As a proof of concept, post-perfusion immunoblotting on total
411 protein from TM tissue showed significantly decreased N-SREBP1 ($n = 4$, $p = 0.005$) and N-SREBP2 ($n = 4$,
412 $p = 0.03$) in fatostatin-perfused TM (**Figure 3G**). Thus, demonstrating a direct result of SREBP inactivation
413 on decreased IOP. Moreover, histochemical evaluation on the TM outflow pathway revealed both
414 qualitative and quantitative decrease in ECM like COL1A and FN. We found that both COL1A and FN in
415 the TM-JCT region showed a marked decrease compared to the control (**Figure 3H**), which is
416 represented in the histogram for COL1A staining ($n = 5$, $p = 0.0001$), and FN staining ($n = 5$, $p = 0.0001$) in
417 the TM outflow pathway (**Figure 3H, right panel**). To get better insights, we performed immunoblotting
418 with the protein extracted from the TM tissue obtained from DMSO and fatostatin-perfused eyes. In
419 agreement with IHC results, we found that compared to DMSO-perfused the fatostatin-perfused TM
420 tissue showed significantly decreased expression of COL1A ($n = 4$, $p = 0.01$) and FN ($n = 4$, $p = 0.03$)
421 (**Figure 3I**). Thereby, the direct inhibition of SREBPs activity significantly reduced IOP potentially by
422 diminishing ECM in the TM outflow pathway and increasing the space around the TM tissue to increase
423 the AH outflow.
424

425 **3.4 Molecular inactivation of SREBPs by knocking down SCAP in *SCAP$^{f/f}$* mice lowers IOP *in vivo***

426 Since we established the direct effect of SREBPs inactivation on IOP *ex vivo*, we checked the effect of
427 SREBPs inactivation on IOP regulation in *SCAP$^{f/f}$* mice *in vivo*. Conditional knockdown of SCAP was

428 achieved using intravitreal injection of Ad5.CMV.iCre-eGFP in *SCAP$^{f/f}$* mice inducing the loss of SCAP in
429 the TM tissue due to Cre/lox recombination. The cohorts were divided into four groups - three injection
430 groups: Ad5.CMV.iCre-eGFP, Ad5.CMV.eGFP (sham virus control), and saline (sham injection control)
431 and one uninjected/untouched group. The IOP was measured over time in anesthetized *SCAP$^{f/f}$* mice
432 before injection to obtain the baseline IOP, and every 10 days after injection until 50 days post-injection.
433 Data presented here show the mean IOP ± SEM in mmHg. The Ad5.CMV.iCre-eGFP injection group
434 displayed a significant IOP lowering (12.97 ± 0.71, n = 10) compared to Ad5.CMV.eGFP injection group
435 (21.74 ± 1.47, n = 9, p = 0.0001), saline injection group (20.5 ± 1.00, n = 10, p = 0.0001), and the
436 untouched group (19.67 ± 0.83, n = 9, p = 0.0001) (**Figure 4A**) 10 days after injection. The decreased IOP
437 in Ad5.CMV.iCre-eGFP injection group compared to the control groups sustained up to 30 days post-
438 injection (n = 10, p < 0.05). At post-injection days 40 and 50, IOP in Ad5.CMV.iCre-eGFP injection group
439 was significantly decreased (n = 10, p < 0.05) compared to saline injection and Ad5.CMV.eGFP injection
440 groups. The IOP was also lower than the untouched group, but not statistically significant (**Figure 4A**).
441 We also compared the IOP changes within each group to their baseline normal IOP (before
442 injection/time point 0 days), and the result shows that there was no significant change in IOP levels in
443 untouched, saline injection, and Ad5.CMV.eGFP injection groups. However, within Ad5.CMV.iCre-eGFP
444 injection group, the IOP was significantly decreased 10 days post-injection and sustained till 50 days
445 post-injection (n = 10, p < 0.05). Start from 40 days post-injection, the IOP in Ad5.CMV.iCre-eGFP
446 injection group was slowly went back to the baseline (**Figure 4B**). Upon analyzing percentage changes in
447 IOP (delta IOP %) in each group at each time point, Ad5.CMV.iCre-eGFP injection group showed a
448 decrease of 40.38% compared to the baseline normal (before injection/time point 0 days) with an
449 average decrease of 27.85% (**Figure 4C**). The delta IOP % in the control groups were less than 13%
450 changes of baseline normal IOP. (**Figure 4C**). We evaluated IOP changes after SREBPs knock down in
451 adult and old mice to check if aging in combination with SREBPs knockdown influenced IOP. We found
452 IOP was consistently and significantly decreased in Ad5.CMV.iCre-eGFP group compared to
453 Ad5.CMV.eGFP group (n = 5, p < 0.05), and it was also lower than the untouched group and saline
454 injection group in the old and adult cohorts (**Supplementary Figure 5A and 5D, respectively**). In both old
455 and adult cohorts, there was no significant change in IOP levels in all sham control groups, but IOP was
456 significantly decreased 10 days post-injection in Ad5.CMV.iCre-eGFP injection group and sustained till 50
457 days post-injection (n = 5, p < 0.05) (**Supplementary Figure 5B and 5E, respectively**). The IOP in
458 Ad5.CMV.iCre-eGFP injection groups showed a decrease of as much as 42.72 % and 43.14 % of baseline
459 normal IOP in old and adult cohorts, respectively (**Supplementary Figure 5C and 5F, respectively**). All
460 sham control groups showed less than 17 % changes of baseline normal IOP in both old and adult mice
461 (**Supplementary Figure 5C and 5F, respectively**). At the end of the longitudinal IOP measurement study,
462 the mice eyes were enucleated and processed for histological and immunohistochemical analysis. The H
463 & E staining showed normal open iridocorneal angles and no marked differences in TM morphology in
464 all the groups (**Figure 4D**). Immunostaining in Ad5.CMV.iCre-eGFP injection group compared to all
465 control groups for - SCAP showed a marked decrease in TM (**Figure 4E, green arrow in the inset**),
466 SREBP1 and SREBP2 showed decreased distribution in the nuclear regions in TM (**Figure 4F and 4G,**
467 **green arrow in the inset**). This data proves that selective molecular knockdown of SCAP in TM outflow
468 pathway thereby inactivating SREBPs in TM significantly lowered IOP and confirming the significance of
469 SCAP-SREBP pathway in modulation of IOP.

470 **3.5 SREBPs inactivation impacts lipid metabolism in TM**

471 Since SREBPs are master regulators of lipid biosynthesis, as a proof-of-concept study, we looked at
472 changes in lipid metabolism in HTM cells under fatostatin treatment. HTM cells treated with 20 µM
473 fatostatin for 24 h significantly decreased many of the SREBPs responsive mRNA expression (**Figure 5A**)
474 involved in - 1) genes related to cholesterol biosynthesis: low-density lipoprotein receptor (LDLR) (n = 4,
475 p = 0.002), hydroxymethylglutaryl-CoA synthase 1 (HMGCS1) (n = 4, p = 0.004), 3-Hydroxy-3-
476 Methylglutaryl-CoA Reductase (HMGCR) (n = 4, p = 0.02), SREBP2 (n = 4, p = 0.02); 2) genes involved in
477 fatty acid biosynthesis: acetyl-CoA carboxylase (ACC) (n = 4, p = 0.0007), fatty acid synthase (FAS) (n = 4,
478 p = 0.0009), peroxisome proliferator-activated receptor gamma (PPARG) (n = 4, p = 0.005), acetyl-CoA
479 synthetase (ACS) (n = 4, p = 0.0008), SREBP1 (n = 4, p = 0.0003); and 3) gene regulating triglyceride and
480 phospholipid biosynthesis: glycerol-3-phosphate acyltransferase (GPAT) (n = 4, p = 0.08) (**Figure 5A**).
481 Using immunoblotting we checked for the expression of rate limiting enzymes involved in lipogenesis -
482 FAS, HMGCR, and ACC under fatostatin treatment. Compared to the DMSO controls, fatostatin
483 significantly decreased FAS (n = 4, p = 0.049), HMGCR (n = 4, p = 0.02), and ACC (n = 4, p = 0.049)
484 expression (**Figure 5B**). To further confirm the lipid changes under fatostatin treatment, we measured
485 normalized phospholipid/cell, normalized free cholesterol/cell, and normalized triglyceride/cell. The
486 results show that levels of phospholipid (n = 4, p = 0.0001) (**Figure 5C**), free cholesterol (n = 4, p = 0.04)
487 (**Figure 5D**), and triglyceride (n = 4, p = 0.04) (**Figure 5E**) were significantly reduced under fatostatin
488 treatment. Interestingly the magnitude of the phospholipid decrease was the highest (~95%). To better
489 understand changes in each lipid class under SREBPs inactivation, we performed shotgun lipidomics post
490 fatostatin treatment. Based on the lipidomic analysis, fatostatin treatment significantly decreased
491 multiple lipid classes that belonged to phosphatidylcholine (PC), phosphatidylethanolamine (PE), fatty
492 acids (FA), sphingomyelin (SM), and triglycerides (TG) **(Table 3)** correlating with the decrease in total
493 phospholipid/cell content (**Figure 5C**). On the other hand, the lipid class phosphatidylserine (PS) was
494 significantly increased **(Table 4**). The heatmap shows the fatostatin-mediated changes in the top 25 lipid
495 classes averaged across samples(**Supplementary Figure 6**). Fatostatin treatment decreased PC, PE,
496 Cholesteryl ester (CE), diacylglycerol (DG), FA, and TG (**Supplementary Figure 6A, 6B, 6C, 6D, 6E, and 6F**,
497 respectively); and increased PS and ceramide (Cer) in HTM cells (**Supplementary Figure 6G and 6H**,
498 respectively). However, sphingomyelin (SM) did not change after fatostatin treatment (**Supplementary**
499 **Figure 6I**). Looking at the KEGG human pathways (**Table 5**) based on total lipids changes we found that
500 major pathways affected due to fatostatin treatment were glycosylphosphatidylinositol inositol (GPI)-
501 anchor biosynthesis, glycerophospholipid metabolism, arachidonic acid metabolism, linoleic acid
502 metabolism, alpha-linoleic acid metabolism, biosynthesis of unsaturated fatty acids, sphingolipid
503 metabolism, and steroid biosynthesis. Together, this demonstrates that SREBPs inactivation using
504 fatostatin lowers lipid biosynthesis in HTM cells by decreasing the expression of SREBPs responsive
505 genes. Further, the potential role of lipids regulated by SREBPs in regulating IOP.
506

507 **3.6 SREBPs inactivation aids in the induction of cellular relaxation and focal adhesion signaling**

508 Since activation of SREBPs induced contractile phenotype in the cells, our logical step was to check if
509 SREBPs inactivation by fatostatin modulated actin polymerization and FA based cellular tension. We
510 probed for filamentous actin (F-actin) using phalloidin labeling in HTM cells along with FA proteins –
511 vinculin and paxillin. As seen in **Figures 6A and 6B**, compared to DMSO control, 24 h of 20 µM fatostatin
512 treatment on HTM cells demonstrated a marked decrease in the F-actin stress fibers (green staining in
513 merged/grayscale) and sparse distribution of vinculin and paxillin at the edges of F-actin fibers with
514 greater cytoplasmic accumulation (red staining in the merged/grayscale, indicated by white arrows). To
515 further confirm this result, we extracted F-actin and globular actin (G-actin) from control and fatostatin-
516 treated HTM cells separately and checked the changes in F-actin/G-actin ratio in each condition. **Figure**
517 **6C** shows that fatostatin significantly decreased F-actin/G-actin ratio (n = 4, p = 0.04), implying the

518 decreased actin polymerization under fatostatin treatment. Since changes in actin polymerization affect
519 cell contractility, we next assayed for the p-MLC/MLC ratio. Immunoblotting of the fatostatin treated
520 protein lysate showed a significant decrease in the ratio of p-MLC/MLC ratio (n = 4, p = 0.002) (**Figure**
521 **6D**), indicating that SREBPs inactivation can reduce HTM cell contractility. Finally, we examined the
522 expression of proteins involved in FA formation, F-actin polymerization, and their stabilization. Fascin is
523 a major F-actin bundling protein and regulates the maintenance and stability of parallel bundles of F-
524 actin in various cell types including TM (66),(20). Immunoblotting showed that fatostatin significantly
525 decreased fascin-1 levels (n = 4, p = 0.03) (**Figure 6E**) with no change in vinculin levels (n = 4, p = 0.6)
526 (**Figure 6E**). Suggesting that fatostatin destabilized the vinculin distribution at the edge of F-actin fibers,
527 but not vinculin levels. We found that fatostatin significantly decreased levels of LIM kinase 1 (LIMK1) (n
528 = 4, p = 0.04) (**Figure 6E**), an actin polymerization and stabilization protein (67). Looking at cofilin, we
529 found no significant change in the levels of total-cofilin (T-cofilin) (n = 4, p = 0.3), but phosphorylated
530 cofilin at serine 3 (P-cofilin) (n = 4, p = 0.003) and the ratio of P-cofilin/T-cofilin was significantly
531 decreased in fatostatin treatment (n = 4, p = 0.004) (**Figure 6F**). Therefore, providing evidence for
532 weakening the LIMK1-cofilin-driven actin polymerization. Moreover, we also found that fatostatin
533 treatment increased total-paxillin (T-paxillin) levels (n = 4, p = 0.07), and significantly decreased its
534 tyrosine 118 phosphorylated form (P-paxillin) (n = 4, p = 0.03). The ratio of P-paxillin/T-paxillin was
535 significantly decreased in fatostatin treatment (n = 4, p = 0.01) (**Figure 6G**), indicating decreased cellular
536 contractility and cell adhesive interactions.

537 **3.7 SREBPs activation is a critical regulator of ECM engagement to the matrix sites**

538 Alterations in actin and focal adhesions can have a direct impact on ECM adhesion (68). We found that
539 inhibition of SCAP-SREBP pathway using fatostatin (20 μM for 24 h) significantly decreased all ECM
540 mRNA expression, including FN (n = 4, p = 0.03), COL1α (n = 4, p = 0.0004), COL6α (n = 4, p = 0.01),
541 COL4α (n = 4, p = 0.002), tenascin C (TNC) (n = 4, p = 0.03), transforming growth factor β2 (TGFβ2) (n = 4,
542 p = 0.0003), and sarcospan (SSPN) (n = 4, p = 0.002) (**Figure 7A**). Consequently, upon fatostatin
543 treatment, the whole cell lysate (CL) protein expression analysis showed a significant reduction of FN (n
544 = 4, p = 0.01) and COL1A (n = 4, p = 0.001) (**Figure 7B**). In addition, secretory ECM levels FN (n = 4, p =
545 0.02) and COL1A (n = 4, p = 0.001) in conditioned media (CM) was significantly decreased (**Figure 7C**).
546 These results were confirmed using IF, where FN (**Figure 7D**) and COL1A (**Figure 7E**) immunolabeling
547 were robustly decreased.

548 Finally, to discern the role of SREBPs activation in the regulation of ECM recruitment to the matrix sites,
549 IF was performed for ECM like FN and COL1A (**Figure 7F and 7G,** green staining) under the expression of
550 constitutively active SREBP1a or 1c or 2 with the endogenous total SREBP activity inhibited using
551 fatostatin (20 μM for 24 h). The lower magnification images of the cells can be visualized in the
552 **Supplementary Figure 7**, with the box indicating the cells chosen for detailed explanation in **Figure 7F**
553 **and G**. In a compelling manner, the presence of Ad5-N-SREBP1a (**Figure 7F**, second-row third column),
554 Ad5-N-SREBP1c (**Figure 7F**, third-row third column), and Ad5-N-SREBP2 (**Figure 7F**, fourth-row third
555 column) induced higher FN perinuclear distribution inside the cell (denoted by yellow arrows) compared
556 to the AdMT control (**Figure 7F**, first-row third column). Similar pattern was observed for COL1A .
557 Compared to AdMT combined with fatostatin treatment (**Figure 7G**, first-row third column), Ad5-N-
558 SREBP1a (**Figure 7G**, second-row third column), Ad5-N-SREBP1c (**Figure 7G**, third-row third column), and
559 Ad5-N-SREBP2 (**Figure 7G**, fourth-row third column) combined with fatostatin treatment caused higher
560 COL1A distribution inside the cells, and more COL1A puncta mostly located near the cell membrane
561 (denoted by yellow arrows). We also observed a stronger COL1A fibril formation in Ad5-N-SREBP1a

562 (**Figure 7G**, second-row third column). Therefore, put together this data defines that SREBPs activation is
563 indispensable for ECM production, trafficking, and engagement to the matrix sites.

564 **4. Discussion:**

565 This study provides the first detailed evidence of the mechanosensing and mechanotransduction
566 role of SREBPs in TM. We have further established the cellular and molecular basis for the SREBPs
567 activation under increased mechanical stress in TM (38). Mechanosensing is an important function of
568 TM (69, 70) to maintain the IOP homeostasis (71) and excessive mechanotransduction in TM outflow
569 pathway can result in increased TM cell tension and stiffness (22, 72). Such changes have been
570 documented in experimental models of glaucoma (73) and in human glaucomatous TM (74). Moreover,
571 increased stiffness can lead to loss in mechanosensing function of the TM AH outflow pathway (75).
572 Here, we have established the positive feedforward loop connecting mechanical stress to actin-based
573 contractility via SREBP activation. The TM adapts to increased mechanical stress by modifying the actin
574 cytoskeleton and the ECM (38, 65). Augmenting SREBPs activation, induced contractility indicating a
575 perpetual feedforward signaling from mechanical stress sensing by SREBPs resulting in induction of
576 contractile force in the TM. Our study also demonstrates that inhibiting SREBPs activation mitigates
577 mechanical stress-induced actin stress fiber formation providing a strong basis for SREBPs acting as
578 mechanosensors and mechanotransducers. In fact, studies in cancer lines and *Drosophila* have
579 demonstrated that acto-myosin contractility and mechanical forces imposed by the ECM can regulate
580 SREBP1 (48). Interestingly, along with the mechanosensing function of SREBPs in TM and the expression
581 and distribution of SREBPs and SCAP in the TM-JCT outflow pathway compared to other tissues of the
582 ocular anterior segment suggested a potential role in IOP regulation. Likewise, we provide *ex vivo* and *in*
583 *vivo* based evidence to show that SREBPs activity plays an important role in the maintenance of IOP.
584 Both pharmacological and molecular inactivation of SREBPs significantly lowered IOP. We believe that
585 the effect of inhibiting a transcription factor will require a longer time to produce the effect but will be
586 longer lasting. We predict this because SREBPs inactivation will require regulation at the gene
587 expression level first followed by changes in protein/enzyme levels and finally effecting physiological
588 changes. Moreover, since anterior segment perfusion technique utilizes constant inflow, this also
589 directly proves that the IOP lowering is potentially by increasing the AH drainage via the TM outflow
590 pathway. Additionally, *in vivo* studies in *SCAP*$^{f/f}$ mice injected with Ad5.CMV.iCre-eGFP confirmed that
591 the molecular inactivation of SREBPs by knocking down SCAP significantly lowered IOP by 10 days post-
592 injection. Further studies to understand the role of SCAP-SREBP pathway in the SC and the distal outflow
593 pathways will be extremely significant. Studies on AH dynamics *in vivo* after inactivation or constitutively
594 activating SREBPs can provide additional insights into AH drainage modalities. Despite available IOP-
595 lowering drugs, there remains an unmet need for novel, efficacious, and mechanism-based targeted
596 therapy for ocular hypertension and POAG with minimal side effects (76). Testing the pharmacological
597 inactivation of SREBPs on IOP in animal models can help us identify novel topical drugs to lower IOP.
598 Curiously, there is evidence that SREBP1 activation and increased lipogenesis results in cellular
599 senescence (77). Interestingly in aging and glaucoma, it has been proposed that there is a gradual loss of
600 TM cellularity (78, 79). It will be key to unravel the role of SREBP isoforms – SREBP1 and SREBP2 - and
601 their activation paradigm in TM during aging, to elucidate the resultant effects TM cellularity and IOP,
602 and in the onset and progression of glaucoma pathogenesis.

603 The major function of SREBPs is regulating lipogenesis (42). In line, upon inactivation of the
604 SCAP-SREBP pathway, we found a significant decrease in total TM phospholipids (~90%) as well as in
605 cholesterol and triglycerides. The current understanding of the correlation between the regulation of
606 lipid levels in the TM outflow pathway with IOP changes is unclear. Lipids levels are known to be varied
607 in AH from ocular hypertensives and can participate in the pathogenesis of elevated IOP (29, 80-82).
608 Some well-studied lipids contributing to ocular hypertension are the bioactive lysophospholipids (lipid
609 growth factors) (30, 83-86), and cholesterol (31-33). Yet the causality has not been completely
610 attributed to increased lipids on IOP elevation. Based on recent epidemiologic studies, there is an
611 association between cholesterol and glaucoma, although the findings have not been conclusive if
612 hyperlipidemia is a cause or an effect of the disease. Some studies found that hyperlipidemia, especially
613 high cholesterol levels, is significantly associated with an increased risk of glaucoma and increased IOP
614 (32, 33, 87) (88) and others show the opposite (89) (90). Interestingly, even though it is not clear how
615 cholesterol is related to the glaucoma risk, there is mounting evidence showing that HMG-CoA
616 reductase inhibitor statin can decrease POAG risk by mitigating disease progression (35, 91, 92). The
617 proposed mechanism for statins to decrease IOP is by inhibiting the isoprenylation of Rho GTPase thus
618 resulting in decreased actomyosin contractile activity and ECM synthesis/assembly (36, 93-95). All these
619 studies imply that there is an association between lipids, ocular hypertension, and POAG. The data we
620 show clearly suggests that inactivating SCAP-SREBP pathway decreases TM lipids. Thus, connecting the
621 aspects of lowering lipids leading to IOP lowering. However, the contributions of lipid metabolism in TM
622 for the regulation of TM biomechanics and IOP are blurred (96). We have recently identified that TM
623 cholesterol plays a significant role in the maintenance of the polymerized state of actin, FA recruitment,
624 and TM membrane tension (*Unpublished study*). Thus, suggesting a strong contribution of lipids
625 including cholesterol in regulating TM actin-adhesion complex-ECM modulated via the SCAP-SREBP
626 pathway to efficiently maintain the IOP homeostasis.

627 This study strengthens the correlation between lipid changes and tissue stiffness and reinforces
628 the significance and role of actin-cell adhesive interactions in the regulation of IOP homeostasis (97). It
629 has been characterized that the FA vinculin but not paxillin directly interacts with actin (98, 99).
630 Additional mechanistic evidence in our study confirms that SREBPs inactivation regulates vinculin
631 distribution but not expression confirming the requirement of SREBPs activity in modulating the
632 recruitment of vinculin to the FA site. Also, a decrease in paxillin phosphorylation suggests a decreased
633 inside-out signaling towards integrin binding to ECM and recruitment of FA (100, 101). Inside the cells,
634 we identified that loss of SREBPs activation lowered the actin-bundling protein fascin-1 (20, 66, 102).
635 The decreased fascin-1 expression under fatostatin treatment can result in a slower rate of actin
636 polymerization with lesser filopodia formation (103, 104). Within this context, the decreased LIMK1
637 resulting in the loss of phosphorylation of cofilin-1 at serine 3 can induce F-actin destabilization and this
638 can prevent contraction and attenuate hypertension (67, 105). Thus, we propose that the loss of cell
639 adhesive interaction upon SREBPs inactivation is an important mechanism in lowering the IOP.
640 Interestingly, we found that there was a strong negative regulation of most of the ECM gene expression
641 upon fatostatin treatment in HTM cells. Though it is not yet clear if SREBPs directly regulate the
642 transcription of ECM genes, we believe this to be a result of negative feedback outside-in signaling
643 towards transcribing ECM genes due to the disengagement of ECM. *Ex vivo* evidence indicated a
644 significant loss in the ECM components like collagen and fibronectin in the outflow pathway which
645 concurred in the *in vitro* experiments in HTM cells. *In vitro* analysis provided further proof that the
646 inactivation of SREBPs decreased actin fibers and increased retraction of FAs to the cytosol with very

647 little found at the edges of the cells. The FAs aid in linking the intracellular cytoskeleton to the
648 extracellular ECM (106). A compromise in vinculin and paxillin localization at the edge of F-actin fibers
649 dictates the dissolution of FAs and decreased cell-ECM connections. Put together, the SCAP-SREBP
650 inactivation induced TM relaxation and ECM-based stiffness potentially by downregulating lipogenesis
651 resulting in IOP decrease.

652 Finally, of significant interest is the role of SREBPs activation in regulating the ECM engagement
653 to the membrane potentially for the release, modification, and cross-linking. This could be due to the
654 cellular and membrane lipid changes resulting from SREBPs activation. Additionally, we found marked
655 changes in the caveolar structures including the rosette formation upon SREBPs activation. These
656 structures could be involved in mechanosensing, mechanotransduction, possibly to mitigate mechanical
657 stress, and to buffer membrane tension (107-109). Moreover, multiple rate-limiting enzymes in lipid
658 biogenic pathways like FAS (49, 110), ACC (111, 112), HMGCR, and SREBPs are implicated in increasing
659 ECM and fibrosis in various tissue types (113-115). ACC catalyzes the carboxylation of acetyl-CoA into
660 malonyl-CoA. This reaction is the first and the rate-limiting step in the biosynthesis of fatty acids.
661 Significantly, acetyl-CoA metabolism is implicated in POAG (116). Further investigation on the role of
662 these rate limiting enzymes in controlling the metabolism and TM biomechanics is essential to decode
663 their function in IOP regulation. Though out of scope for this manuscript, we predict that SREBPs can
664 modulate ECM remodeling via lipid-independent pathways. SREBP1 has been shown to bind to the
665 promoter region of TGFβ (117), a major pro-fibrotic factor. Also, SREBP1 can act as a cell surface
666 retention factor for the TGFβ receptor, TβRI, by preventing its secretion in exosomes or directly
667 changing COL VI transcription (118) (119). Thus, pointing to the idea that SREBPs activation can increase
668 ECM production and deposition and IOP elevation in both lipid-dependent and -independent pathways.
669 Therefore, identifying all the gene promoters that SREBPs bind to in TM genome and teasing out the
670 lipid-dependent and -independent pathways responsible for modulating actin dynamics and ECM
671 remodeling in TM is essential.

672 **5. Conclusion**

673 In summary, this study presents a novel way of lowering IOP by inactivating SREBPs through
674 decreasing lipogenesis, actin-based tension, and attenuating ECM accumulation in TM. Thus,
675 demonstrating the important role of SREBPs in the regulation of TM contractility and stiffness, and IOP
676 regulation. Further modalities of SREBPs regulating the actin cytoskeleton and ECM in TM will aid in
677 identifying better targets for IOP lowering and glaucoma therapy.

678 **6. Conflict of Interest**

679 The authors declare that they have no conflict of interest. The funders had no role in the design
680 of the study; in the collection, analyses, or interpretation of data; in the writing of the manuscript, or in
681 the decision to publish the results.

682 **7. Data availability statement**

683 The datasets presented in this study is available upon request from the corresponding author.

684 **8. Author contributions**

685 Conceptualization: PPP. Methodology, cell cultures, immunohistochemistry, immunofluorescence
686 immunoblotting, qPCR: TW, AS, and JR. Animal work – Animal Breeding & Injection: AJ, TW, AS, and PPP.
687 Formal analysis: TW, AS, and PPP. Investigation: TW, AS, JR, and PPP. Lipidomics data collection, data
688 analysis, and pathway analysis: TW. Write-up and data curation: TW, AS, and PPP. Writing—original
689 draft preparation: TW and PPP. Figure preparation: TW and PPP. Visualization: TW, AS, and PPP:
690 supervision: PPP: project administration: PPP: funding acquisition: PPP. All authors have read and
691 approved the manuscript.

692 **9. Funding**

693 This project was supported by the National Institutes of Health/ National Eye Institute
694 (R01EY029320) (PPP), Glick Research Endowment Funds (PPP), Cohen AMD Research Pilot Grant (PPP),
695 RPB Departmental Pilot Grant (PPP), Sigma Xi Grant-in-aid (TW) and grant from Research to Prevent
696 Blindness to IU.

697 **10. Acknowledgments**

698 We would like to acknowledge Dr. Nuria Morral, Dr. Benjamin Perrin, Dr. Gary Landreth, and Dr.
699 Tim Corson from IUSM for their useful discussions on the project. Derrick Gray from Center for Electron
700 Microscopy (iCEM) and Instrumentation grant from the NIH - 1S10OD028723 to iCEM. We thank Dr.
701 Christina Ferreira from the Bindley Bioscience Center, Purdue University, for the discussions, planning,
702 and help with the execution of the MRM-based Lipidomics analysis, and data analysis.

703 **11. References**

704 1. R. N. Weinreb, P. T. Khaw, Primary open-angle glaucoma. *Lancet* **363**, 1711-1720 (2004).
705 2. W. M. Grant, Clinical tonography. *Trans Am Acad Ophthalmol Otolaryngol* **55**, 774-781 (1951).
706 3. W. M. Grant, Experimental aqueous perfusion in enucleated human eyes. *Arch Ophthalmol* **69**,
707 783-801 (1963).
708 4. N. A. Sharif, Therapeutic Drugs and Devices for Tackling Ocular Hypertension and Glaucoma, and
709 Need for Neuroprotection and Cytoprotective Therapies. *Frontiers in pharmacology* **12**, 729249
710 (2021).
711 5. Y. Shiose, Intraocular pressure: new perspectives. *Surv Ophthalmol* **34**, 413-435 (1990).
712 6. L. Bonomi *et al.*, Prevalence of glaucoma and intraocular pressure distribution in a defined
713 population. The Egna-Neumarkt Study. *Ophthalmology* **105**, 209-215 (1998).
714 7. I. Dielemans *et al.*, Primary open-angle glaucoma, intraocular pressure, and systemic blood
715 pressure in the general elderly population. The Rotterdam Study. *Ophthalmology* **102**, 54-60
716 (1995).
717 8. H. A. Quigley, Open-angle glaucoma. *The New England journal of medicine* **328**, 1097-1106
718 (1993).
719 9. J. B. Saaddine, K. M. Narayan, F. Vinicor, Vision loss: a public health problem? *Ophthalmology*
720 **110**, 253-254 (2003).
721 10. Y. C. Tham *et al.*, Global prevalence of glaucoma and projections of glaucoma burden through
722 2040: a systematic review and meta-analysis. *Ophthalmology* **121**, 2081-2090 (2014).
723 11. H. A. Quigley, A. T. Broman, The number of people with glaucoma worldwide in 2010 and 2020.
724 *British journal of ophthalmology* **90**, 262-267 (2006).
725 12. M. A. Kass *et al.*, The Ocular Hypertension Treatment Study: a randomized trial determines that
726 topical ocular hypotensive medication delays or prevents the onset of primary open-angle
727 glaucoma. *Arch Ophthalmol* **120**, 701-713; discussion 829-730 (2002).

13. A. F. Clark, T. Yorio, Ophthalmic drug discovery. *Nat Rev Drug Discov* **2**, 448-459 (2003).
14. A. J. Lee, I. Goldberg, Emerging drugs for ocular hypertension. *Expert Opin Emerg Drugs* **16**, 137-161 (2011).
15. L. Crawley, S. M. Zamir, M. F. Cordeiro, L. Guo, Clinical options for the reduction of elevated intraocular pressure. *Ophthalmol Eye Dis* **4**, 43-64 (2012).
16. D. K. Sunderland, A. Sapra, "Physiology, Aqueous Humor Circulation" in StatPearls. (Treasure Island (FL), 2022).
17. W. D. Stamer, The cell and molecular biology of glaucoma: mechanisms in the conventional outflow pathway. *Invest Ophthalmol Vis Sci* **53**, 2470-2472 (2012).
18. D. W. Abu-Hassan, T. S. Acott, M. J. Kelley, The Trabecular Meshwork: A Basic Review of Form and Function. *J Ocul Biol* **2** (2014).
19. T. Carreon, E. van der Merwe, R. L. Fellman, M. Johnstone, S. K. Bhattacharya, Aqueous outflow - A continuum from trabecular meshwork to episcleral veins. *Prog Retin Eye Res* **57**, 108-133 (2017).
20. A. Soundararajan, S. A. Ghag, S. S. Vuda, T. Wang, P. P. Pattabiraman, Cathepsin K Regulates Intraocular Pressure by Modulating Extracellular Matrix Remodeling and Actin-Bundling in the Trabecular Meshwork Outflow Pathway. *Cells* **10**, 2864 (2021).
21. P. P. Pattabiraman, C. B. Toris, The exit strategy: Pharmacological modulation of extracellular matrix production and deposition for better aqueous humor drainage. *Eur J Pharmacol* **787**, 32-42 (2016).
22. P. P. Pattabiraman *et al.*, RhoA GTPase-induced ocular hypertension in a rodent model is associated with increased fibrogenic activity in the trabecular meshwork. *The American journal of pathology* **185**, 496-512 (2015).
23. K. Wang, A. T. Read, T. Sulchek, C. R. Ethier, Trabecular meshwork stiffness in glaucoma. *Exp Eye Res* **158**, 3-12 (2017).
24. J. A. Vranka, M. J. Kelley, T. S. Acott, K. E. Keller, Extracellular matrix in the trabecular meshwork: intraocular pressure regulation and dysregulation in glaucoma. *Exp Eye Res* **133**, 112-125 (2015).
25. E. R. Tamm, B. M. Braunger, R. Fuchshofer, Intraocular Pressure and the Mechanisms Involved in Resistance of the Aqueous Humor Flow in the Trabecular Meshwork Outflow Pathways. *Prog Mol Biol Transl Sci* **134**, 301-314 (2015).
26. P. Liu, F. Wang, Y. Song, M. Wang, X. Zhang, Current situation and progress of drugs for reducing intraocular pressure. *Therapeutic advances in chronic disease* **13**, 20406223221140392 (2022).
27. J. D. Humphrey, E. R. Dufresne, M. A. Schwartz, Mechanotransduction and extracellular matrix homeostasis. *Nature reviews. Molecular cell biology* **15**, 802-812 (2014).
28. N. V. Azbukina *et al.*, Targeted Lipidomic Analysis of Aqueous Humor Reveals Signaling Lipid-Mediated Pathways in Primary Open-Angle Glaucoma. *Biology (Basel)* **10**, 658 (2021).
29. G. Edwards *et al.*, Endogenous ocular lipids as potential modulators of intraocular pressure. *J Cell Mol Med* **24**, 3856-3900 (2020).
30. P. V. Rao, Bioactive lysophospholipids: role in regulation of aqueous humor outflow and intraocular pressure in the context of pathobiology and therapy of glaucoma. *J Ocul Pharmacol Ther* **30**, 181-190 (2014).
31. K. M. Madjedi *et al.*, The Association between Serum Lipids and Intraocular Pressure in 2 Large United Kingdom Cohorts. *Ophthalmology* **129**, 986-996 (2022).
32. L. Posch-Pertl *et al.*, Cholesterol and glaucoma: a systematic review and meta-analysis. *Acta Ophthalmol* **100**, 148-158 (2022).
33. S. Wang, X. Bao, Hyperlipidemia, Blood Lipid Level, and the Risk of Glaucoma: A Meta-Analysis. *Invest Ophthalmol Vis Sci* **60**, 1028-1043 (2019).

775 34. M. W. Marcus *et al.*, Cholesterol-lowering drugs and incident open-angle glaucoma: a
776 population-based cohort study. *PloS one* **7**, e29724 (2012).
777 35. J. D. Stein *et al.*, The relationship between statin use and open-angle glaucoma. *Ophthalmology*
778 **119**, 2074-2081 (2012).
779 36. J. Song, P. F. Deng, S. S. Stinnett, D. L. Epstein, P. V. Rao, Effects of cholesterol-lowering statins
780 on the aqueous humor outflow pathway. *Invest Ophthalmol Vis Sci* **46**, 2424-2432 (2005).
781 37. C. L. Von Zee, M. P. Richards, P. Bu, J. I. Perlman, E. B. Stubbs, Jr., Increased RhoA and RhoB
782 protein accumulation in cultured human trabecular meshwork cells by lovastatin. *Invest*
783 *Ophthalmol Vis Sci* **50**, 2816-2823 (2009).
784 38. A. Soundararajan *et al.*, Multiomics analysis reveals the mechanical stress-dependent changes in
785 trabecular meshwork cytoskeletal-extracellular matrix interactions. *Front Cell Dev Biol* **10**,
786 874828 (2022).
787 39. H. Shimano, R. Sato, SREBP-regulated lipid metabolism: convergent physiology - divergent
788 pathophysiology. *Nat Rev Endocrinol* **13**, 710-730 (2017).
789 40. H. Shimano, Sterol regulatory element-binding proteins (SREBPs): transcriptional regulators of
790 lipid synthetic genes. *Prog Lipid Res* **40**, 439-452 (2001).
791 41. D. Eberle, B. Hegarty, P. Bossard, P. Ferre, F. Foufelle, SREBP transcription factors: master
792 regulators of lipid homeostasis. *Biochimie* **86**, 839-848 (2004).
793 42. J. D. Horton, J. L. Goldstein, M. S. Brown, SREBPs: activators of the complete program of
794 cholesterol and fatty acid synthesis in the liver. *J Clin Invest* **109**, 1125-1131 (2002).
795 43. J. L. Goldstein, R. A. DeBose-Boyd, M. S. Brown, Protein sensors for membrane sterols. *Cell* **124**,
796 35-46 (2006).
797 44. D. Dorotea, D. Koya, H. Ha, Recent Insights Into SREBP as a Direct Mediator of Kidney Fibrosis via
798 Lipid-Independent Pathways. *Front Pharmacol* **11**, 265 (2020).
799 45. M. Matsuda *et al.*, SREBP cleavage-activating protein (SCAP) is required for increased lipid
800 synthesis in liver induced by cholesterol deprivation and insulin elevation. *Genes Dev* **15**, 1206-
801 1216 (2001).
802 46. J. Sakai, A. Nohturfft, J. L. Goldstein, M. S. Brown, Cleavage of sterol regulatory element-binding
803 proteins (SREBPs) at site-1 requires interaction with SREBP cleavage-activating protein. Evidence
804 from in vivo competition studies. *J Biol Chem* **273**, 5785-5793 (1998).
805 47. S. Daemen, M. Kutmon, C. T. Evelo, A pathway approach to investigate the function and
806 regulation of SREBPs. *Genes Nutr* **8**, 289-300 (2013).
807 48. R. Bertolio *et al.*, Sterol regulatory element binding protein 1 couples mechanical cues and lipid
808 metabolism. *Nat Commun* **10**, 1326 (2019).
809 49. X. Zhao, J. Y. Y. Kwan, K. Yip, P. P. Liu, F. F. Liu, Targeting metabolic dysregulation for fibrosis
810 therapy. *Nat Rev Drug Discov* **19**, 57-75 (2020).
811 50. G. Proctor *et al.*, Regulation of renal fatty acid and cholesterol metabolism, inflammation, and
812 fibrosis in Akita and OVE26 mice with type 1 diabetes. *Diabetes* **55**, 2502-2509 (2006).
813 51. J. H. Lee *et al.*, SREBP-1a-stimulated lipid synthesis is required for macrophage phagocytosis
814 downstream of TLR4-directed mTORC1. *Proc Natl Acad Sci U S A* **115**, E12228-e12234 (2018).
815 52. G. Sorrentino *et al.*, Metabolic control of YAP and TAZ by the mevalonate pathway. *Nat Cell Biol*
816 **16**, 357-366 (2014).
817 53. K. E. Keller *et al.*, Consensus recommendations for trabecular meshwork cell isolation,
818 characterization and culture. *Exp Eye Res* **171**, 164-173 (2018).
819 54. A. Soundararajan, T. Wang, S. A. Ghag, M. H. Kang, P. P. Pattabiraman, Novel insight into the
820 role of clusterin on intraocular pressure regulation by modifying actin polymerization and
821 extracellular matrix remodeling in the trabecular meshwork. *J Cell Physiol* **237**, 3012-3029 (2022).

822 55. X. Cheng, J. Li, D. Guo, SCAP/SREBPs are Central Players in Lipid Metabolism and Novel
823 Metabolic Targets in Cancer Therapy. *Curr Top Med Chem* **18**, 484-493 (2018).
824 56. S. Kamisuki *et al.*, A small molecule that blocks fat synthesis by inhibiting the activation of SREBP.
825 *Chem Biol* **16**, 882-892 (2009).
826 57. S. H. Lee, J. H. Lee, S. S. Im, The cellular function of SCAP in metabolic signaling. *Exp Mol Med* **52**,
827 724-729 (2020).
828 58. L. Jiajia *et al.*, Assessment of Neuronal Viability Using Fluorescein Diacetate-Propidium Iodide
829 Double Staining in Cerebellar Granule Neuron Culture. *J Vis Exp* 10.3791/55442 (2017).
830 59. M. Matsuda *et al.*, SREBP cleavage-activating protein (SCAP) is required for increased lipid
831 synthesis in liver induced by cholesterol deprivation and insulin elevation. *Genes & development*
832 **15**, 1206-1216 (2001).
833 60. Y. Kidani *et al.*, Sterol regulatory element–binding proteins are essential for the metabolic
834 programming of effector T cells and adaptive immunity. *Nature Immunology* **14**, 489-499 (2013).
835 61. K. J. Livak, T. D. Schmittgen, Analysis of relative gene expression data using real-time
836 quantitative PCR and the 2(-Delta Delta C(T)) Method. *Methods* **25**, 402-408 (2001).
837 62. P. P. Pattabiraman, P. V. Rao, Mechanistic basis of Rho GTPase-induced extracellular matrix
838 synthesis in trabecular meshwork cells. *Am J Physiol Cell Physiol* **298**, C749-763 (2010).
839 63. E. G. Bligh, W. J. Dyer, A rapid method of total lipid extraction and purification. *Can J Biochem*
840 *Physiol* **37**, 911-917 (1959).
841 64. T. Wang, P. P. Pattabiraman, Analysis of Lipid Contents in Human Trabecular Meshwork Cells by
842 Multiple Reaction Monitoring (MRM) Profiling Lipidomics. *Methods Mol Biol* **2625**, 291-298
843 (2023).
844 65. P. P. Pattabiraman, T. Inoue, P. V. Rao, Elevated intraocular pressure induces Rho GTPase
845 mediated contractile signaling in the trabecular meshwork. *Exp Eye Res* **136**, 29-33 (2015).
846 66. J. Zanet *et al.*, Fascin promotes filopodia formation independent of its role in actin bundling.
847 *Journal of Cell Biology* **197**, 477-486 (2012).
848 67. O. Bernard, Lim kinases, regulators of actin dynamics. *Int J Biochem Cell Biol* **39**, 1071-1076
849 (2007).
850 68. C. Wu, Focal adhesion: a focal point in current cell biology and molecular medicine. *Cell Adh*
851 *Migr* **1**, 13-18 (2007).
852 69. D. WuDunn, Mechanobiology of trabecular meshwork cells. *Exp Eye Res* **88**, 718-723 (2009).
853 70. D. C. Turner *et al.*, Transient Intraocular Pressure Fluctuations: Source, Magnitude, Frequency,
854 and Associated Mechanical Energy. *Invest Ophthalmol Vis Sci* **60**, 2572-2582 (2019).
855 71. C. Xin, N. Tian, M. Li, H. Wang, N. Wang, Mechanism of the reconstruction of aqueous outflow
856 drainage. *Sci China Life Sci* **61**, 534-540 (2018).
857 72. P. V. Rao, P. P. Pattabiraman, C. Kopczynski, Role of the Rho GTPase/Rho kinase signaling
858 pathway in pathogenesis and treatment of glaucoma: Bench to bedside research. *Exp Eye Res*
859 **158**, 23-32 (2017).
860 73. A. Vahabikashi *et al.*, Increased stiffness and flow resistance of the inner wall of Schlemm's canal
861 in glaucomatous human eyes. *Proceedings of the National Academy of Sciences* **116**, 26555-
862 26563 (2019).
863 74. J. A. Last *et al.*, Elastic modulus determination of normal and glaucomatous human trabecular
864 meshwork. *Invest Ophthalmol Vis Sci* **52**, 2147-2152 (2011).
865 75. K. Gao *et al.*, Reduced Pulsatile Trabecular Meshwork Motion in Eyes With Primary Open Angle
866 Glaucoma Using Phase-Sensitive Optical Coherence Tomography. *Invest Ophthalmol Vis Sci* **61**,
867 21 (2020).
868 76. A. Sheybani *et al.*, Open-Angle Glaucoma: Burden of Illness, Current Therapies, and the
869 Management of Nocturnal IOP Variation. *Ophthalmol Ther* **9**, 1-14 (2020).

77. Y. M. Kim *et al.*, Sterol regulatory element-binding protein (SREBP)-1-mediated lipogenesis is involved in cell senescence. *The Journal of biological chemistry* **285**, 29069-29077 (2010).
78. J. Alvarado, C. Murphy, R. Juster, Trabecular meshwork cellularity in primary open-angle glaucoma and nonglaucomatous normals. *Ophthalmology* **91**, 564-579 (1984).
79. J. Alvarado, C. Murphy, J. Polansky, R. Juster, Age-related changes in trabecular meshwork cellularity. *Invest Ophthalmol Vis Sci* **21**, 714-727 (1981).
80. G. Edwards, K. Aribindi, Y. Guerra, S. K. Bhattacharya, Sphingolipids and ceramides of mouse aqueous humor: Comparative profiles from normotensive and hypertensive DBA/2J mice. *Biochimie* **105**, 99-109 (2014).
81. G. Edwards, K. Aribindi, Y. Guerra, R. K. Lee, S. K. Bhattacharya, Phospholipid profiles of control and glaucomatous human aqueous humor. *Biochimie* **101**, 232-247 (2014).
82. H. Wang, G. Edwards, C. Garzon, C. Piqueras, S. K. Bhattacharya, Aqueous humor phospholipids of DBA/2J and DBA/2J-Gpnmb(+)/SjJ mice. *Biochimie* **113**, 59-68 (2015).
83. P. S. Mettu *et al.*, Role of lysophospholipid growth factors in the modulation of aqueous humor outflow facility. *Invest Ophthalmol Vis Sci* **45**, 2263-2271 (2004).
84. L. T. Y. Ho *et al.*, Role of the autotaxin-lysophosphatidic acid axis in glaucoma, aqueous humor drainage and fibrogenic activity. *Biochimica et Biophysica Acta (BBA) - Molecular Basis of Disease* **1866**, 165560 (2020).
85. M. Honjo *et al.*, Autotaxin–Lysophosphatidic Acid Pathway in Intraocular Pressure Regulation and Glaucoma Subtypes. *Investigative Ophthalmology & Visual Science* **59**, 693-701 (2018).
86. P. Iyer *et al.*, Autotaxin-lysophosphatidic acid axis is a novel molecular target for lowering intraocular pressure. *PloS one* **7**, e42627 (2012).
87. H. C. Lin, C. W. Chien, C. C. Hu, J. D. Ho, Comparison of comorbid conditions between open-angle glaucoma patients and a control cohort: a case-control study. *Ophthalmology* **117**, 2088-2095 (2010).
88. S. Pavljasević, M. Asćerić, Primary open-angle glaucoma and serum lipids. *Bosn J Basic Med Sci* **9**, 85-88 (2009).
89. P. A. Newman-Casey, N. Talwar, B. Nan, D. C. Musch, J. D. Stein, The relationship between components of metabolic syndrome and open-angle glaucoma. *Ophthalmology* **118**, 1318-1326 (2011).
90. W. C. Stewart, C. Sine, S. Sutherland, J. A. Stewart, Total cholesterol and high-density lipoprotein levels as risk factors for increased intraocular pressure. *Am J Ophthalmol* **122**, 575-577 (1996).
91. P. McCann, R. E. Hogg, R. Fallis, A. Azuara-Blanco, The Effect of Statins on Intraocular Pressure and on the Incidence and Progression of Glaucoma: A Systematic Review and Meta-Analysis. *Investigative Ophthalmology & Visual Science* **57**, 2729-2748 (2016).
92. N. Talwar, D. C. Musch, J. D. Stein, Association of Daily Dosage and Type of Statin Agent With Risk of Open-Angle Glaucoma. *JAMA ophthalmology* **135**, 263-267 (2017).
93. X. Y. Song *et al.*, Atorvastatin reduces IOP in ocular hypertension in vivo and suppresses ECM in trabecular meshwork perhaps via FGD4. *Int J Mol Med* **49** (2022).
94. L. Cong, S. Fu, J. Zhang, J. Zhao, Y. Zhang, Effects of atorvastatin on porcine aqueous humour outflow and trabecular meshwork cells. *Exp Ther Med* **15**, 210-216 (2018).
95. C. L. Von Zee, E. B. Stubbs, Jr., Geranylgeranylation facilitates proteasomal degradation of rho G-proteins in human trabecular meshwork cells. *Invest Ophthalmol Vis Sci* **52**, 1676-1683 (2011).
96. M. Lakk *et al.*, Membrane cholesterol regulates TRPV4 function, cytoskeletal expression, and the cellular response to tension. *Journal of lipid research* **62**, 100145-100145 (2021).
97. Y. F. Yang, Y. Y. Sun, D. M. Peters, K. E. Keller, The Effects of Mechanical Stretch on Integrins and Filopodial-Associated Proteins in Normal and Glaucomatous Trabecular Meshwork Cells. *Front Cell Dev Biol* **10**, 886706 (2022).

98. J. D. Humphries *et al.*, Vinculin controls focal adhesion formation by direct interactions with talin and actin. *The Journal of cell biology* **179**, 1043-1057 (2007).
99. M. Reinhard, M. Rüdiger, B. M. Jockusch, U. Walter, VASP interaction with vinculin: a recurring theme of interactions with proline-rich motifs. *FEBS Lett* **399**, 103-107 (1996).
100. S. L. Bellis, J. T. Miller, C. E. Turner, Characterization of tyrosine phosphorylation of paxillin in vitro by focal adhesion kinase. *The Journal of biological chemistry* **270**, 17437-17441 (1995).
101. A. M. López-Colomé, I. Lee-Rivera, R. Benavides-Hidalgo, E. López, Paxillin: a crossroad in pathological cell migration. *J Hematol Oncol* **10**, 50 (2017).
102. L. M. Machesky, A. Li, Fascin: Invasive filopodia promoting metastasis. *Commun Integr Biol* **3**, 263-270 (2010).
103. R. Jaiswal *et al.*, The Formin Daam1 and Fascin Directly Collaborate to Promote Filopodia Formation. *Current Biology* **23**, 1373-1379 (2013).
104. D. Vignjevic *et al.*, Role of fascin in filopodial protrusion. *Journal of Cell Biology* **174**, 863-875 (2006).
105. M. Morales-Quinones *et al.*, LIMK (LIM Kinase) Inhibition Prevents Vasoconstriction- and Hypertension-Induced Arterial Stiffening and Remodeling. *Hypertension* **76**, 393-403 (2020).
106. B. Geiger, A. Bershadsky, R. Pankov, K. M. Yamada, Transmembrane crosstalk between the extracellular matrix--cytoskeleton crosstalk. *Nat Rev Mol Cell Biol* **2**, 793-805 (2001).
107. L. Sotodosos-Alonso, M. Pulgarín-Alfaro, M. A. del Pozo, Caveolae Mechanotransduction at the Interface between Cytoskeleton and Extracellular Matrix. *Cells* **12**, 942 (2023).
108. M. H. Elliott *et al.*, Caveolin-1 modulates intraocular pressure: implications for caveolae mechanoprotection in glaucoma. *Scientific Reports* **6**, 37127 (2016).
109. G. Golani, N. Ariotti, R. G. Parton, M. M. Kozlov, Membrane Curvature and Tension Control the Formation and Collapse of Caveolar Superstructures. *Developmental Cell* **48**, 523-538.e524 (2019).
110. M. Y. Jung *et al.*, Fatty acid synthase is required for profibrotic TGF-beta signaling. *FASEB J* **32**, 3803-3815 (2018).
111. M. Lee *et al.*, Phosphorylation of Acetyl-CoA Carboxylase by AMPK Reduces Renal Fibrosis and Is Essential for the Anti-Fibrotic Effect of Metformin. *J Am Soc Nephrol* **29**, 2326-2336 (2018).
112. J. Bates *et al.*, Acetyl-CoA carboxylase inhibition disrupts metabolic reprogramming during hepatic stellate cell activation. *J Hepatol* **73**, 896-905 (2020).
113. S.-N. Lin *et al.*, Development of antifibrotic therapy for stricturing Crohn's disease: lessons from randomized trials in other fibrotic diseases. *Physiological Reviews* **102**, 605-652 (2022).
114. M. Martin *et al.*, Role of endothelial cells in pulmonary fibrosis via SREBP2 activation. *JCI Insight* **6** (2021).
115. M. Matsumoto *et al.*, Acetyl-CoA carboxylase 1 and 2 inhibition ameliorates steatosis and hepatic fibrosis in a MC4R knockout murine model of nonalcoholic steatohepatitis. *PloS one* **15**, e0228212-e0228212 (2020).
116. J. N. C. Bailey *et al.*, Hypothesis-independent pathway analysis implicates GABA and Acetyl-CoA metabolism in primary open-angle glaucoma and normal-pressure glaucoma. *Hum Genet* **133**, 1319-1330 (2014).
117. L. Uttarwar, B. Gao, A. J. Ingram, J. C. Krepinsky, SREBP-1 activation by glucose mediates TGF-β upregulation in mesangial cells. *Am J Physiol Renal Physiol* **302**, F329-341 (2012).
118. A. Ferrari, S. Maretto, D. Girotto, D. Volpin, G. M. Bressan, SREBP contributes to induction of collagen VI transcription by serum starvation. *Biochem Biophys Res Commun* **313**, 600-605 (2004).

964 119. R. Van Krieken *et al.*, Sterol Regulatory Element Binding Protein (SREBP)-1 is a novel regulator of
965 the Transforming Growth Factor (TGF)-β receptor I (TβRI) through exosomal secretion. *Cell*
966 *Signal* **29**, 158-167 (2017).

967

968 **Figure Legends:**

969 **Figure 1: Mechanical stress on trabecular meshwork induces SREBPs activation.**

970 (**A**) and (**B**) Localization of SREBPs in HTM cells subjected to cyclic mechanical stretch was checked using
971 immunofluorescence (IF). After 2 h of mechanical stress, HTM cells show a strong nuclear localization of
972 both SREBP1 and SREBP2 (second-row third column). Phalloidin was used to stain the distribution of
973 filamentous actin (F-actin) fiber in the cells. After 2 h of mechanical stress, there was increased F-actin
974 distribution inside the HTM cells (second-row fourth column). 2 h stretch combined with fatostatin
975 treatment shows decreased nuclear localization of both SREBP1 and SREBP2 (third-row third column)
976 and decreased F-actin distribution inside the HTM cells (third-row fourth column). Quantification of
977 immunofluorescence images using ImageJ-based fluorescence intensity measurements shows a
978 significant increase in both nuclear SREBP1 and nuclear SREBP2's mean fluorescence intensity in 2 h
979 stretched HTM cells and a significant decrease of them in 2 h stretch combined with fatostatin
980 treatment (right panel). The nucleus was stained with DAPI in blue. Images were captured in z-stack in a
981 confocal microscope, and stacks were orthogonally projected. Scale bar 20 micron. (**C**) Protein
982 expression of both nuclear form SREBP1 (N-SREBP1) and SREBP2 (N-SREBP2) was significantly increased
983 in TM derived from enucleated porcine anterior segments perfused under the elevated pressure of 30
984 mmHg for 5 h compared with 15 mmHg. The results were based on semi-quantitative immunoblotting
985 with subsequent densitometric analysis. β-actin was used as a loading control. Values represent the
986 mean ± SEM, where n = 4-40 (biological replicates). $*p < 0.05$ was considered statistically significant. CTL:
987 un-stretched control HTM cells, ST: stretched HTM cells.

988 **Figure 2: Constitutive induction of SREBPs activation modulates actin and focal adhesion dynamics.**

989 (**A**) and (**B**) Immunofluorescence (IF) shows the distribution of SREBP1, SREBP2, filamentous actin (F-
990 actin) fibers, and vinculin in HTM cells under AdMT and Ad5-N-SREBPs treatments. (**A**) Ad5-N-SREBP1a
991 (second-row third column), and Ad5-N-SREBP1c (third-row third column) induced strong staining of
992 SREBP1 in the nucleus in HTM cells compared to AdMT (first-row third column). Similarly, (**B**) Ad5-N-
993 SREBP2 (second-row third column) induced strong staining of SREBP2 in the nucleus in HTM cells
994 compared to AdMT (first-row third column). Compared to AdMT (first-row fifth column), (**A**) Ad5-N-
995 SREBP1a (second-row fifth column) and Ad5-N-SREBP1c (third-row fifth column), and (**B**) Ad5-N-SREBP2
996 (second-row fifth column) caused the increased distribution of F-actin fibers stained by phalloidin
997 (purple/grayscale) in HTM cells and induced increased lamellipodia and filopodia formation (indicated by
998 yellow arrows). (**A**) Ad5-N-SREBP1a (second-row fourth column), Ad5-N-SREBP1c (third-row fourth
999 column), and (**B**) Ad5-N-SREBP2 (second-row fourth column) also induced more distribution of vinculin
1000 (green/grayscale) at the edges of F-actin fibers (indicated by white arrows) in HTM cells compared to the
1001 AdMT (first-row fourth column). The nucleus was stained with DAPI in blue. Images were captured in z-
1002 stack in a confocal microscope, and stacks were orthogonally projected. Scale bar 20 micron. (**C**)
1003 Immunofluorescence (IF) shows the distribution of Arp2/3 and RAPH1 in HTM cells under AdMT and
1004 Ad5-N-SREBPs treatment. Compared to AdMT, Ad5-N-SREBPs induced the distribution of Arp2/3 and

1005 RAPH1 at the cell membrane and near the filopodia structures. Images were captured in z-stack in a
1006 confocal microscope, and stacks were orthogonally projected. Scale bar 5 micron. (**D**) Transmission
1007 electron microscope (TEM) image of HTM cells under AdMT and Ad5-N-SREBPs treatment. Compared to
1008 AdMT, Ad5-N-SREBP1a, Ad5-N-SREBP1c, and Ad5-N-SREBP2 induced membrane bending and filopodia
1009 formation. Scale bar as shown in the figure.

1010 **Figure 3: Pharmacological inhibition of SCAP-SREBP pathway lowers IOP.**

1011 (**A**) Nuclear fraction from PTM cells after 20 µM fatostatin for 24 h treatment. Immunoblotting result
1012 shows that both N-SREBP1 (left panel) and N-SREBP2 (right panel) were significantly decreased. Lamin
1013 B1 was used as a loading control. (**B**) Primary HTM cells were treated with 20 µM fatostatin for 24 h, and
1014 immunoblotting results show that both N-SREBP1 (left panel) and N-SREBP2 (middle panel) were
1015 significantly decreased under fatostatin treatment, but SCAP protein expression level was no significant
1016 difference in two groups (right panel). GAPDH was used as a loading control. (**C**) and (**D**)
1017 Immunofluorescence (IF) shows the changes in SREBP1 and SREBP2 distribution in HTM cells after 20
1018 µM fatostatin treatment (left panel). In the fatostatin treated HTM cells, less SREBP1 (green staining)
1019 and SREBP2 (green staining) were distributed inside the nucleus (second row), compared to DMSO
1020 treated control HTM cells (first row). The nucleus was stained with DAPI in blue. Images were captured
1021 in z-stack in a confocal microscope, and stacks were orthogonally projected. Scale bar 20 microns.
1022 Quantification of immunofluorescence images using ImageJ-based fluorescence intensity measurements
1023 shows a significant decrease in both nuclear SREBP1 and nuclear SREBP2's mean fluorescence intensity
1024 in fatostatin treated HTM cells (right panel). Freshly enucleated porcine eyes were perfused with 20 µM
1025 fatostatin or DMSO control after baseline was established with perfusion media containing D-glucose at
1026 37 °C. (**E**) Graphical representation of relative fold change in IOP showed a significant decrease post 12 h
1027 of fatostatin perfusion (red line) and remained significant until 22 h compared to vehicle DMSO perfused
1028 control (blue line). (**F**) Histological examination of the outflow pathway tissues using Hematoxylin and
1029 Eosin (H and E) staining showed increased spacing between the TM in the fatostatin perfused eyes
1030 compared to a more compact TM in the DMSO perfused eyes. Scale bar 100 micron. (**G**) Quantitative
1031 analysis of protein expression from 20 µM fatostatin perfused TM tissues showed a significant decrease
1032 in N-SREBP1 and N-SREBP2, compared to vehicle DMSO perfused control. Lamin B1 was used as a
1033 loading control. (**H**) Immunolocalization of ECM proteins, including COL1A and FN (green staining) in the
1034 outflow pathway tissue in DMSO control or fatostatin. In the fatostatin perfused eyes, COL1A and FN
1035 (left panel second column) showed a decreased distribution in the TM-JCT region. TM indicates
1036 trabecular meshwork. AP indicates aqueous plexus. Images were captured in z-stack in a confocal
1037 microscope, and stacks were orthogonally projected. Scale bar 50 micron. Quantification of
1038 immunofluorescence images using ImageJ-based fluorescence intensity measurements showed a
1039 significant decrease in the fluorescence intensity of COL1A and FN in the TM outflow pathway (right
1040 panel). (**I**) Quantitative analysis of protein expression from 20 µM fatostatin perfused TM tissues
1041 showed a significant decrease in COL1A, and FN compared to vehicle DMSO perfused control. Lamin B1
1042 was used as a loading control. Values represent the mean ± SEM, where n = 4-5 (biological replicates).
1043 *$p < 0.05$ was considered statistically significant.

1044 **Figure 4: Molecular inactivation of SREBPs by SCAP knockdown lowers IOP**

1045 (**A**) Starting from 10 days after saline and adenovirus injection, IOP was significantly decreased in
1046 Ad5.CMV.iCre-eGFP injection group compared to the untouched group, saline injection group, and

1047 Ad5.CMV.eGFP injection group. This significant reduction in IOP in Ad5.CMV.iCre-eGFP injection group
1048 was sustained until 30 days post-injection. On 40 days and 50 days post-injection, compared to saline
1049 injection group and Ad5.CMV.eGFP injection group, IOP in Ad5.CMV.iCre-eGFP injection group was
1050 significantly decreased, it was also lower than the untouched group, but not statistically significant. (**B**)
1051 IOP changes in each group were analyzed and compared to their baseline normal IOP (before
1052 injection/time point 0 days), the graphical representation shows that IOP was significantly decreased in
1053 Ad5.CMV.iCre-eGFP injection group starting from 10 days after injection and sustained until 50 days
1054 post-injection. There were no significant changes in IOP levels in other control groups. (**C**) IOP
1055 percentage change (Delta IOP) compared to their baseline normal IOP in each group was calculated, and
1056 a graphical representation shows that IOP in Ad5.CMV.iCre-eGFP injection group was decreased as much
1057 as 40.38 % of baseline normal (before injection/time point 0 days) with an average decrease of 27.85 %.
1058 The IOP in other control groups showed less than 13 % changes of baseline normal IOP. (**D**) Histological
1059 examination of the TM using Hematoxylin and Eosin (H and E) staining showed no gross morphological
1060 alterations between four groups. Scale bar 100 micron. (**E**), (**F**) and (**G**) Immunolocalization of SCAP,
1061 SREBP1 and SREBP2 proteins in TM in four groups. SCAP showed decreased distribution in TM in
1062 Ad5.CMV.iCre-eGFP injection group compared to all other shame control groups. SREBP1 and SREBP2
1063 showed decreased distribution in the nuclear regions in TM in Ad5.CMV.iCre-eGFP injection group
1064 compared to other sham control groups. TM indicates trabecular meshwork and marked by white color
1065 arrow. Images were captured in z-stack in a confocal microscope, and stacks were orthogonally
1066 projected. Scale bar 50 micron. The top left corner in each image shows the magnification of the framed
1067 area showing the nuclear regions in TM and marked by green color arrow. Scale bar 10 micron. Values
1068 represent the mean ± SEM, where n = 9-10 (biological replicates). *$p < 0.05$ was considered statistically
1069 significant.

1070 **Figure 5: Inactivation of SREBPs inhibits lipogenesis in HTM cells.**

1071 (**A**) Fatostatin treatment significantly decreased SREBPs responsive genes mRNA expression involved in 1)
1072 cholesterol biosynthesis: low-density lipoprotein receptor (LDLR), hydroxymethylglutaryl-CoA synthase 1
1073 (HMGCS1), 3-hydroxy-3-methylglutaryl-CoA Reductase (HMGCR), SREBP2; 2) fatty acid biosynthesis:
1074 acetyl-CoA carboxylase (ACC), fatty acid synthase (FAS), SREBP1, peroxisome proliferator- activated
1075 receptor gamma (PPARG), acetyl-CoA synthetase ; 3) triglyceride and phospholipid biosynthesis:
1076 glycerol-3-phosphate acyltransferase (GPAT). 18S were used as internal controls for qPCR analysis. (**B**)
1077 Immunoblotting show that fatostatin significantly reduced FAS, HMGCR, and ACC protein expression
1078 compared to the control. GAPDH was used as loading control. (**C**), (**D**) and (**E**) show that fatostatin
1079 significantly reduced total lipid biosynthesis in HTM cells, including normalized phospholipid/cell,
1080 normalized cholesterol/cell, and normalized triglyceride/cell. Values represent the mean ± SEM, where n
1081 = 4 (biological replicates). *$p < 0.05$ was considered statistically significant.

1082 **Figure 6: SREBPs inactivation hampers actin polymerization machinery and disengages focal adhesions.**

1083 (**A**) and (**B**) Immunofluorescence (IF) shows the distribution of filamentous actin (F-actin) fiber, vinculin,
1084 and paxillin distribution in HTM cells under DMSO and fatostatin treatment. Fatostatin caused the
1085 reduced distribution of F-actin fiber stained by phalloidin (green/grayscale) in HTM cells (first and third
1086 column) compared to the control. Fatostatin treatment also caused less distribution of vinculin
1087 (red/grayscale) and paxillin (red/grayscale) at the edges of F-actin fiber, but more cytoplasmic
1088 distribution (indicated by white arrows) in HTM cells (first and fourth column) compared to the control.

1089 The nucleus was stained with DAPI in blue. Images were captured in z-stack in a confocal microscope,
1090 and stacks were orthogonally projected. Scale bar 20 micron. (**C**) Globular actin (G-actin) and F-actin
1091 were extracted from HTM cells treated with DMSO or fatostatin. Immunoblotting shows that fatostatin
1092 significantly decreased F-actin/G-actin ratio in HTM cells compared to the control. (**D**) Immunoblotting
1093 shows that fatostatin treatment significantly decreased p-MLC/MLC ratio in HTM cells. (**E**)
1094 Immunoblotting shows that fatostatin treatment significantly reduced Fascin-1 and LIMK1 protein
1095 expression, but no difference in vinculin expression compared to the control. GAPDH was used as a
1096 loading control. (**F**) Immunoblotting shows that there was no significant difference in total-cofilin (T-
1097 cofilin) protein expression levels in DMSO and fatostatin treated HTM cells. The phospho-cofilin (P-
1098 cofilin) and the ratio of P-cofilin/T-cofilin were significantly decreased in fatostatin treated HTM cells
1099 compared to the control. GAPDH was used as a loading control. (**G**) Immunoblotting shows that
1100 fatostatin significantly decreased phosphor-paxillin (P-paxillin) protein expression level, increased total-
1101 paxillin (T-paxillin) protein expression level, and significantly reduced the ratio of P-paxillin/T-paxillin
1102 compared to the control. GAPDH was used as a loading control. Values represent the mean ± SEM,
1103 where n = 4 (biological replicates). *$p < 0.05$ was considered statistically significant, and ns denotes non-
1104 significant.

1105 **Figure 7: SREBP activation is a critical regulator of ECM engagement to the matrix sites.**

1106 (**A**) Regulation of ECM mRNA expression under fatostatin treatment. Fatostatin treatment significantly
1107 decreased mRNA expression in fibronectin (FN), collagen 1α (COL1α), collagen 6α (COL6α), collagen 4α
1108 (COL4α), tenascin C (TNC), transforming growth factor β2 (TGFβ2), and sarcospan (SSPN) in HTM cells
1109 compared to DMSO treated control HTM cells. (**B**) Immunoblotting for whole cell lysate (CL) shows that
1110 fatostatin significantly decreased FN, and COL1A protein expression compared to DMSO treated control
1111 HTM cells. GAPDH was used as a loading control. (**C**) Immunoblotting for conditioned media (CM) shows
1112 that fatostatin significantly decreased FN and COL1A protein expression in HTM CM compared to DMSO
1113 treated control HTM CM. Ponceau S was used as a loading control. (**D**) and (**E**) Immunofluorescence (IF)
1114 shows the FN and COL1A expression and distribution in HTM cells after DMSO or fatostatin treatment.
1115 Fatostatin reduced FN (green staining) and COL1A (green staining) distribution compared to the control.
1116 The nucleus was stained with DAPI in blue. (**F**) and (**G**) Immunofluorescence (IF) shows that compared to
1117 fatostatin combined with AdMT treatment (first-row third column), there was increased FN and COL1A
1118 expression and distribution in HTM cells in fatostatin combined with Ad5-N-SREBP1a (second-row third
1119 column), Ad5-N-SREBP1c (third-row third column) and Ad5-N-SREBP2 (fourth-row third column)
1120 treatments. The nucleus was stained with DAPI in blue. Images were captured in z-stack in a confocal
1121 microscope, and stacks were orthogonally projected. Scale bar 20 micron. The lower magnification
1122 images of the cells can be visualized in the Supplementary Figure 7. Values represent the mean ± SEM,
1123 where n = 4 (biological replicates). *$p < 0.05$ was considered statistically significant.

1124

1125 **SUPPLEMENTARY MATERIAL LEGENDS:**

1126 **Supplementary Figure 1: Expression and distribution of SREBP isoforms and SCAP in TM**

1127 (**A**) Expression profile of SREBP isoforms and SCAP in primary human trabecular meshwork (HTM) cells
1128 by reverse-transcription polymerase chain reaction (RT-PCR) showing that SREBP1 transcript 2, SREBP2
1129 transcript 1, and SCAP were expressed in HTM. (**B**) Protein expression of proform SREBP1 (Pro-SREBP1)
1130 and SREBP2 (Pro-SREBP2), and nuclear form SREBP1 (N-SREBP1) and SREBP2 (N-SREBP2), and SCAP in
1131 primary HTM cells. GAPDH was used as the loading control. (**C**) Protein expression of Pro-SREBP1 and
1132 Pro-SREBP2, N-SREBP1 and N-SREBP2, and SCAP in the primary porcine trabecular meshwork (PTM) cells.
1133 GAPDH was used as the loading control. (**D**) Immunofluorescence (IF) shows the cytosolic distribution of
1134 SREBP1 (green staining), SREBP2 (green staining) and SCAP (green staining) in primary HTM cells. The
1135 nucleus was stained with DAPI in blue. Images were captured in z-stack in a confocal microscope, and
1136 stacks were orthogonally projected. Scale bar 20 microns. (**E**) Tissue distribution of SREBP1 (green
1137 staining) and SREBP2 (green staining) and SCAP (green staining) in the aqueous humor (AH) outflow
1138 pathway of a normal human eye specimen by IF. The nucleus was stained with DAPI in blue. Images
1139 were captured in z-stack in a confocal microscope, and stacks were orthogonally projected. Scale bar 50
1140 microns. (**F**) The negative control for SREBPs and SCAP distribution in AH outflow pathway (in the
1141 presence of secondary antibody alone) did not show any significant staining (green panel).

1142 **Supplementary Figure 2: Dose-dependent effects of fatostatin on SREBPs activation in PTM cells**

1143 (**A**) and (**B**) Dose-dependent treatment of fatostatin on PTM cells to test the optimal concentration of
1144 fatostatin on TM cells. Immunoblotting shows 20 µM fatostatin for 24 h treatment significantly
1145 decreased both N-SREBP1 and N-SREBP2 expression. GAPDH was used as a loading control. (**C**)
1146 Examination of the effects of 20 µM fatostatin on primary PTM cell viability. Cell viability assay in serum-
1147 starved PTM cells treated with 20 µM fatostatin for 24 h was performed using fluorometric live/dead
1148 staining of FDA-PI staining. The first row represents the control DMSO treatment, and the second row
1149 represents 20 µM fatostatin treatment of serum-starved PTM cells. The first, second, and the third
1150 columns are bright field image of PTM cells 24 h after treatment, FDA, and PI staining respectively. The
1151 green channel shows viable cells that take up FDA and emit green fluorescence, and the red channel
1152 shows dead cells, which take up PI and give out red florescence. The graphical representation denotes
1153 the mean percentage ratio of FDA/PI, including the viable cells (green bar) and the non-viable cells (red
1154 bar) in both control and 20 µM fatostatin treated cells. No significant cell death was observed after 20
1155 µM fatostatin for 24 h treatment. Values represent the mean ± SEM, where n = 4 (biological replicates).
1156 *$p < 0.05$ was considered statistically significant.

1157 **Supplementary Figure 3: 6 h mechanical stretch induces SREBPs activation**

1158 (**A**) and (**B**) Localization of SREBPs in HTM cells subjected to cyclic mechanical stretch was checked using
1159 immunofluorescence (IF). After 6 h of mechanical stress, HTM cells shows a strong nuclear localization of
1160 both SREBP1 and SREBP2 (second-row third column). Phalloidin was used to stain the distribution of
1161 filamentous actin (F-actin) fiber in the cells. After 6 h of mechanical stress, there was increased F-actin
1162 distribution inside the HTM cells (second-row fourth column). Quantification of immunofluorescence
1163 images using ImageJ-based fluorescence intensity measurements shows a significant increase in both
1164 nuclear SREBP1 and nuclear SREBP2's mean fluorescence intensity in 6 h stretched HTM cells (right
1165 panel).

1166 **Supplementary Figure 4: HTM cell changes after Ad5-N-SREBPs treatment**

1167 HTM cells were treated with either AdMT or Ad5-N-SREBPs for 24 h followed by 48 h serum starvation.
1168 (**A**) Compared to AdMT, Ad5-N-SREBP1a and Ad5-N-SREBP1c treatment on HTM cells significantly
1169 increased N-SREBP1 mRNA expression, and Ad5-N-SREBP2 significantly increased N-SREBP2 mRNA
1170 expression in HTM cells. 18S were used as internal controls for qPCR analysis. (**B**) Compared to AdMT,
1171 Ad5-N-SREBP1a and Ad5-N-SREBP1c significantly increased N-SREBP1 protein expression, and Ad5-N-
1172 SREBP2 significantly increased N-SREBP2 protein expression. The results were based on semi-
1173 quantitative immunoblotting with subsequent densitometric analysis. β-actin was used as a loading
1174 control. (**C**) Bright-field cell culture images were captured by Nikon TS100 Inverted Phase Contrast
1175 Microscope. After treatment, Ad5-N-SREBPs treated HTM cells displayed increased lamellipodia and
1176 filopodial extension formation (indicated by black arrows), compared to AdMT treatment. (**D**) and (**E**)
1177 Immunofluorescence (IF) shows the distribution of SREBP1, SREBP2, filamentous actin (F-actin) fibers,
1178 and paxillin in HTM cells under AdMT and Ad5-N-SREBPs treatments. (**D**) Ad5-N-SREBP1a (second-row
1179 third column), and Ad5-N-SREBP1c (third-row third column) induced strong staining of SREBP1 in the
1180 nucleus in HTM cells compared to AdMT (first-row third column). Similarly, (**E**) Ad5-N-SREBP2 (second-
1181 row third column) induced strong staining of SREBP2 in the nucleus in HTM cells compared to AdMT
1182 (first-row third column). Compared to AdMT (first-row fifth column), (**D**) Ad5-N-SREBP1a (second-row
1183 fifth column) and Ad5-N-SREBP1c (third-row fifth column), and (**E**) Ad5-N-SREBP2 (second-row fifth
1184 column) caused the increased distribution of F-actin fibers stained by phalloidin (purple/grayscale) in
1185 HTM cells and induced increased lamellipodia and filopodia formation (indicated by yellow arrows). (**D**)
1186 Ad5-N-SREBP1a (second-row fourth column), Ad5-N-SREBP1c (third-row fourth column), and (**E**) Ad5-N-
1187 SREBP2 (second-row fourth column) also induced more distribution of paxillin (green/grayscale) at the
1188 edges of F-actin fibers (indicated by white arrows) in HTM cells compared to the AdMT (first-row fourth
1189 column). The nucleus was stained with DAPI in blue. Images were captured in z-stack in a confocal
1190 microscope, and stacks were orthogonally projected. Scale bar 20 micron. Values represent the mean ±
1191 SEM, where n = 4 (biological replicates). $*p < 0.05$ was considered statistically significant.

1192 **Supplementary Figure 5: Molecular inactivation of SREBPs by knocking down SCAP in old and adult**
1193 ***SCAP$^{f/f}$* mice lowers IOP *in vivo***

1194 (**A**) In old *SCAP$^{f/f}$* mice, starting from 10 days after saline and viral injection, IOP was consistently and
1195 significantly decreased in Ad5.CMV.iCre-eGFP injection group compared to Ad5.CMV.eGFP injection
1196 group, and sustained until 50 days post-injection. Compared to the untouched and saline injection group,
1197 IOP was also lower in Ad5.CMV.iCre-eGFP injection group, but not consistently statistically significant. (**B**)
1198 In old *SCAP$^{f/f}$* mice, IOP changes in each group were analyzed and compared to their baseline normal IOP
1199 (before injection/time point 0 days), the graphical representation shows that IOP was significantly
1200 decreased in Ad5.CMV.iCre-eGFP injection group starting from 10 days after injection and sustained
1201 until 50 days post-injection. There were no significant changes in IOP levels in other control groups. (**C**)
1202 In old *SCAP$^{f/f}$* mice, IOP percentage change (Delta IOP) compared to their baseline normal IOP in each
1203 group was calculated, and graphical representation shows that IOP in Ad5.CMV.iCre-eGFP injection
1204 group was decreased as much as 42.72 % of baseline normal (before injection/time point 0 days) with an
1205 average decrease of 27.61 %. The IOP in other control groups showed less than 17 % changes of baseline
1206 normal IOP. (**D**) In adult *SCAP$^{f/f}$* mice, start from 10 days after saline and viral injection, IOP was
1207 consistently and significantly decreased in Ad5.CMV.iCre-eGFP injection group compared to
1208 Ad5.CMV.eGFP injection group, and sustained until 50 days post-injection. Compared to the untouched,

1209 saline injection group, IOP was also lower in Ad5.CMV.iCre-eGFP injection group, but not consistently
1210 statistically significant. (**E**) In adult *SCAP*$^{f/f}$ mice, IOP was significantly decreased in Ad5.CMV.iCre-eGFP
1211 injection group starting from 10 days after injection and sustained until 50 days post-injection. There
1212 were no significant changes in IOP levels in other control groups. (**F**) In adult *SCAP*$^{f/f}$ mice, IOP in
1213 Ad5.CMV.iCre-eGFP injection group decreased as much as 43.14 % of baseline normal (before
1214 injection/time point 0 days) with an average decrease of 28.10 %. The IOP in other control groups
1215 showed less than 17 % changes of baseline normal IOP. Values represent the mean ± SEM, where n = 4-5
1216 (biological replicates). *$p < 0.05$ was considered statistically significant.

1217 **Supplementary Figure 6: Averaged top25 cellular lipid changes in lipidomics analysis**

1218 (**A**) Averaged top25 lipid changes heatmap of the total cellular phosphatidylcholine (PC) in control and
1219 fatostatin treated HTM cells. (**B**) Averaged top25 lipid changes heatmap of the total cellular
1220 phosphatidylethanolamine (PE) in control and fatostatin treated HTM cells. (**C**) Averaged top25 lipid
1221 changes heatmap of the total cellular cholesteryl ester (CE) in control and fatostatin treated HTM cells.
1222 (**D**) Averaged top25 lipid changes heatmap of the total cellular diacylglycerol (DG) in control and
1223 fatostatin treated HTM cells. (**E**) Averaged top25 lipid changes heatmap of the total fatty acid (FA) in
1224 control and fatostatin treated HTM cells. (**F**) Averaged top25 lipid changes heatmap of the total
1225 triacylglycerol (TG) in control and fatostatin treated HTM cells. (**G**) Averaged top25 lipid changes
1226 heatmap of the total cellular phosphatidylserine (PS) in control and fatostatin treated HTM cells. (**H**)
1227 Averaged top25 lipid changes heatmap of the total cellular ceramide (Cer) in control and fatostatin
1228 treated HTM cells. (**I**) Averaged top25 lipid changes heatmap of the total cellular sphingomyelin (SM) in
1229 control and fatostatin treated HTM cells. All heatmaps are presented by control and fatostatin treated
1230 HTM cells, both are averaged from n = 4 biological replicates. FATO indicates fatostatin treatment.

1231 **Supplementary Figure 7: ECM changes due to response to SREBPs activation**

1232 Immunofluorescence (IF) shows the FN and COL1A expression and distribution in HTM cells after
1233 fatostatin combined with AdMT or Ad5-N-SREBPs treatments. Increased FN and COL1A distribution in
1234 HTM cells were observed in fatostatin combined with Ad5-N-SREBP1a (second-row third column and
1235 sixth column), Ad5-N-SREBP1c (third-row third column and sixth column) and Ad5-N-SREBP2 (fourth-row
1236 third column and sixth column) treatments, compared to fatostatin combined with AdMT treatment
1237 (first-row third column and sixth column). The nucleus was stained with DAPI in blue. Images were
1238 captured in z-stack in a confocal microscope, and stacks were orthogonally projected. Scale bar 20
1239 micron. White box in the images indicate the chosen cells and magnifications of these cells are included
1240 in Figure 7F and 7G.

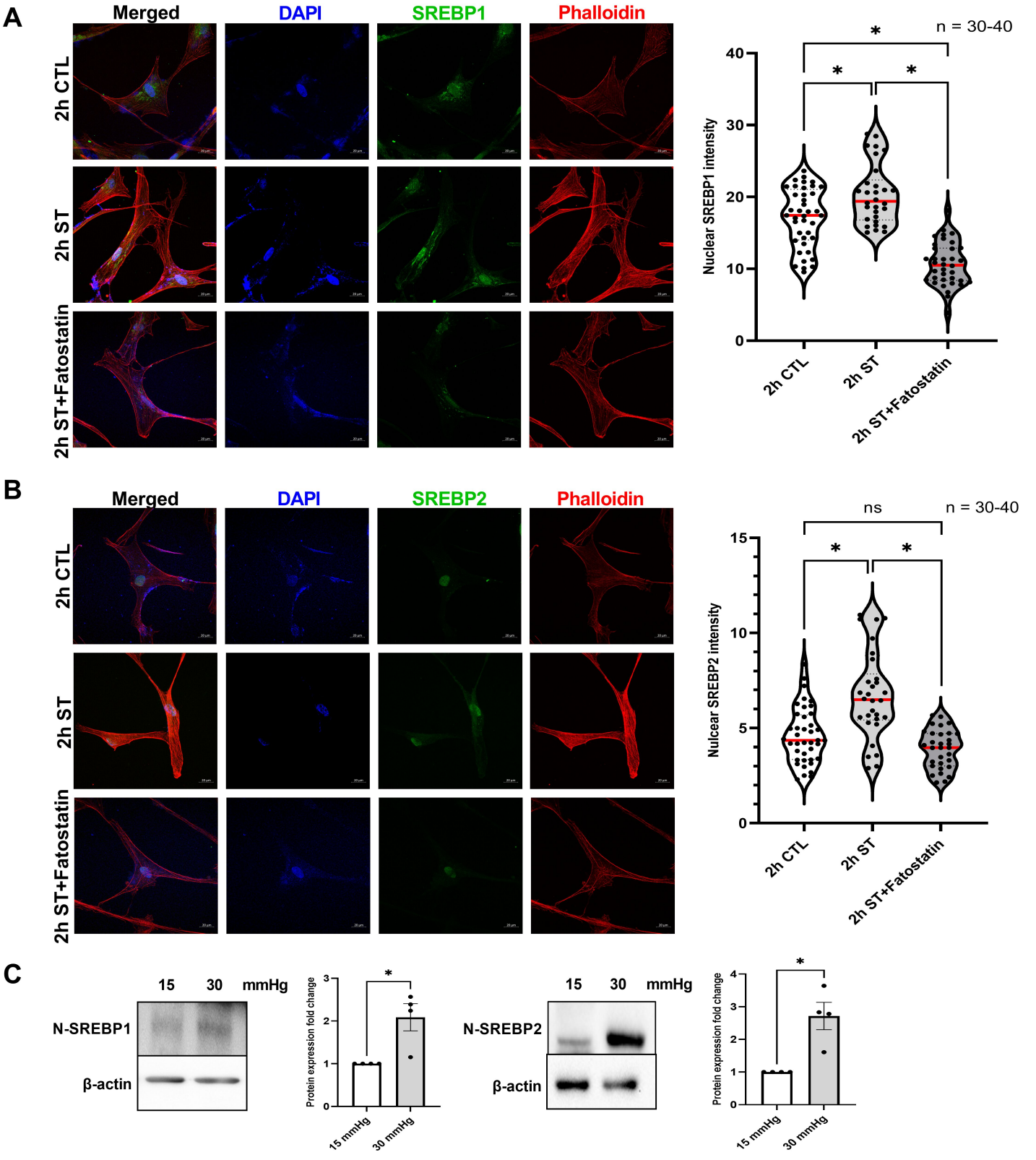
A
Merged
DAPI
SREBP1
Phalloidin
2h CTL
2h ST
2h ST+Fatostatin
n = 30-40
Nuclear SREBP1 intensity
B
Merged
DAPI
SREBP2
Phalloidin
2h CTL
2h ST
2h ST+Fatostatin
ns
n = 30-40
Nulcear SREBP2 intensity
C
15
30
mmHg
N-SREBP1
β-actin
Protein expression fold change
15 mmHg
30 mmHg
N-SREBP2
β-actin

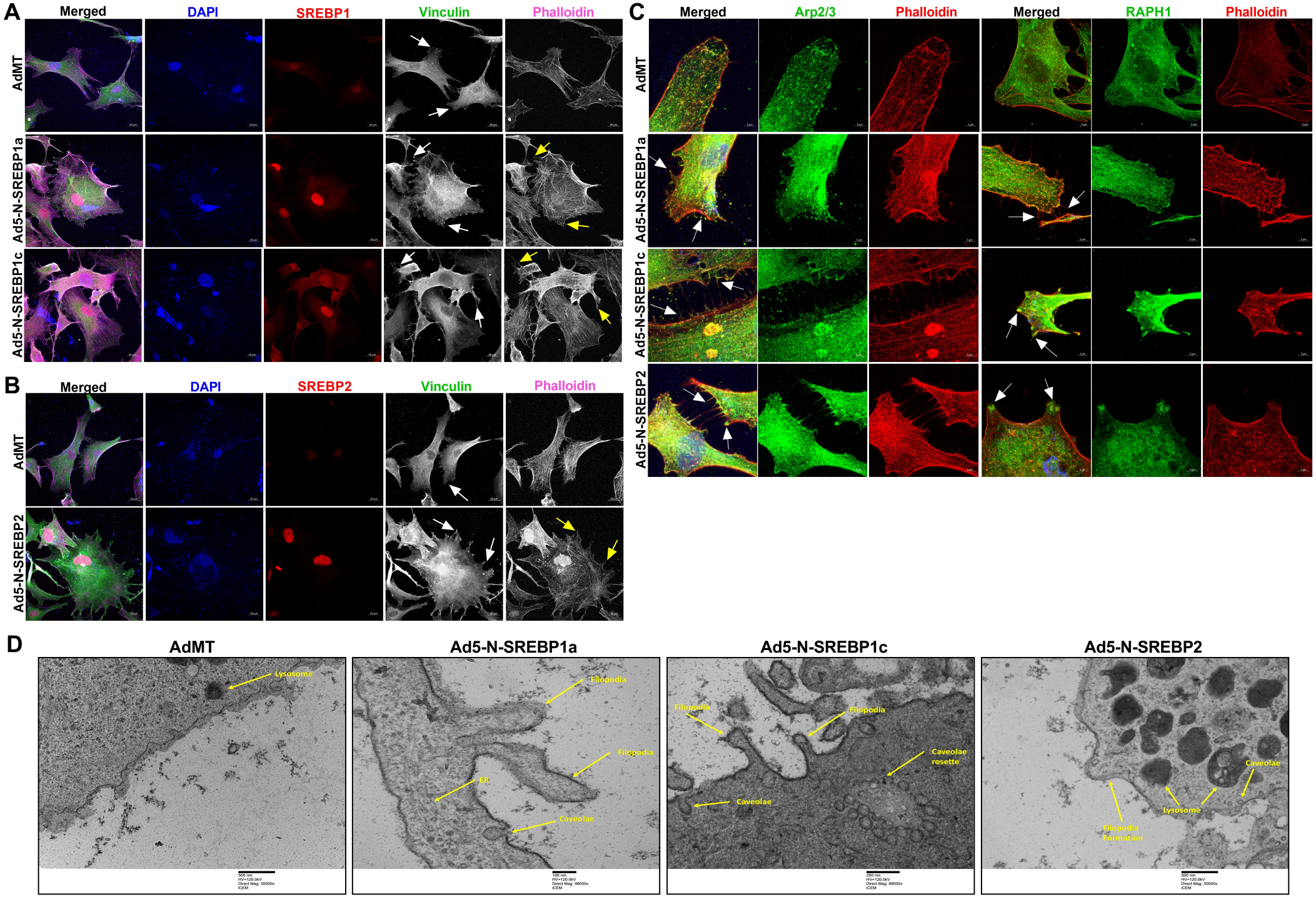
A
Merged
DAPI
SREBP1
Vinculin
Phalloidin
AdMT
Ad5-N-SREBP1a
Ad5-N-SREBP1c
B
Merged
DAPI
SREBP2
Vinculin
Phalloidin
AdMT
Ad5-N-SREBP2
C
Merged
Arp2/3
Phalloidin
Merged
RAPH1
Phalloidin
AdMT
Ad5-N-SREBP1a
Ad5-N-SREBP1c
Ad5-N-SREBP2
D
AdMT
Lysosome
Ad5-N-SREBP1a
Filopodia
Filopodia
ER
Caveolae
Ad5-N-SREBP1c
Filopodia
Filopodia
Caveolae rosette
Caveolae
Ad5-N-SREBP2
Caveolae
Lysosome
Filopodia formation

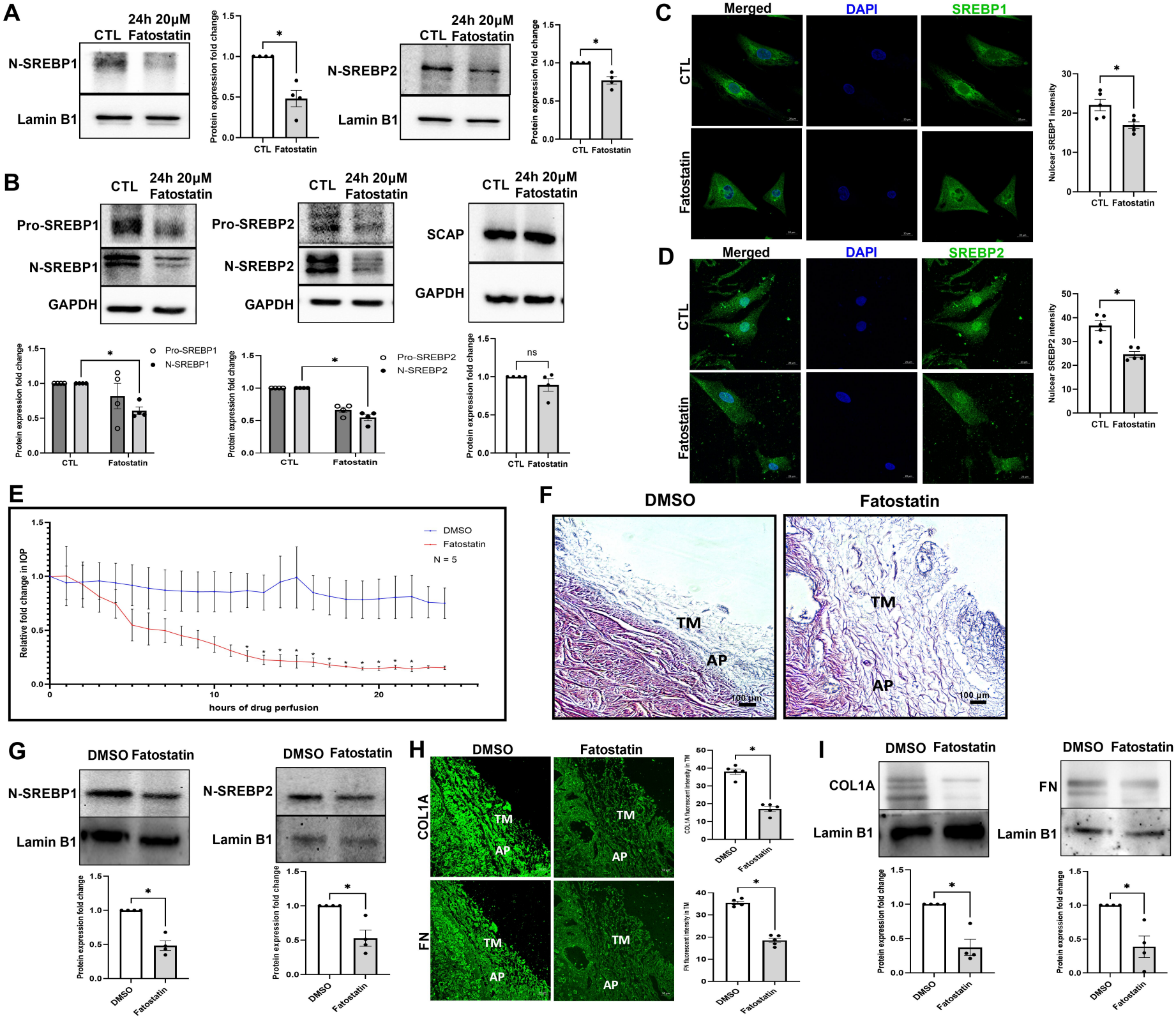
A
24h 20μM
CTL Fatostatin
N-SREBP1
Lamin B1
Protein expression fold change
CTL Fatostatin
N-SREBP2
Lamin B1
B
CTL 24h 20μM Fatostatin
Pro-SREBP1
N-SREBP1
GAPDH
Pro-SREBP2
N-SREBP2
SCAP
Pro-SREBP1
N-SREBP1
Pro-SREBP2
N-SREBP2
ns
C
Merged
DAPI
SREBP1
CTL
Fatostatin
Nulcear SREBP1 intensity
D
SREBP2
Nulcear SREBP2 intensity
E
DMSO
Fatostatin
N = 5
Relative fold change in IOP
hours of drug perfusion
F
DMSO
Fatostatin
TM
AP
100 μm
G
N-SREBP1
N-SREBP2
H
COL1A
FN
COL1A fluorescent intensity in TM
FN fluorescent intensity in TM
I
COL1A
FN

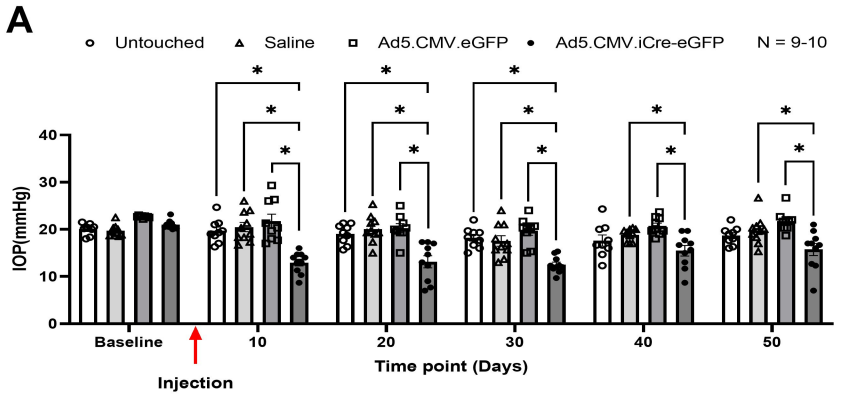
A
Untouched
Saline
Ad5.CMV.eGFP
Ad5.CMV.iCre-eGFP
N = 9-10
IOP(mmHg)
Baseline
Injection
Time point (Days)

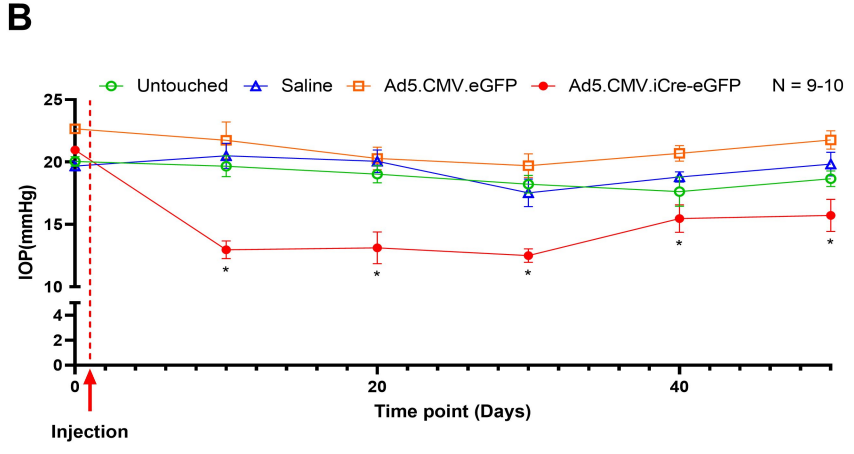
B
Untouched
Saline
Ad5.CMV.eGFP
Ad5.CMV.iCre-eGFP
N = 9-10
IOP(mmHg)
Injection
Time point (Days)

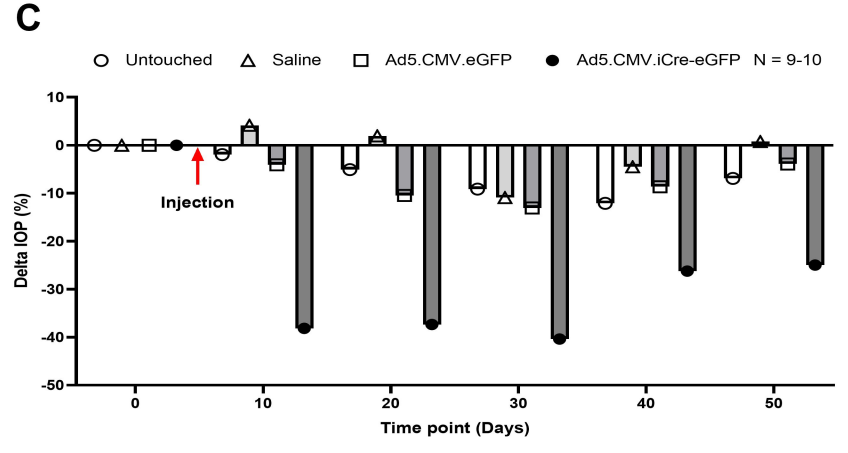
C
Untouched
Saline
Ad5.CMV.eGFP
Ad5.CMV.iCre-eGFP
N = 9-10
Delta IOP (%)
Injection
Time point (Days)

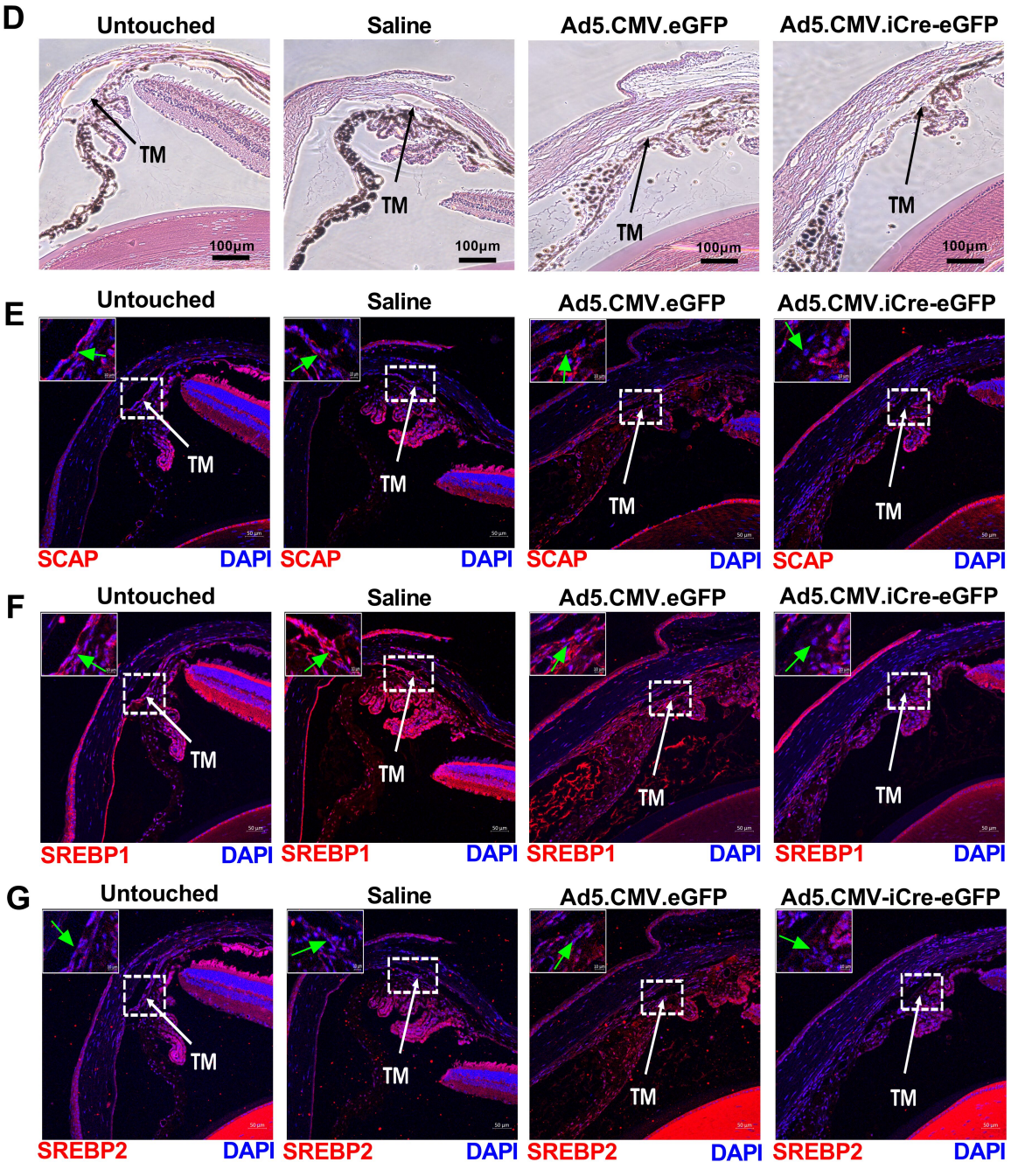
D
Untouched
Saline
Ad5.CMV.eGFP
Ad5.CMV.iCre-eGFP
TM
100μm
E
SCAP
DAPI
F
SREBP1
G
SREBP2
Ad5.CMV-iCre-eGFP

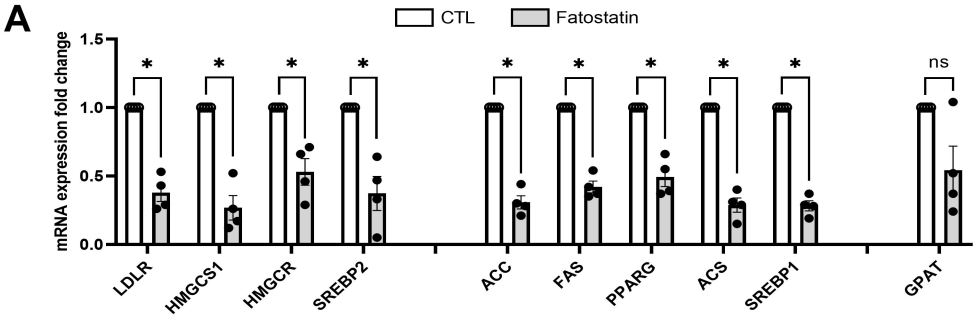
A
CTL
Fatostatin
mRNA expression fold change
1.5
1.0
0.5
0.0
*
ns
LDLR
HMGCS1
HMGCR
SREBP2
ACC
FAS
PPARG
ACS
SREBP1
GPAT

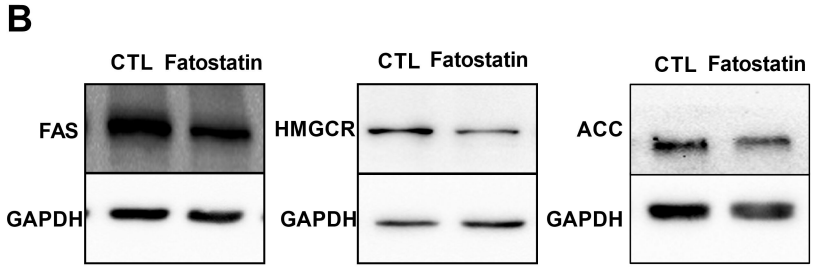
B
CTL Fatostatin
FAS
GAPDH
HMGCR
ACC

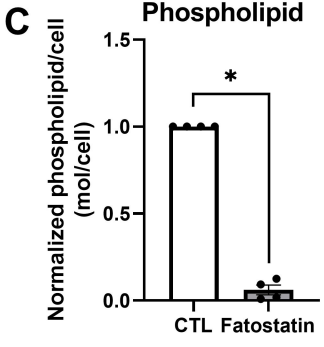
C
Phospholipid
Normalized phospholipid/cell (mol/cell)
1.5
1.0
0.5
0.0
*
CTL Fatostatin

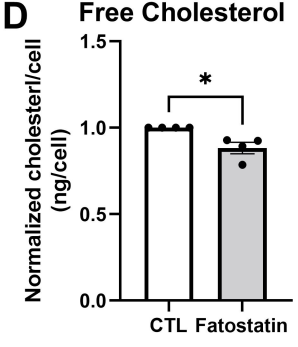
D
Free Cholesterol
Normalized cholesterl/cell (ng/cell)
1.5
1.0
0.5
0.0
*
CTL Fatostatin

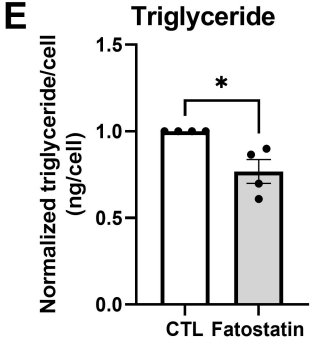
E
Triglyceride
Normalized triglyceride/cell (ng/cell)
1.5
1.0
0.5
0.0
*
CTL Fatostatin

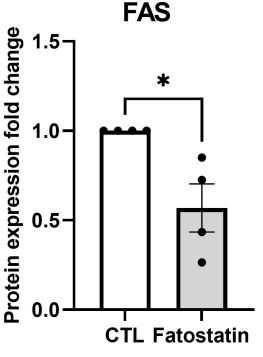
FAS
Protein expression fold change
1.5
1.0
0.5
0.0
*
CTL Fatostatin

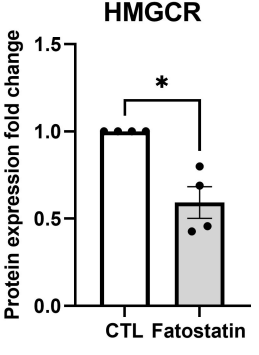
HMGCR
Protein expression fold change
1.5
1.0
0.5
0.0
*
CTL Fatostatin

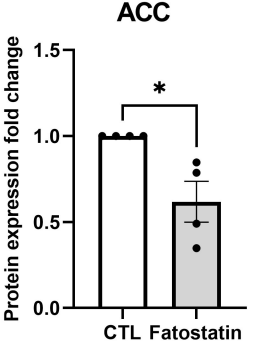
ACC
Protein expression fold change
1.5
1.0
0.5
0.0
*
CTL Fatostatin

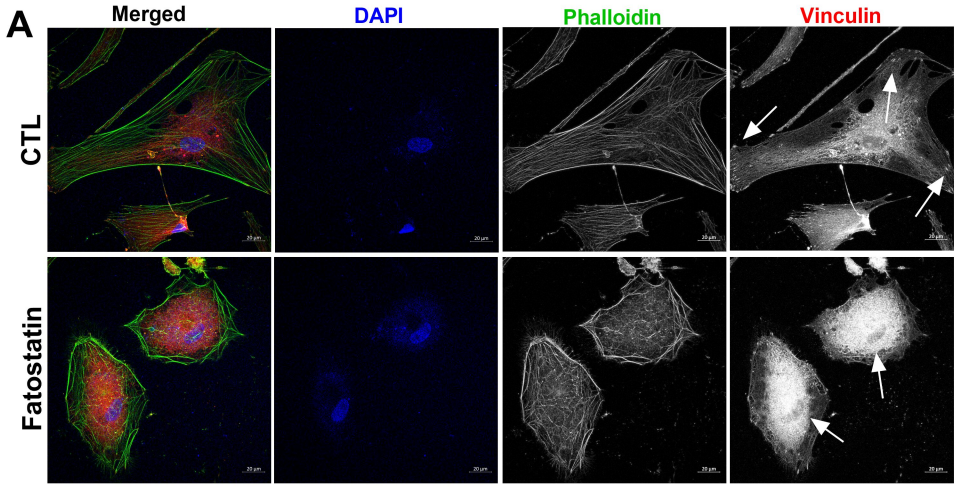
A
Merged
DAPI
Phalloidin
Vinculin
CTL
Fatostatin

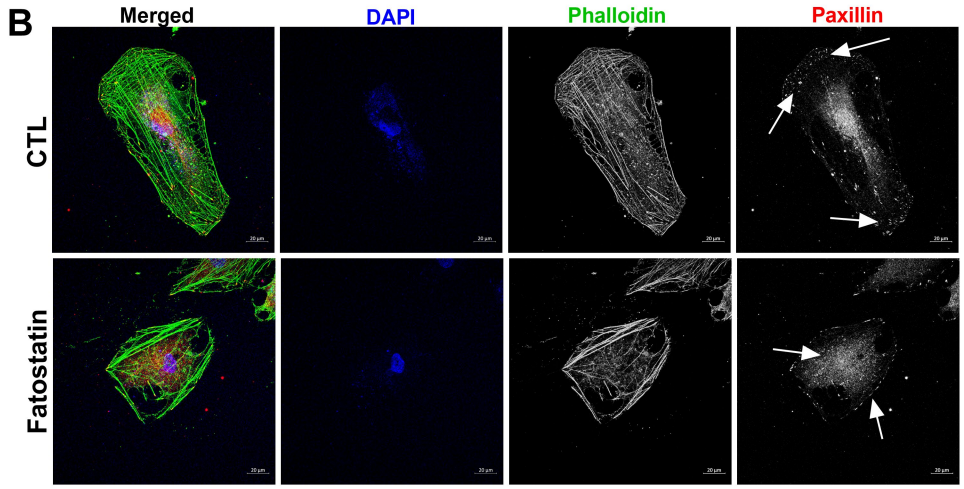
B
Merged
DAPI
Phalloidin
Paxillin
CTL
Fatostatin

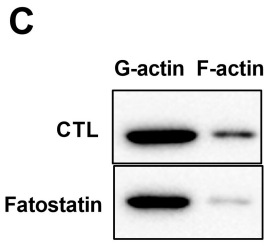
C
G-actin
F-actin
CTL
Fatostatin

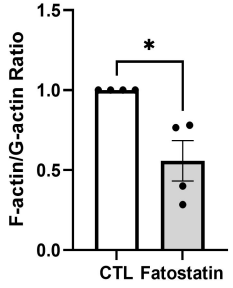
F-actin/G-actin Ratio
1.5
1.0
0.5
0.0
*
CTL
Fatostatin

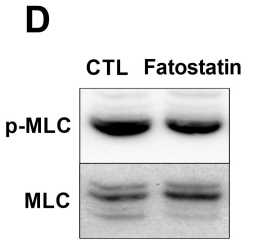
D
CTL
Fatostatin
p-MLC
MLC

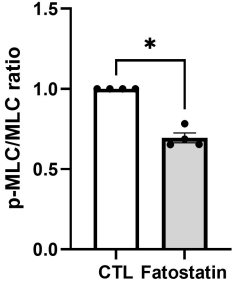
p-MLC/MLC ratio
1.5
1.0
0.5
0.0
*
CTL
Fatostatin

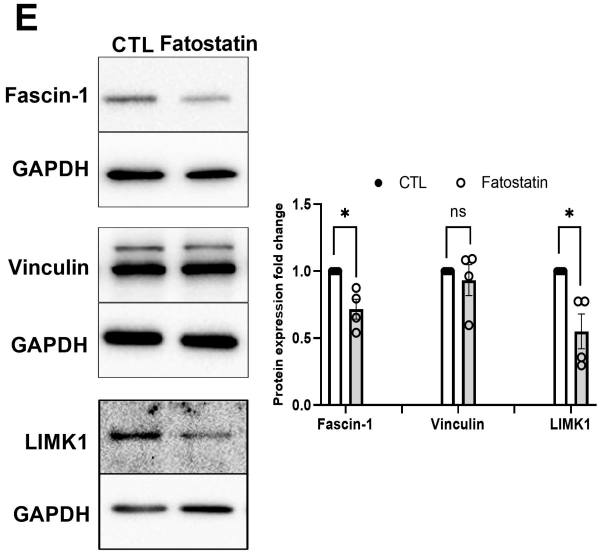
E
CTL
Fatostatin
Fascin-1
GAPDH
Vinculin
GAPDH
LIMK1
GAPDH
CTL
Fatostatin
Protein expression fold change
1.5
1.0
0.5
0.0
*
ns
*
Fascin-1
Vinculin
LIMK1

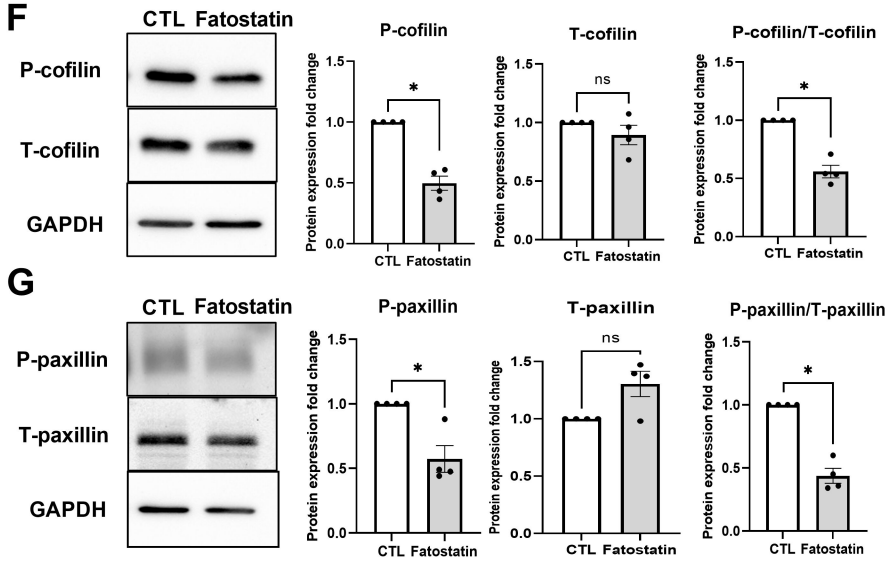
F
CTL
Fatostatin
P-cofilin
T-cofilin
GAPDH
P-cofilin
T-cofilin
P-cofilin/T-cofilin
Protein expression fold change
1.5
1.0
0.5
0.0
*
ns
*
CTL
Fatostatin
G
CTL
Fatostatin
P-paxillin
T-paxillin
GAPDH
P-paxillin
T-paxillin
P-paxillin/T-paxillin
Protein expression fold change
1.5
1.0
0.5
0.0
*
ns
*
CTL
Fatostatin

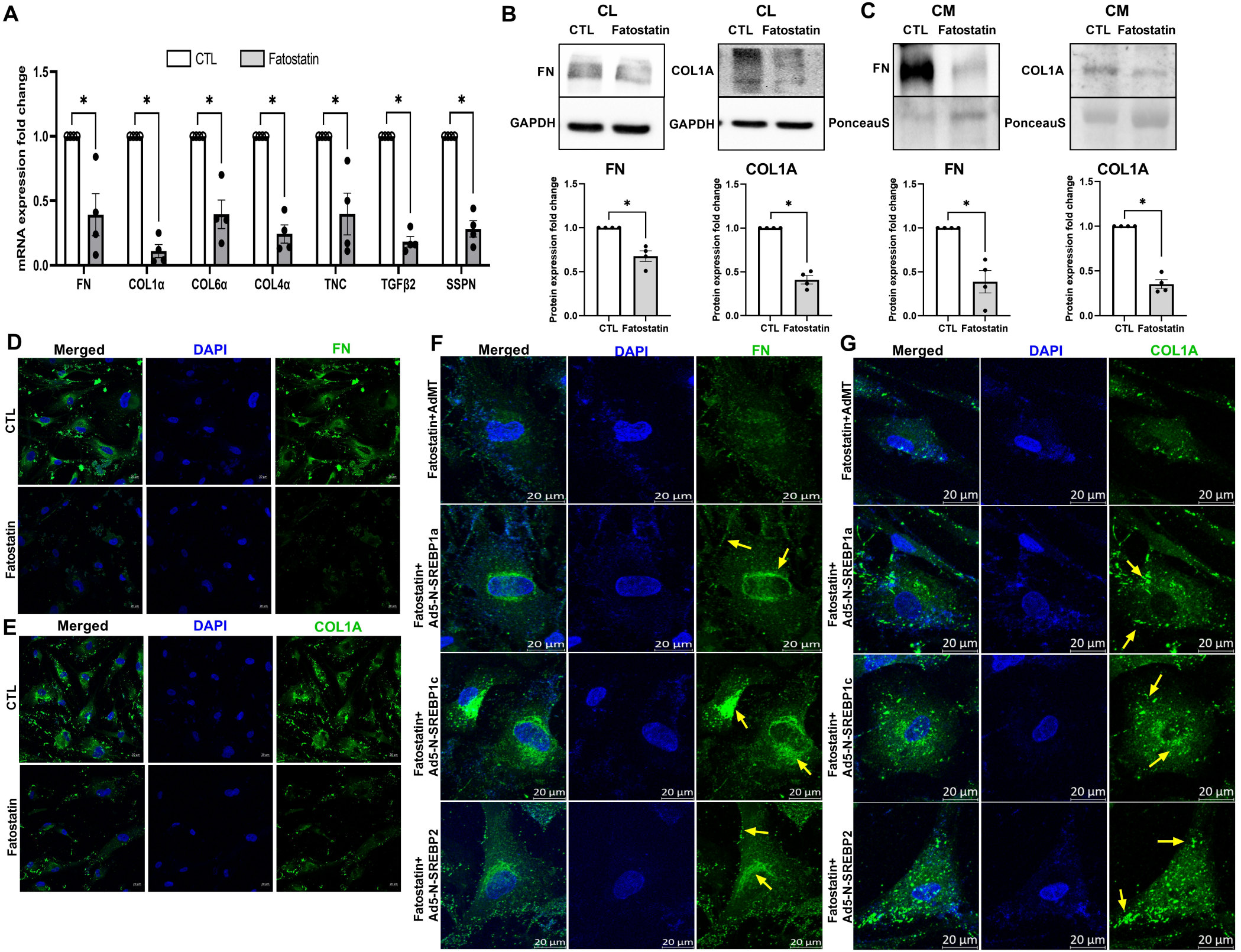
A
CTL
Fatostatin
mRNA expression fold change
1.5
1.0
0.5
0.0
FN
COL1α
COL6α
COL4α
TNC
TGFβ2
SSPN
B
CL
CTL Fatostatin
FN
GAPDH
COL1A
PonceauS
C
CM
Protein expression fold change
D
Merged
DAPI
FN
E
COL1A
F
Fatostatin+AdMT
Fatostatin+ Ad5-N-SREBP1a
Fatostatin+ Ad5-N-SREBP1c
Fatostatin+ Ad5-N-SREBP2
20 μm
G

1 **TABLES:**

2 **TABLE 1: Antibodies and Reagents:**

Reagents and antibodies	Catalog number	Company
Vinculin	V9131	R&D system
β-actin	A1798	R&D system
Collagen 1α (COL1A)	ab34710	R&D system
RAPH1	PA5-110270	Invitrogen/ThermoFisher
Arp2/3	07-227-I	Sigma-Aldrich
LIMK1	sc515585	Santa Cruz Biotechnology
SREBP1	sc13551	Santa Cruz Biotechnology
SREBP2	sc13552	Santa Cruz Biotechnology
Paxillin	sc365379	Santa Cruz Biotechnology
GAPDH	sc32233	Santa Cruz Biotechnology
FAS	sc-48357	Santa Cruz Biotechnology
Fascin 1	sc46675	Santa Cruz Biotechnology
SREBP1	NB100-2215	NOVUS Biologicals
SREBP2	NBP1-54446	NOVUS Biologicals
SREBP2	LS-B1609-BCD1-1	Life Span Bioscience
SCAP	12266-1-AP	Proteintech
SCAP	MABS2288	Sigma-Aldrich
Collagen 1α (COL1A)	ABT257	Sigma-Aldrich
HMGCR	PA5-37367	Invitrogen/ThermoFisher
Lamin B1	PA5-19468	Invitrogen/ThermoFisher
Total-paxillin (T-paxillin)	2542S	Cell Signaling Technology
Phospho-paxillin (P-paxillin)	69363S	Cell Signaling Technology
Total-cofilin (T-cofilin)	5175S	Cell Signaling Technology
Phospho-cofilin (P-cofilin)	3311S	Cell Signaling Technology
Phospho-myosin light chain (p-MLC)	3671	Cell Signaling Technology
Myosin light chain (MLC)	3672	Cell Signaling Technology
ACC	3662S	Cell Signaling Technology
Fibronectin		Gift from Dr. Harold Erickson, Duke University
Donkey-anti-goat IgG	705-035-003	Jackson ImmunoResearch
Donkey-anti-mouse IgG	715-035-150	Jackson ImmunoResearch
Donkey-anti-rabbit IgG	715-035-144	Jackson ImmunoResearch
Goat-anti-Mouse IgG Alexa Fluro Plus 488	A32723	ThermoFisher
Goat-anti-Mouse IgG Alexa Fluor Plus 594	A32742	ThermoFisher
Goat-anti-Rabbit IgG Alexa Fluor Plus 488	A32731	ThermoFisher
Goat-anti-Rabbit IgG Alexa Fluor Plus 594		ThermoFisher
Phalloidin (Alexa Fluor Plus 488 PHA)	A12379	Invitrogen/ThermoFisher
Phalloidin (Alexa Fluor Plus 647 PHA)	A22287	Invitrogen/ThermoFisher
DAPI	UH2820551	Sigma-Aldrich
Fluoromount-G	E139999	Invitrogen/ThermoFisher
Fatostatin	341329	Sigma-Aldrich

3

4 **TABLE 2: Oligonucleotides used for qPCR:**

SREBP1 Transcript 1 (F1V1)	Forward	CTGACCGACATCGAAGGTGA
	Reverse	AAGTGCAATCCATGGCTCCG
SREBP1 Transcript 2 (F1V2)	Forward	GCTGACCGACATCGAAGACA
	Reverse	CAGGAGGTGGAGACAAGCTG
SREBP1 Transcript 3 (F1V3)	Forward	AACGGCTTCAAAAATCCGCC
	Reverse	CCAGCATAGGGTGGGTCAAA
SREBP2 Transcript 1 (F2V1)	Forward	GGTTGTCGGGTGTCATGGG
	Reverse	TTGCAGCATCTCGTCGATGT
SCAP Transcript 1	Forward	CTGGAGAAGCTGGACTGAGC
	Reverse	CCCAAAGTGCCTGACAGATG
Total-SREBP1	Forward	CAACACAGCAACCAGAAACTC
	Reverse	CTCCACCTCAGTCTTCACG
Total-SREBP2	Forward	ATTCAGCACCACTCCGCAG
	Reverse	GCCCCATCATTACAGGCATTG
LDLR	Forward	TTCACTCCATCTCAAGCATCG
	Reverse	ACTGAAAATGGCTTCGTTGATG
HMGCS1	Forward	TTCCCTTGCATCTGTTCTAGC
	Reverse	TTTTATCAAGAGCAGACCCCG
HMGCR	Forward	ACAGATACTTGGGAATGCAGAG
	Reverse	CTGTCGGCGAATAGATACACC
ACC	Forward	ACAGTGGAGCAAGAATCGG
	Reverse	AATGGACAGAGTTGAGAGCAC
FASN	Forward	AAGCTCTTTCACTTCGGAGG
	Reverse	GGGCATTAACACTTTTGGACG
PPARG	Forward	ATCAAAGTGGAGCCTGCATC
	Reverse	CGACATTCAATTGCCATGAG
ACS	Forward	GGGAAGAGTTGGAAGGTGAAG
	Reverse	GCAGCCATCTCCTGTAACATAG
GPAT	Forward	GTGGAGTGTAGCAAGAGGTG
	Reverse	CAGGGAAAGTAGAGCAGACAC
FN	Forward	GGTGACACTTATGAGCGTCCTAAA
	Reverse	AACATGTAACCACCAGTCTCATGTG
COL1α	Forward	GAGAGCATGACCGATGGATT
	Reverse	CCTTCTTGAGGTTGCCAGTC
COL4α	Forward	TGTGGATCGGCTACTCTTTTG
	Reverse	TAGTAATTGCAGGTCCCACG
COL6α	Forward	TCAAGTCCTTCACCAAGCG
	Reverse	ATCTCCACCTCGTCACTGTA
TNC	Forward	CACTACACAGCCAAGATCCAG
	Reverse	TCGTGTCTCCATTCAGCATTG
TGFβ2	Forward	TTGACGTCTCAGCAATGGAG
	Reverse	TTCGCCTTCTGCTCTTGTTT
SSPN	Forward	AGGTTGACGAACGGACATG
	Reverse	TGTGAGCTGCGAATAGTGG

18S	Forward	CTACCACATCCAAGGAAGCA
	Reverse	TTTTTCGTCACTACCTCCCCG

7 **Table 3: Significantly decreased lipids in fatostatin treated HTM cells using lipidomics analysis**

8 Lipids significantly decreased in fatostatin treated compared to DMSO treated HTM cells. Columns (left
9 to right) show the lipid name, calculated *p*-value, and -log10(*p*) based on lipidomics analysis, where n = 4
10 (biological replicates), $p < 0.05$ was considered statistically significant.

Significantly Decreased Lipids		
Lipid names	**p.value**	**-LOG10(p)**
FA(26:2)	0.028469	1.5456
FA(31:0)	0.042276	1.3739
FA(8:5)	0.044452	1.3521
FA(40:6)	0.045725	1.3398
FA(28:3)	0.048249	1.3165
PC(34:3),PC(P-35:2)	0.049402	1.3063
PC(32:4)	0.035932	1.4445
PC(39:4),PC(O-40:4),PC(P-40:3)	0.035369	1.4514
PC(36:3),PC(P-37:2)	0.033334	1.4771
PC(39:5),PC(O-40:5),PC(P-40:4)	0.02939	1.5318
PC(40:4)	0.028955	1.5383
PC(36:6)	0.025581	1.5921
PC(32:3),PC(P-33:2)	0.024358	1.6134
PC(37:6),PC(O-38:6),PC(P-38:5)	0.023377	1.6312
PC(30:3)	0.023107	1.6363
PC(40:2)	0.021659	1.6644
LPC(18:0),PC(O-18:0),LPC(O-19:0)	0.020997	1.6778
PC(40:6)	0.020007	1.6988
PC(40:5)	0.015675	1.8048
PC(35:6),PC(P-36:5)	0.015663	1.8051
PC(O-38:9),PC(36:2),PC(O-37:2),PC(P-37:1)	0.012034	1.9196
PC(39:6),PC(O-40:6),PC(P-40:5)	0.008298	2.081
PC(42:7),PC(41:0),PC(O-42:0)	0.005097	2.2927
PC(35:5),PC(O-36:5),PC(P-36:4)	0.004128	2.3842
PC(42:8),PC(41:1),PC(O-42:1),PC(P-42:0)	0.002498	2.6023
PC(42:11),PC(41:4),PC(O-42:4)	0.000459	3.3382
PE(36:7),PE(35:0),PE(O-36:0)	0.003916	2.4072
PE(39:8),PE(O-40:8),PE(P-40:7),PE(38:1),PE(O-39:1),PE(P-39:0)	0.0059	2.2292
PE(31:3)	0.006313	2.1997
LPE(24:6)	0.007378	2.1321
PE(41:5),PE(P-42:4)	0.018917	1.7231
LPE(20:0)	0.022466	1.6485
PE(30:0),PE(O-31:0)	0.026313	1.5798
PE(41:7),PE(P-42:6),PE(40:0),PE(O-41:0)	0.039907	1.399
PE(42:4)	0.048557	1.3137

PS(P-34:0)	0.023249	1.6336
Cer(d20:0/26:0)	0.008979	2.0468
SM(d16:1/22:1)	0.006082	2.216
SM(d16:0/24:0)	0.016019	1.7954
SM(d16:1/20:1)	0.016222	1.7899
SM(d16:1/24:1)	0.045543	1.3416
[TG(64:6)]_FA18:0	0.019064	1.7198
[TG(41:0)]_FA18:0	0.019322	1.7139
[TG(64:15),TG(63:8),TG(62:1)]_FA18:0	0.041375	1.3833
[TG(54:11),TG(53:4)]_FA18:0	0.049515	1.3053

13 **Table 4: Significantly increased lipids in fatostatin treated HTM cells using lipidomics analysis**

14 Lipids significantly increased in fatostatin treated HTM cells, compared to DMSO treated control HTM
15 cells. Columns (left to right) show the lipid name, calculated *p*-value, and -log10(*p*) based on lipidomics
16 analysis, where n = 4 (biological replicates), $p < 0.05$ was considered statistically significant

Significantly Increased Lipids		
Lipid names	**p.value**	**-LOG10(p)**
FA(46:0)	0.002262	2.6455
FA(9:0)	0.028193	1.5499
PC(48:2)	0.048723	1.3123
LPS(22:2)	0.00053	3.2756
LPS(O-18:0)	0.001578	2.802
PS(P-36:4)	0.007234	2.1406
PS(31:3)	0.00733	2.1349
PS(30:3)	0.012664	1.8974
LPS(17:2)	0.014756	1.831
PS(P-37:0)	0.017008	1.7694
PS(P-30:1)	0.021447	1.6686
PS(42:3)	0.022778	1.6425
PS(P-34:1)	0.032583	1.487
PS(P-34:2)	0.039833	1.3998
LPS(P-16:0)	0.044804	1.3487
PS(24:0)	0.049925	1.3017
Cer(d18:1/25:0)	0.02538	1.5955
[TG(44:3)]_FA18:0	0.012642	1.8982
[TG(47:2)]_FA18:0	0.046668	1.331

17

18

19 **Table 5: The most relevant pathways involved in fatostatin treated HTM cells using lipidomics**
20 **pathway analysis**

21 The table shows the detailed results for pathways are relevant to fatostatin treatment. Columns (left to
22 right) denote the pathway names, the total number of compounds in the pathway (Total Compound),
23 the matched number from the lipidomics data (Hits), the original p value calculated from the
24 enrichment analysis (Raw p), the p value adjusted using False Discovery Rate (FDR), and the pathway
25 impact value calculated from pathway topology analysis (Impact).

Pathways	Total Compound	Hits	Raw p	FDR	Impact
Glycosylphosphatidylinositol (GPI)-anchor biosynthesis	14	1	0.17694	0.65345	0.00399
Glycerophospholipid metabolism	36	4	0.40972	0.65345	0.26332
Arachidonic acid metabolism	36	1	0.46277	0.65345	0
Linoleic acid metabolism	5	1	0.46277	0.65345	0
alpha-Linolenic acid metabolism	13	1	0.46277	0.65345	0
Biosynthesis of unsaturated fatty acids	36	1	0.49008	0.65345	0
Sphingolipid metabolism	21	2	0.83211	0.88546	0.26978
Steroid biosynthesis	42	1	0.88546	0.88546	0

26

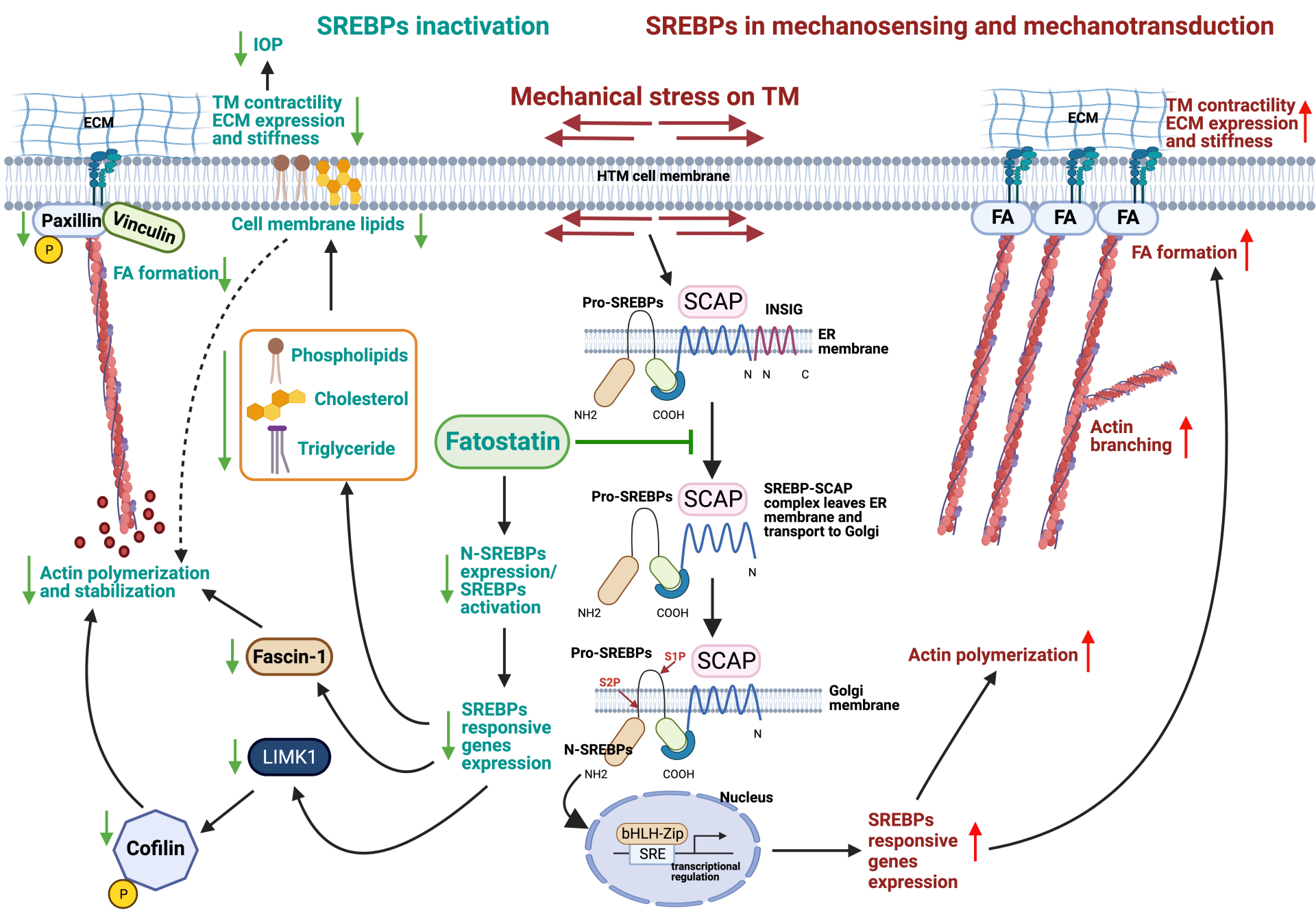
SREBPs inactivation
SREBPs in mechanosensing and mechanotransduction
IOP
TM contractility
ECM expression
and stiffness
Mechanical stress on TM
ECM
HTM cell membrane
TM contractility
ECM expression
and stiffness
Paxillin
Vinculin
P
Cell membrane lipids
FA
FA
FA
FA formation
FA formation
Phospholipids
Cholesterol
Triglyceride
Pro-SREBPs
SCAP
INSIG
ER
membrane
N N C
NH2
COOH
Fatostatin
Actin
branching
Pro-SREBPs
SCAP
SREBP-SCAP
complex leaves ER
membrane and
transport to Golgi
N
NH2
COOH
Actin polymerization
and stabilization
N-SREBPs
expression/
SREBPs
activation
Fascin-1
Pro-SREBPs
S1P
SCAP
S2P
Golgi
membrane
N
N-SREBPs
NH2
COOH
Actin polymerization
SREBPs
responsive
genes
expression
LIMK1
Nucleus
bHLH-Zip
SRE
transcriptional
regulation
SREBPs
responsive
genes
expression
Cofilin
P

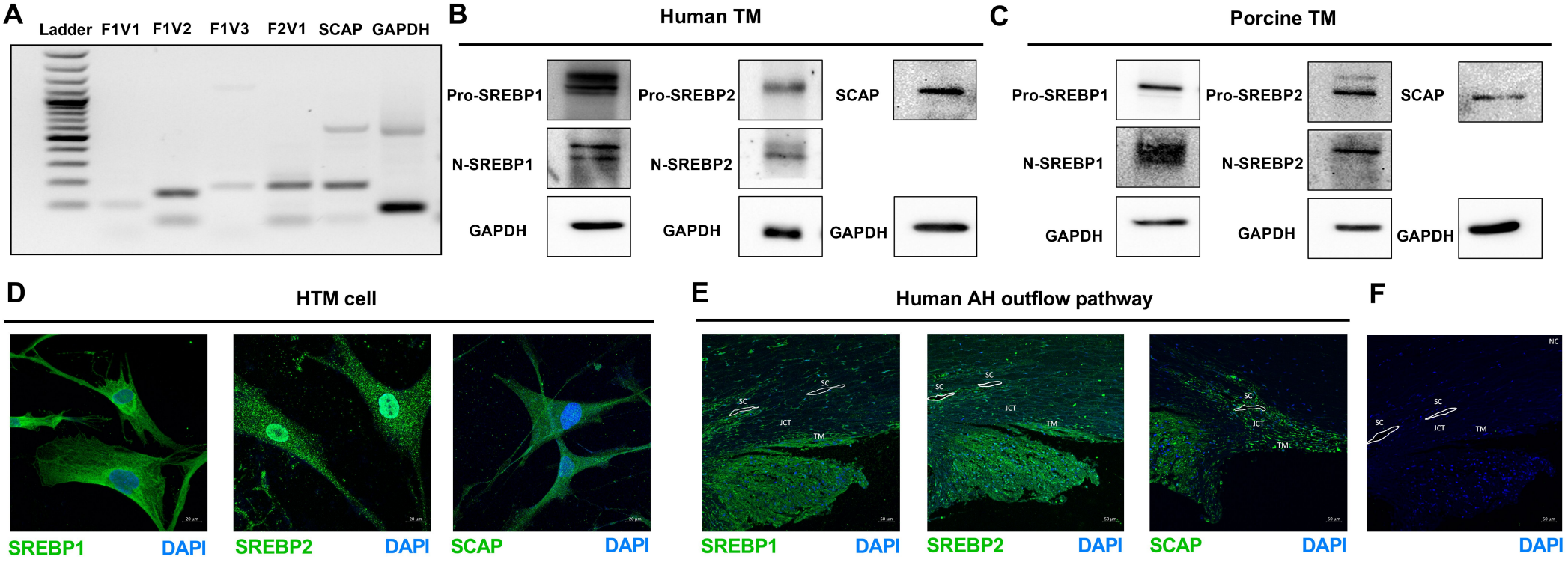
A
Ladder
F1V1
F1V2
F1V3
F2V1
SCAP
GAPDH
B
Human TM
Pro-SREBP1
Pro-SREBP2
SCAP
N-SREBP1
N-SREBP2
GAPDH
GAPDH
GAPDH
C
Porcine TM
Pro-SREBP1
Pro-SREBP2
SCAP
N-SREBP1
N-SREBP2
GAPDH
GAPDH
GAPDH
D
HTM cell
SREBP1
DAPI
SREBP2
DAPI
SCAP
DAPI
E
Human AH outflow pathway
SC
JCT
TM
SREBP1
DAPI
SREBP2
DAPI
SCAP
DAPI
F
NC
SC
JCT
TM
DAPI

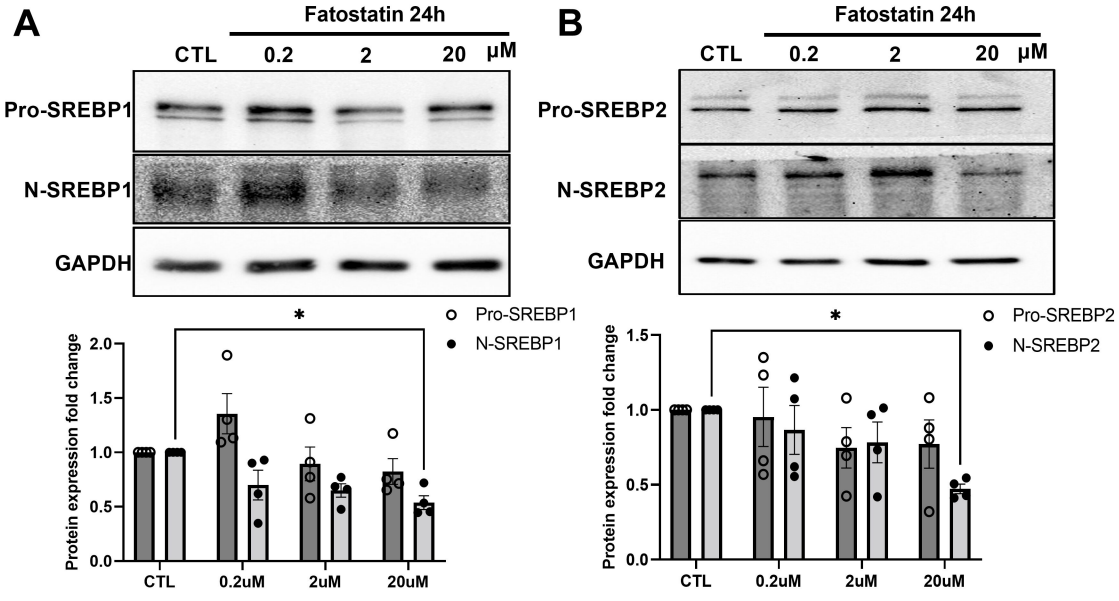
A
Fatostatin 24h
CTL
0.2
2
20
μM
Pro-SREBP1
N-SREBP1
GAPDH
Pro-SREBP1
N-SREBP1
Protein expression fold change
CTL
0.2uM
2uM
20uM
B
Fatostatin 24h
CTL
0.2
2
20
μM
Pro-SREBP2
N-SREBP2
GAPDH
Pro-SREBP2
N-SREBP2
Protein expression fold change
CTL
0.2uM
2uM
20uM

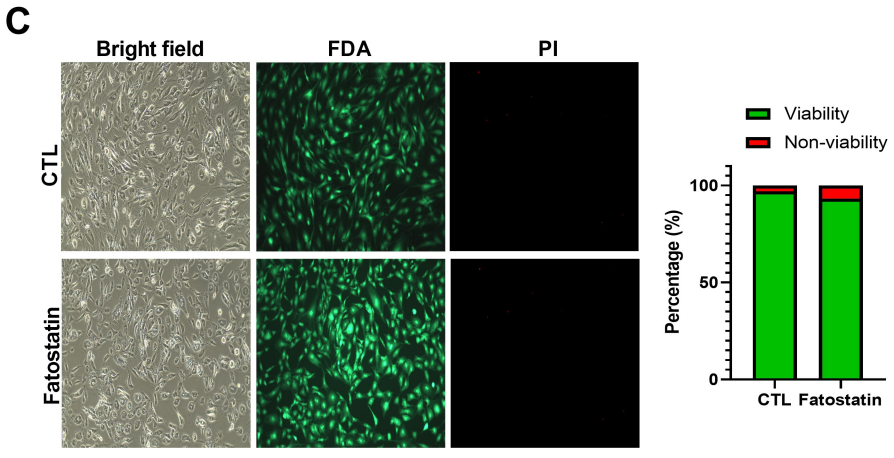
C
Bright field
FDA
PI
CTL
Fatostatin
Viability
Non-viability
Percentage (%)
CTL
Fatostatin

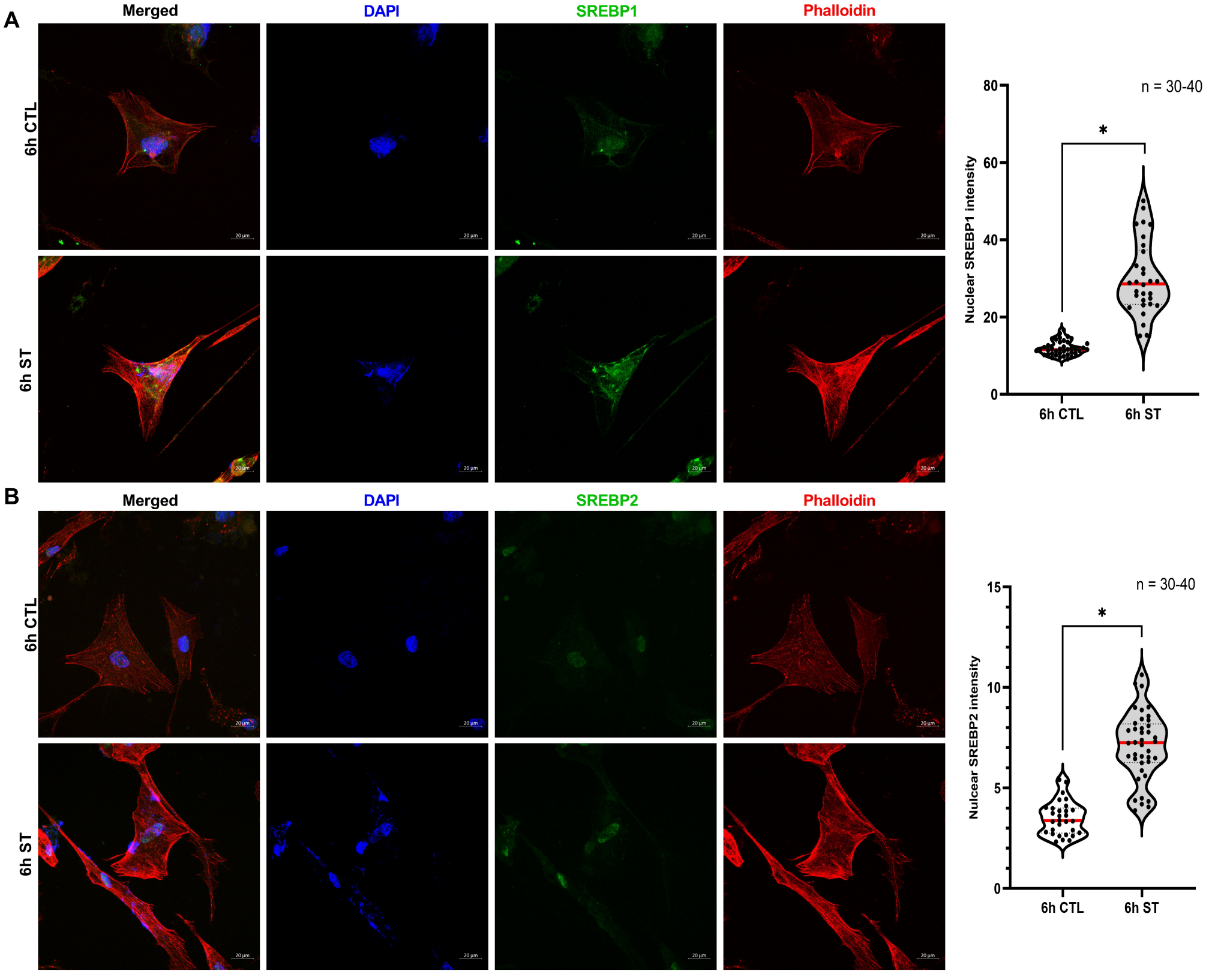
A
Merged
DAPI
SREBP1
Phalloidin
6h CTL
6h ST
20 µm
n = 30-40
*
Nuclear SREBP1 intensity
0
20
40
60
80
6h CTL
6h ST
B
Merged
DAPI
SREBP2
Phalloidin
6h CTL
6h ST
20 µm
n = 30-40
*
Nulcear SREBP2 intensity
0
5
10
15
6h CTL
6h ST

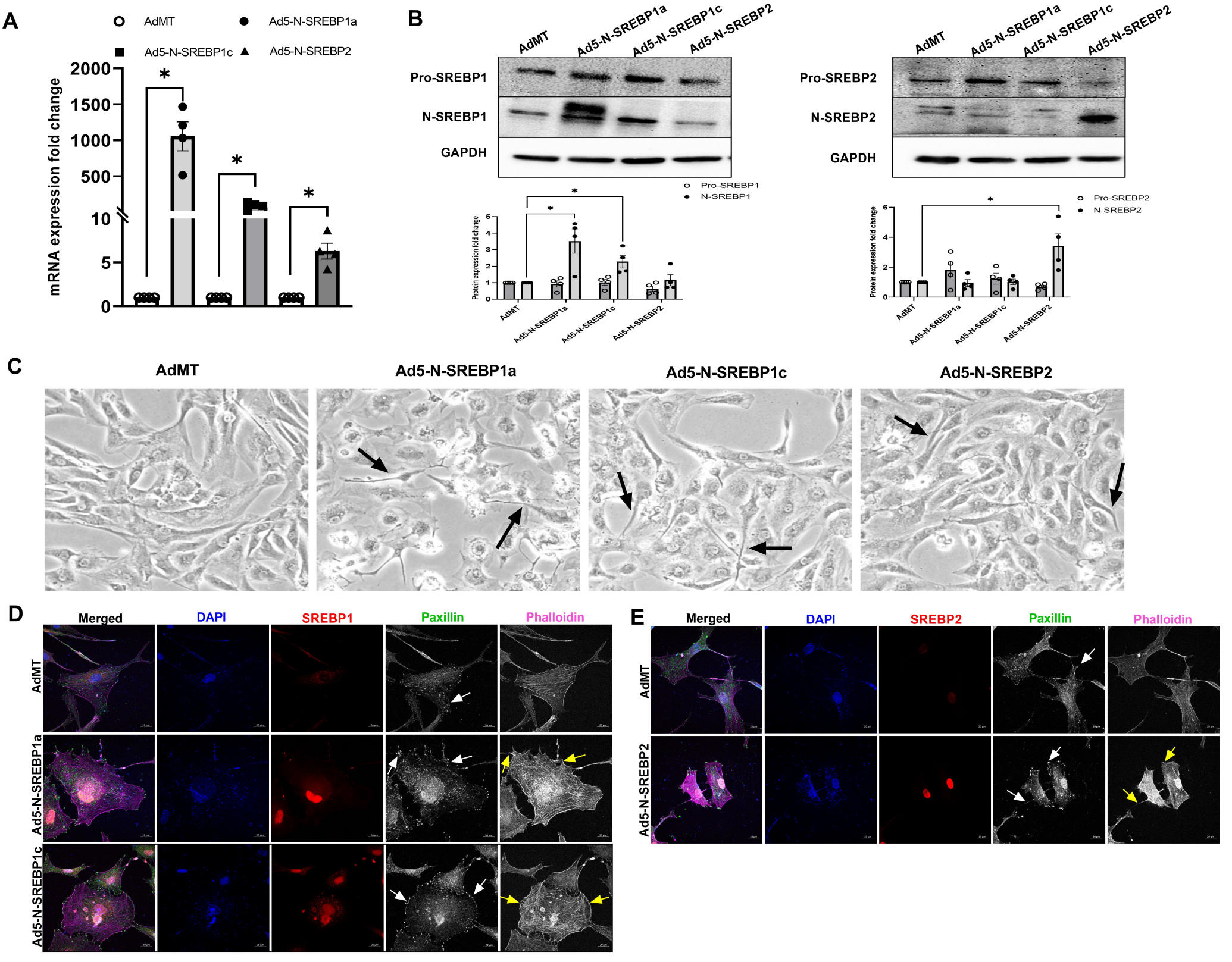
A
AdMT
Ad5-N-SREBP1a
Ad5-N-SREBP1c
Ad5-N-SREBP2
mRNA expression fold change
2000
1500
1000
500
10
5
0
B
AdMT
Ad5-N-SREBP1a
Ad5-N-SREBP1c
Ad5-N-SREBP2
Pro-SREBP1
N-SREBP1
GAPDH
Pro-SREBP2
N-SREBP2
Protein expression fold change
C
AdMT
Ad5-N-SREBP1a
Ad5-N-SREBP1c
Ad5-N-SREBP2
D
Merged
DAPI
SREBP1
Paxillin
Phalloidin
E
SREBP2

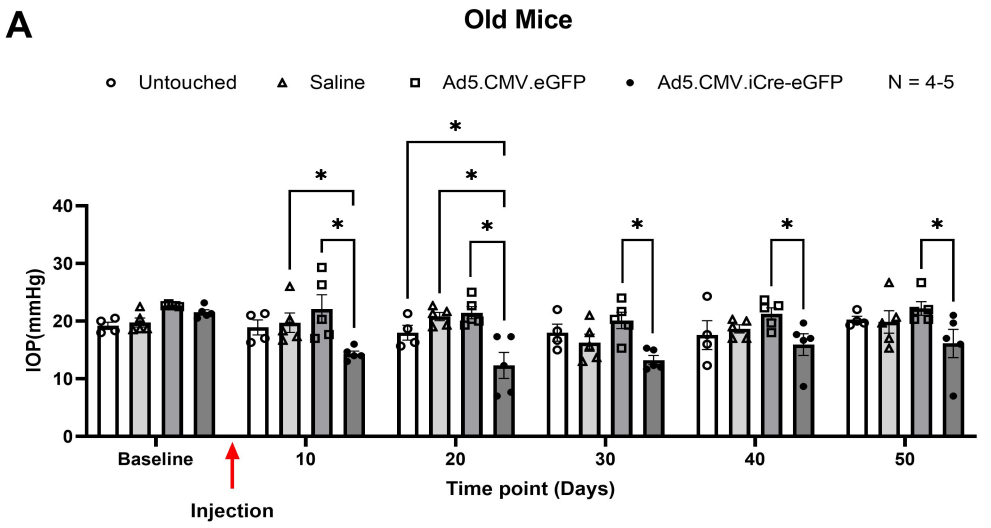
A
Old Mice
Untouched
Saline
Ad5.CMV.eGFP
Ad5.CMV.iCre-eGFP
N = 4-5
IOP(mmHg)
Baseline
Injection
Time point (Days)

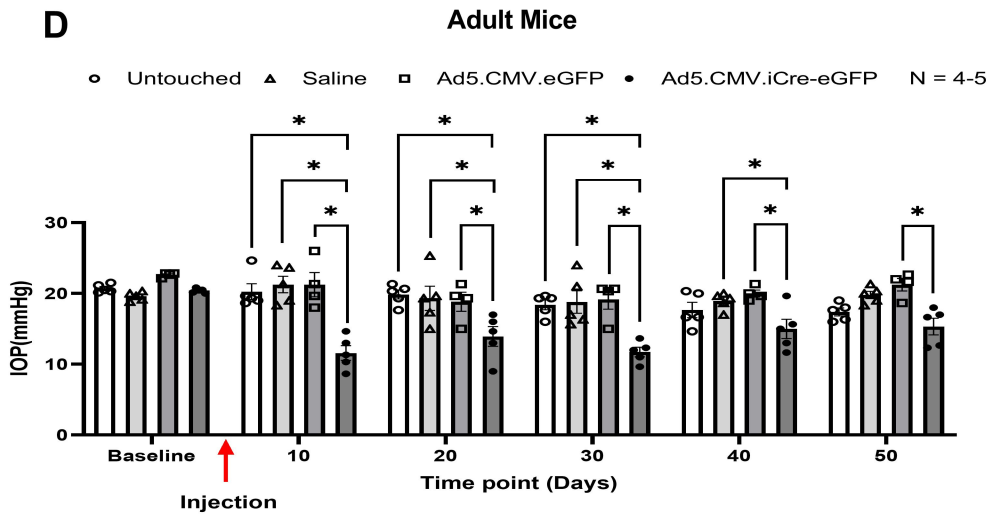
D
Adult Mice
Untouched
Saline
Ad5.CMV.eGFP
Ad5.CMV.iCre-eGFP
N = 4-5
IOP(mmHg)
Baseline
Injection
Time point (Days)

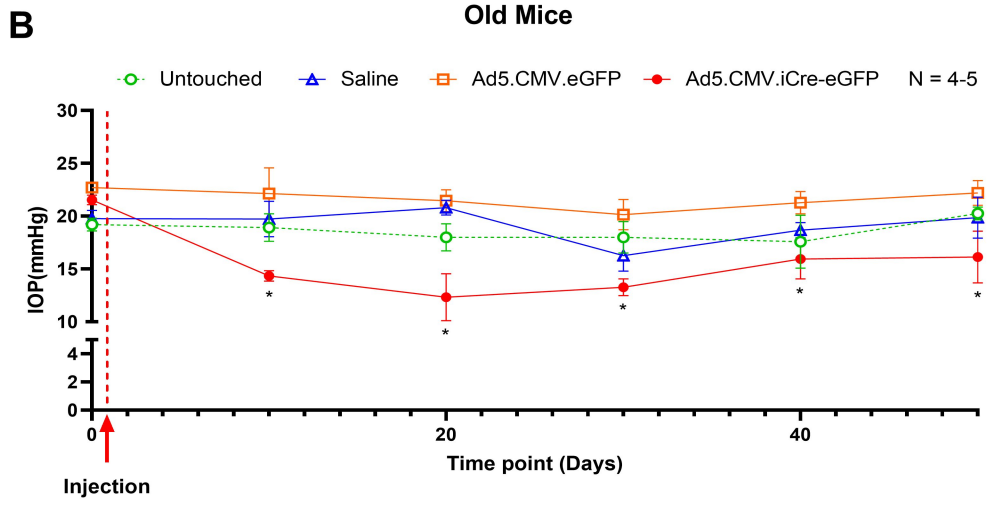
B
Old Mice
Untouched
Saline
Ad5.CMV.eGFP
Ad5.CMV.iCre-eGFP
N = 4-5
IOP(mmHg)
Injection
Time point (Days)

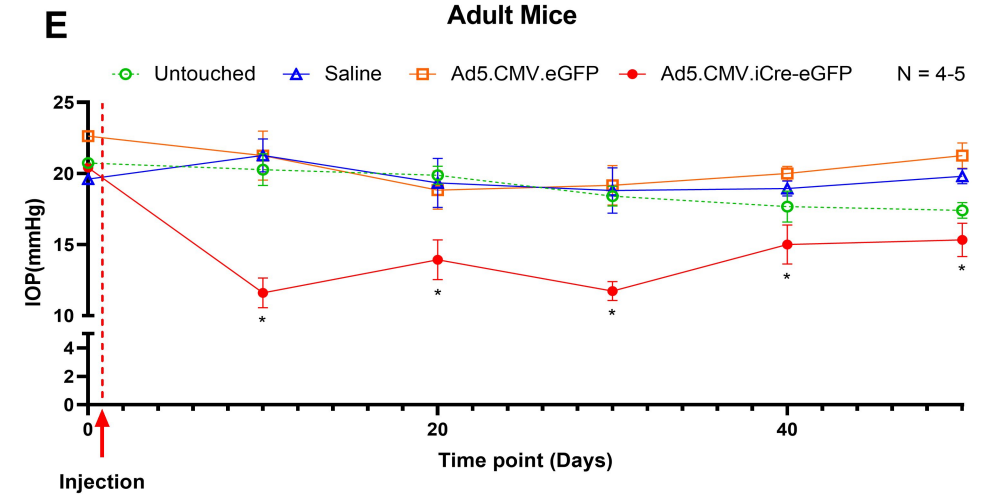
E
Adult Mice
Untouched
Saline
Ad5.CMV.eGFP
Ad5.CMV.iCre-eGFP
N = 4-5
IOP(mmHg)
Injection
Time point (Days)

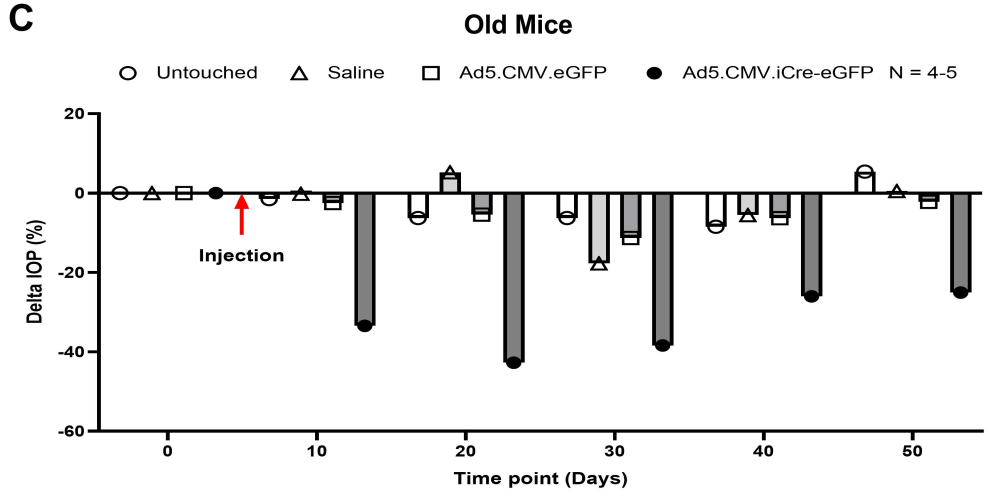
C
Old Mice
Untouched
Saline
Ad5.CMV.eGFP
Ad5.CMV.iCre-eGFP
N = 4-5
Delta IOP (%)
Injection
Time point (Days)

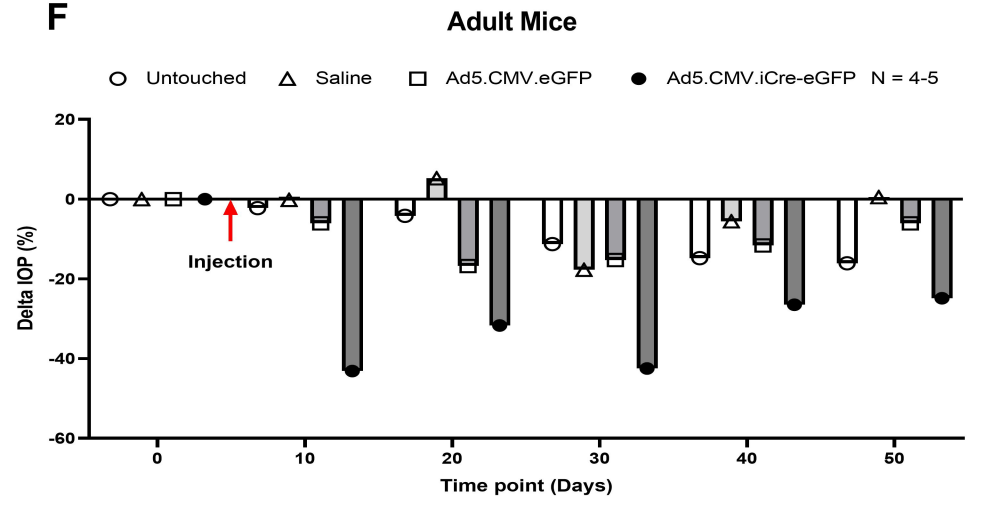
F
Adult Mice
Untouched
Saline
Ad5.CMV.eGFP
Ad5.CMV.iCre-eGFP
N = 4-5
Delta IOP (%)
Injection
Time point (Days)

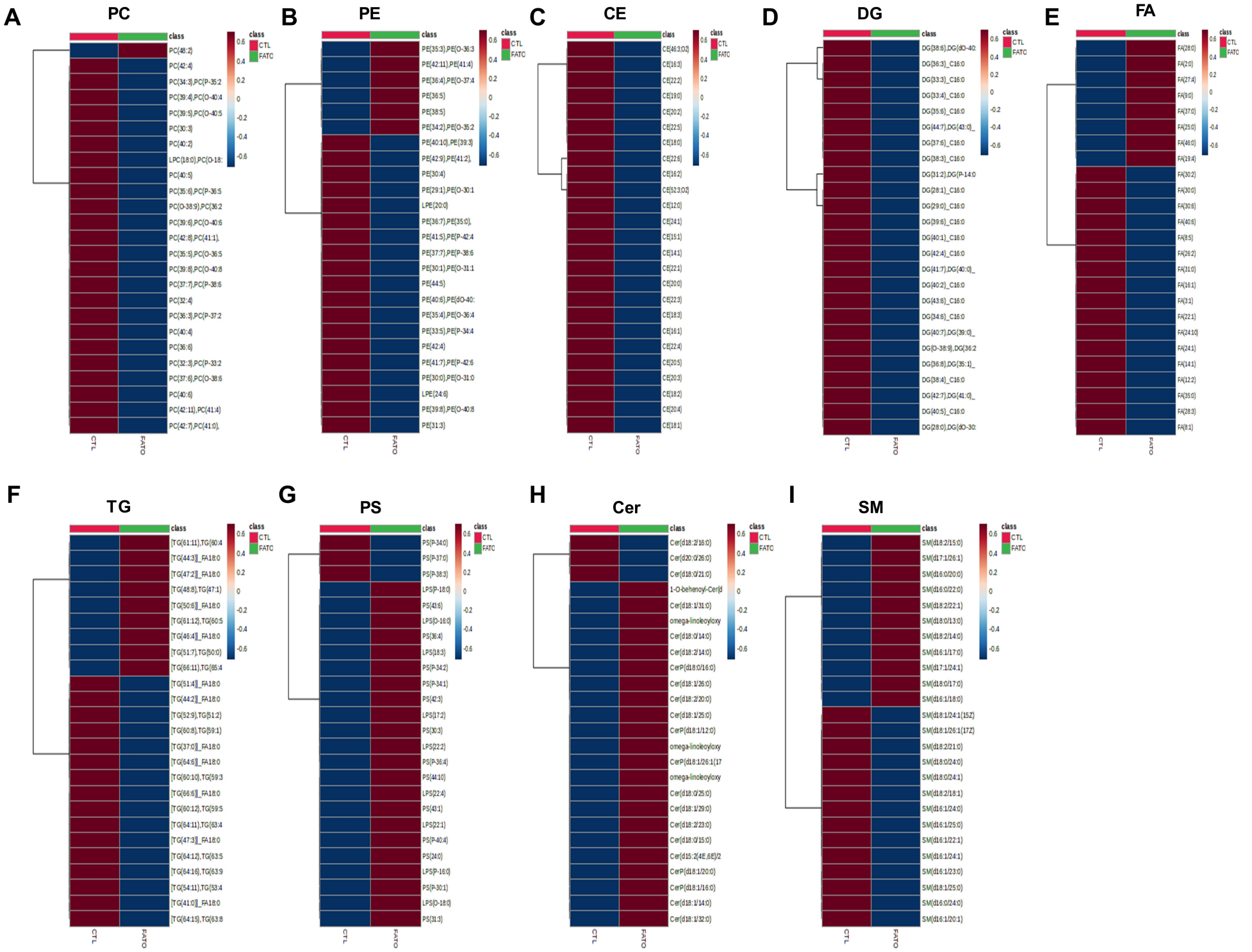
A
PC
class
PC(48:2)
PC(42:4)
PC(34:3),PC(P-35:2
PC(39:4),PC(O-40:4
PC(39:5),PC(O-40:5
PC(30:3)
PC(40:2)
LPC(18:0),PC(O-18:
PC(40:5)
PC(35:6),PC(P-36:5
PC(O-38:9),PC(36:2
PC(39:6),PC(O-40:6
PC(42:8),PC(41:1),
PC(35:5),PC(O-36:5
PC(39:8),PC(O-40:8
PC(37:7),PC(P-38:6
PC(32:4)
PC(36:3),PC(P-37:2
PC(40:4)
PC(36:6)
PC(32:3),PC(P-33:2
PC(37:6),PC(O-38:6
PC(40:6)
PC(42:11),PC(41:4)
PC(42:7),PC(41:0),
CTL
FATC
B
PE
class
PE(35:3),PE(O-36:3
PE(42:11),PE(41:4)
PE(36:4),PE(O-37:4
PE(36:5)
PE(38:5)
PE(34:2),PE(O-35:2
PE(40:10),PE(39:3)
PE(42:9),PE(41:2),
PE(30:4)
PE(29:1),PE(O-30:1
LPE(20:0)
PE(36:7),PE(35:0),
PE(41:5),PE(P-42:4
PE(37:7),PE(P-38:6
PE(30:1),PE(O-31:1
PE(44:5)
PE(40:6),PE(dO-40:
PE(35:4),PE(O-36:4
PE(33:5),PE(P-34:4
PE(42:4)
PE(41:7),PE(P-42:6
PE(30:0),PE(O-31:0
LPE(24:6)
PE(39:8),PE(O-40:8
PE(31:3)
CTL
FATC
C
CE
class
CE(46:3;O2)
CE(16:3)
CE(22:2)
CE(19:0)
CE(20:2)
CE(22:5)
CE(18:0)
CE(22:6)
CE(16:2)
CE(52:3;O2)
CE(12:0)
CE(24:1)
CE(15:1)
CE(14:1)
CE(22:1)
CE(20:0)
CE(22:3)
CE(18:3)
CE(16:1)
CE(22:4)
CE(20:5)
CE(20:3)
CE(18:2)
CE(20:4)
CE(18:1)
CTL
FATC
D
DG
class
DG(38:6),DG(dO-40:
DG(36:3)_C16:0
DG(33:3)_C16:0
DG(33:4)_C16:0
DG(35:6)_C16:0
DG(44:7),DG(43:0)_
DG(37:6)_C16:0
DG(38:3)_C16:0
DG(31:2),DG(P-14:0
DG(28:1)_C16:0
DG(29:0)_C16:0
DG(39:6)_C16:0
DG(40:1)_C16:0
DG(42:4)_C16:0
DG(41:7),DG(40:0)_
DG(40:2)_C16:0
DG(43:6)_C16:0
DG(34:6)_C16:0
DG(40:7),DG(39:0)_
DG(O-38:9),DG(36:2
DG(36:8),DG(35:1)_
DG(38:4)_C16:0
DG(42:7),DG(41:0)_
DG(40:5)_C16:0
DG(28:0),DG(dO-30:
CTL
FATC
E
FA
class
FA(28:0)
FA(2:0)
FA(27:4)
FA(9:0)
FA(37:0)
FA(25:0)
FA(46:0)
FA(19:4)
FA(30:2)
FA(30:0)
FA(30:6)
FA(40:6)
FA(8:5)
FA(26:2)
FA(31:0)
FA(16:1)
FA(3:1)
FA(22:1)
FA(24:1:0)
FA(24:1)
FA(14:1)
FA(12:2)
FA(35:0)
FA(28:3)
FA(8:1)
CTL
FATC
F
TG
class
[TG(61:11),TG(60:4
[TG(44:3)]_FA18:0
[TG(47:2)]_FA18:0
[TG(48:8),TG(47:1)
[TG(50:6)]_FA18:0
[TG(61:12),TG(60:5
[TG(46:4)]_FA18:0
[TG(51:7),TG(50:0)
[TG(66:11),TG(65:4
[TG(51:4)]_FA18:0
[TG(44:2)]_FA18:0
[TG(52:9),TG(51:2)
[TG(60:8),TG(59:1)
[TG(37:0)]_FA18:0
[TG(64:6)]_FA18:0
[TG(60:10),TG(59:3
[TG(66:6)]_FA18:0
[TG(60:12),TG(59:5
[TG(64:11),TG(63:4
[TG(47:3)]_FA18:0
[TG(64:12),TG(63:5
[TG(64:16),TG(63:9
[TG(54:11),TG(53:4
[TG(41:0)]_FA18:0
[TG(64:15),TG(63:8
CTL
FATC
G
PS
class
PS(P-34:0)
PS(P-37:0)
PS(P-38:3)
LPS(P-18:0)
PS(43:6)
LPS(O-16:0)
PS(36:4)
LPS(18:3)
PS(P-34:2)
PS(P-34:1)
PS(42:3)
LPS(17:2)
PS(30:3)
LPS(22:2)
PS(P-36:4)
PS(44:10)
LPS(22:4)
PS(43:1)
LPS(22:1)
PS(P-40:4)
PS(24:0)
LPS(P-16:0)
PS(P-30:1)
LPS(O-18:0)
PS(31:3)
CTL
FATC
H
Cer
class
Cer(d18:2/16:0)
Cer(d20:0/26:0)
Cer(d18:0/21:0)
1-O-behenoyl-Cer(d
Cer(d18:1/31:0)
omega-linoleoyloxy
Cer(d18:0/14:0)
Cer(d18:2/14:0)
CerP(d18:0/16:0)
Cer(d18:1/26:0)
Cer(d18:2/20:0)
Cer(d18:1/25:0)
CerP(d18:1/12:0)
omega-linoleoyloxy
CerP(d18:1/26:1(17
omega-linoleoyloxy
Cer(d18:0/25:0)
Cer(d18:1/29:0)
Cer(d18:2/23:0)
Cer(d18:0/15:0)
Cer(d15:2(4E,6E)/2
CerP(d18:1/20:0)
CerP(d18:1/16:0)
Cer(d18:1/14:0)
Cer(d18:1/32:0)
CTL
FATC
I
SM
class
SM(d18:2/15:0)
SM(d17:1/26:1)
SM(d16:0/20:0)
SM(d16:0/22:0)
SM(d18:2/22:1)
SM(d18:0/13:0)
SM(d18:2/14:0)
SM(d16:1/17:0)
SM(d17:1/24:1)
SM(d18:0/17:0)
SM(d16:1/18:0)
SM(d18:1/24:1(15Z)
SM(d18:1/26:1(17Z)
SM(d18:2/21:0)
SM(d18:0/24:0)
SM(d18:0/24:1)
SM(d18:2/18:1)
SM(d16:1/24:0)
SM(d16:1/25:0)
SM(d16:1/22:1)
SM(d16:1/24:1)
SM(d16:1/23:0)
SM(d18:1/25:0)
SM(d16:0/24:0)
SM(d16:1/20:1)
CTL
FATC

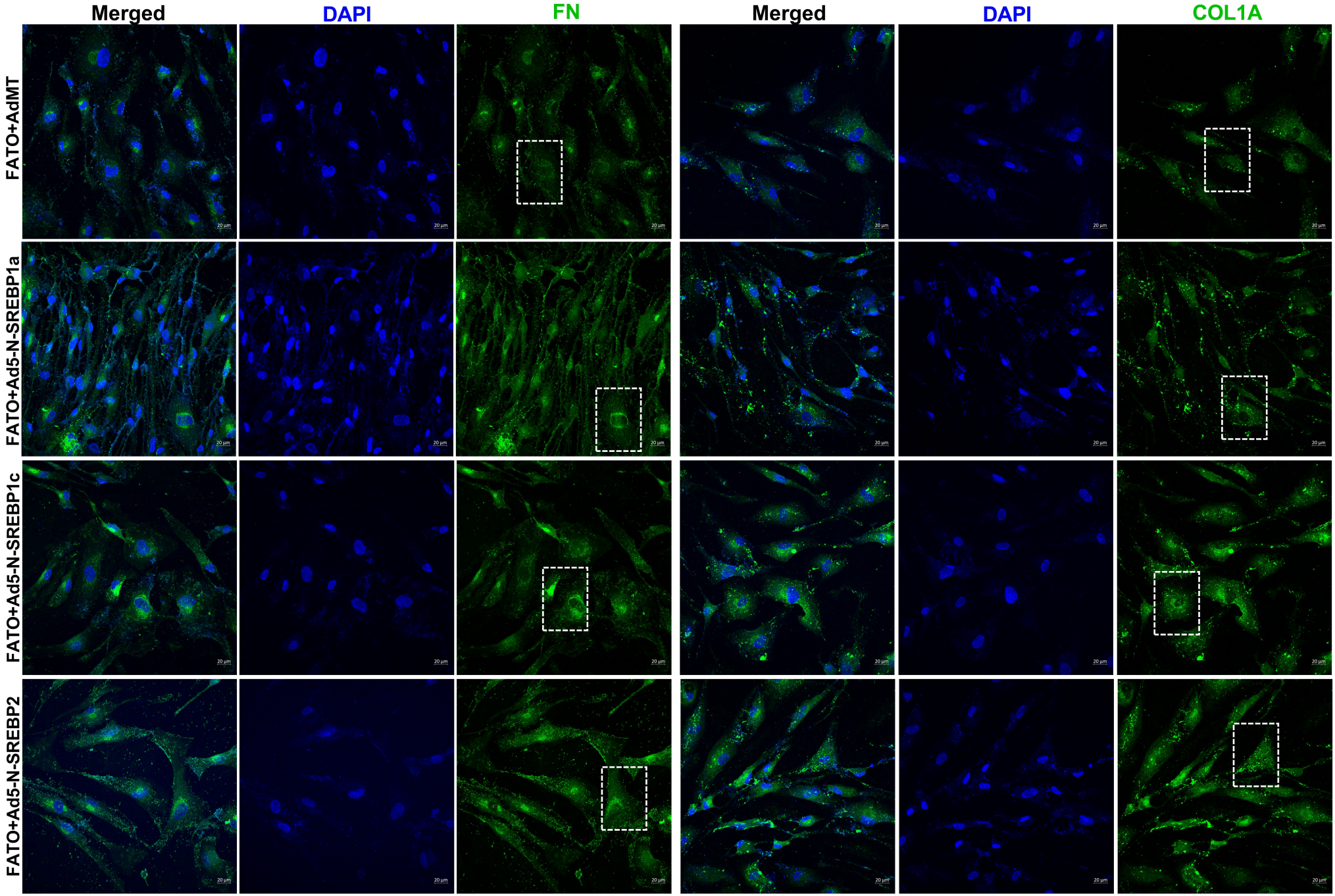
Merged
DAPI
FN
Merged
DAPI
COL1A
FATO+AdMT
FATO+Ad5-N-SREBP1a
FATO+Ad5-N-SREBP1c
FATO+Ad5-N-SREBP2
20 μm